Charged Particle Production in pp and Pb–Pb Collisions measured with ALICE at the LHC

Dissertation
zur Erlangung des Doktorgrades
der Naturwissenschaften

vorgelegt beim Fachbereich 13
der Johann Wolfgang Goethe-Universität
in Frankfurt am Main

von

Philipp Lüttig
aus Frankfurt am Main

Frankfurt am Main, 2017

(D30)

vom Fachbereich 13 der
Johann Wolfgang Goethe-Universität als Dissertation angenommen.

Dekan:	Prof. Dr. Owe Philipsen
Gutachter:	Prof. Dr. Henner Büsching
	Prof. Dr. Harald Appelshäuser
Datum der Disputation:	24.08.2017

Zusammenfassung

Die vorliegende Arbeit beschäftigt sich mit einer Untersuchung grundlegender Eigenschaften der Materie, insbesondere den Eigenschaften des sogenannten Quark-Gluon-Plasmas (QGP), das in Blei-Blei-Kollisionen bei einer Schwerpunktsenergie von $\sqrt{s_{NN}} =$ 2,76 TeV erzeugt und mit dem ALICE-Experiment am Large Hadron Collider (LHC) untersucht wird. Die Analyse konzentriert sich dabei auf die Produktion geladener primärer Teilchen als Funktion des Transversalimpulses (p_{T}). Dabei wird die Teilchenproduktion in Blei-Blei-Kollisionen mit der in Proton-Proton-Kollisionen verglichen. Weiterhin wird die Teilchenproduktion in Blei-Blei-Kollisionen relativ zur geometrischen Kollisionsebene, der sogenannten Ereignisebene, untersucht.
Die Protonen und Bleikerne werden im Zentrum des ALICE-Experiments zur Kollision gebracht. In ALICE werden unterschiedliche Detektortypen, die vielfältige Detektionstechniken einsetzen, für die Messungen kombiniert. Die geladenen Teilchen, die in den Kollisionen produziert und in dieser Arbeit untersucht werden, werden mit der Time Projection Chamber (TPC) und dem Inner Tracking System (ITS) gemessen. Beide befinden sich im sogenannten *central barrel* des Experiments, also im inneren Bereich von ALICE. Mit der Kombination beider Detektoren lassen sich im Rahmen dieser Arbeit in Blei-Blei-Kollisionen die geladenen Teilchen bis zu $p_{\mathrm{T}} = 100$ GeV/c nachweisen.
Die Analyse der Blei-Blei-Kollision basiert dabei auf Daten, die in den Datennahmeperioden LHC10h und LHC11h gemessen wurden. Im ersten Schritt der Auswertung werden die gemessenen Detektorsignale zu Teilchenspuren (sogenannten *tracks*) zusammengefasst. Diese *tracks* werden vorgefiltert und in sogenannten *AODs* gespeichert, um sowohl die Dateigröße zu reduzieren als auch die Analysegeschwindigkeiten zu verbessern. Charakteristische Ereignis-Kenngrößen, wie zum Beispiel die Zentralität oder die Ereignisebene der Kollision, werden zentral in ALICE berechnet, um die Vergleichbarkeit der Analysen in ALICE zu gewährleisten. Die Teilchenspuren für die hier vorliegende Analyse werden durch verschiedene Auswahlkriterien charakteristischer Spurgrößen selektiert. Eine Auswahl der Spuren, basierend auf der aktiven Länge einer Spur in der TPC, wird in dieser Arbeit erstmals angewendet. Es zeigt sich, dass diese rein geometrisch motivierte Größe

in den gemessenen Daten von den hier verwendeten Monte-Carlo-Simulationen recht gut reproduziert wird. Durch diese Übereinstimmung können die in dieser Arbeit verwendeten Korrekturen mit Hilfe der Monte-Carlo-Simulationen bestimmt werden: zuerst wird auf die begrenzte Nachweiseffizienz und geometrische Akzeptanz des Detektors für geladene Teilchen korrigiert. Diese Korrektur beinhaltet sowohl Ineffizienzen im Detektorsystem als auch eine limitierte geometrische Akzeptanz an den Detektorrändern. Die zweite Korrektur entfernt Sekundärteilchen, die auch nach Anwendung der Auswahlkriterien noch im Datensatz enthalten sind. Die dritte Korrektur betrifft den Transversalimpuls jedes Teilchens, um der p_{T}-Auflösung des Detektors Rechnung zu tragen. In dieser Arbeit wird dabei ein datenbasierter Ansatz gewählt, um diese Korrektur, die besonders bei hohen p_{T} zum Tragen kommt, zu bestimmen.
Die Teilchenproduktion in Proton-Proton-Kollisionen bei hohen Strahlenergien kann in zwei verschiedene Klassen eingeteilt werden, wobei man diese entsprechend des Transversalimpulses der produzierten Teilchen unterscheidet. Bei niedrigen p_{T} dominieren sogenannte weiche Prozesse den totalen Wirkungsquerschnitt der Teilchenproduktion, wohingegen sogenannte harte Prozesse bei hohen p_{T} vorherrschen. Da der Impulsübertrag zwischen den Stoßpartnern der Kollision bei niedrigen Transversalimpulsen klein ist, können nur phänomenologische Modelle die Teilchenproduktion bei kleinen p_{T} beschreiben. Bei hohen Transversalimpulsen wird die Teilchenproduktion typischerweise von Modellen beschrieben, die auf der perturbativen Quantenchromodynamik (pQCD) aufbauen. In diesen Modellen wird der totale Wirkungsquerschnitt der Teilchenproduktion in drei voneinander unabhängige Teile aufgeteilt: die Partonverteilungsfunktion (*parton distribution function*, PDF), den Wirkungsquerschnitt einer elementaren Reaktion sowie die Fragmentationsfunktion. Diese Aufteilung bezeichnet man auch als Faktorisierung.
In dieser Arbeit werden die Transversalimpulsspektren geladener Teilchen in Proton-Proton-Kollisionen bei drei verschiedenen Schwerpunktsenergien ($\sqrt{s}$ = 0,9, 2,76 und 7 TeV) untersucht. Die Spektren zeigen eine klare Abhängigkeit von der Schwerpunktsenergie der Kollision: man beobachtet ein Abflachen der Spektren mit ansteigender Kollisionsenergie. Des Weiteren werden die Spektren mit der Vorhersage einer NLO-pQCD-Rechnung [1, 2] verglichen. Das Modell liegt um etwa einen Faktor zwei über den gemessenen Spektren. Die Abhängigkeit der Transversalimpulsspektren von der Schwerpunktsenergie der Kollision wird zusätzlich noch im sogenannten x_{T}-*scaling* verglichen, in dem man annimmt, dass die Teilchenproduktion vom Verhältnis von p_{T} und der Kollisionsenergie abhängt. Hierbei zeigt sich eine gute Übereinstimmung der Spektren für alle drei verglichenen Schwerpunktsenergien für $x_{\mathrm{T}} \geq 0{,}006$.
Die Teilchenproduktion in Blei-Blei-Kollisionen lässt sich nicht allein durch eine einfache

Überlagerung der Teilchenproduktion in Proton-Proton-Kollisionen, skaliert mit der Zahl der binären Kollisionen, beschreiben. Durch ein QGP, das in Blei-Blei-Kollisionen erzeugt wird, verändern kollektive Effekte sowie Energieverlust-Mechanismen die Zahl der gemessenen Teilchen. Außerdem wird die PDF in Blei-Blei-Kollisionen im Vergleich zu Proton-Proton-Kollisionen modifiziert. Um die Eigenschaften des QGP zu untersuchen, wurden in der Literatur verschiedene Signaturen vorgeschlagen. Von besonderem Interesse in dieser Arbeit ist die Unterdrückung der Teilchenproduktion durch einen Energieverlust der in der Kollision entstandenen Partonen im Medium. Typischerweise wird diese Unterdrückung mit Hilfe des nuklearen Modifikationsfaktors R_{AA} untersucht, in dem das Verhältnis zwischen der Anzahl der Teilchen in Blei-Blei-Kollisionen und der Anzahl der Teilchen in Proton-Proton-Kollisionen, skaliert mit der Zahl der binären Kollisionen, gebildet wird; $R_{\mathrm{AA}} = 1$ bedeutet dann keine Unterdrückung der Teilchenproduktion in Blei-Blei-Kollisionen im Vergleich zur skalierten Proton-Proton-Referenz. Die Untersuchung der p_{T}-Abhängigkeit von R_{AA} kann dann weitere Informationen über die p_{T}-Abhängigkeit des zugrunde liegenden Energieverlusts geben.
In dieser Arbeit wird eine Studie der Teilchenproduktion geladener Teilchen in Blei-Blei-Kollisionen bei $\sqrt{s_{NN}} = 2{,}76$ TeV basierend auf einer Re-Analyse der Daten aus der Datennahmeperiode LHC10h präsentiert. Die Transversalimpulsspektren geladener Teilchen zeigen eine klare Zentralitätsabhängigkeit, insbesondere sichtbar im Vergleich zu einem skalierten Proton-Proton-Referenzspektrum bei der gleichen Kollisionsenergie. In zentralen Blei-Blei-Kollisionen ist die Teilchenproduktion im Vergleich zum Referenzspektrum unterdrückt, wohingegen die p_{T}-Spektren in Proton-Proton- und periphären Blei-Blei-Kollisionen besser übereinstimmen. Die Re-Analyse bestätigt bereits veröffentlichte Ergebnisse [3] des gleichen Datensatzes. Im Gegensatz zu [3] basiert die Re-Analyse allerdings auf einem neuen, im Rahmen dieser Arbeit entwickelten Analysecode, der zum ersten Mal AODs in der Analyse von p_{T}-Spektren geladener Teilchen verwendet. Die Bestätigung der Ergebnisse in [3] erlaubt es, den in dieser Arbeit neu entwickelten Analysecode für die Analyse des Datensatzes aus der Datennahmeperiode LHC11h zu verwenden, worauf alle im Folgenden näher diskutierten Analysen aufbauen. Durch den Einsatz von Zentralitätstriggern für zentrale und semi-zentrale Kollisionen kann in diesem Datensatz der maximal gemessene Transversalimpuls der Spektren geladener Teilchen in zentralen und semi-zentralen Kollisionen im Vergleich zu [3] um einen Faktor zwei von $p_{\mathrm{T}} = 50$ GeV/c auf $p_{\mathrm{T}} = 100$ GeV/c erweitert werden. Für $p_{\mathrm{T}} < 50$ GeV/c reduziert sich der statistische Fehler der Spektren im Vergleich zu [3] um einen Faktor zwei. Durch die Analyse in dieser Arbeit werden somit auch die Spektren bei hohen p_{T} zugänglich; zusammen mit den kleineren statistischen Fehlern bei niedrigeren p_{T} kann dies nun helfen,

den durch das QGP induzierten Energieverlust der unterliegenden, in den Kollisionen entstehenden Partonen in Modellrechnungen genauer zu bestimmen.
Um die Messungen bei hohen p_{T} zu ergänzen, wird in dieser Arbeit auch die Teilchenproduktion bei niedrigen p_{T} untersucht; dazu werden die Spektren geladener Teilchen durch den mittleren Transversalimpuls $\langle p_{\mathrm{T}} \rangle$ charakterisiert. Zunächst wird die Multiplizitätsabhängigkeit von $\langle p_{\mathrm{T}} \rangle$ in Proton-Proton-Kollisionen als Referenzmessung für drei verschiedene Kollisionsenergien, $\sqrt{s} = 0{,}9$, 2,76 und 7 TeV, untersucht. Man beobachtet nur eine kleine Abhängigkeit der $\langle p_{\mathrm{T}} \rangle$-Werte von der Kollisionsenergie. Ausgehend von dieser Referenzmessung, wird nun die Abhängigkeit von $\langle p_{\mathrm{T}} \rangle$ vom Kollisionssystem für Proton-Proton-, Proton-Blei- und Blei-Blei-Kollisionen verglichen. Man beobachtet dabei einen deutlichen Unterschied zwischen den Kollisionssystemen: in Proton-Proton-Kollisionen steigt $\langle p_{\mathrm{T}} \rangle$ stark mit der Multiplizität an. In Blei-Blei-Kollisionen steigt $\langle p_{\mathrm{T}} \rangle$ für kleine Multiplizitäten mit der Multiplizität an und ist bei hohen Multiplizitäten unabhängig von der Multiplizität. Proton-Blei-Kollisionen zeigen Eigenschaften sowohl der Proton-Proton- als auch der Blei-Blei-Kollisionen: ein starker Anstieg von $\langle p_{\mathrm{T}} \rangle$ mit der Multiplizität bei niedrigen Multiplizitäten und ein Plateau bei höheren Multiplizitäten. Das Plateau setzt in Proton-Blei-Kollisionen bei höheren $\langle p_{\mathrm{T}} \rangle$ als in Blei-Blei-Kollisionen ein.
Im letzten Teil dieser Arbeit wird der nukleare Modifikationsfaktor R_{AA} geladener Teilchen in Blei-Blei-Kollisionen bei $\sqrt{s_{NN}} = 2{,}76$ TeV basierend auf dem Datensatz der Datennahmeperiode LHC11h mit dem neu entwickelten Analysecode eingehender untersucht. Dazu werden zwei verschiedene Methoden entwickelt und diskutiert, um das dafür notwendige Proton-Proton-Referenzspektrum zu konstruieren. Für die Veröffentlichung [4] stand noch keine Messung eines Proton-Proton-Referenzspektrums bei $\sqrt{s_{NN}} = 2{,}76$ TeV zur Verfügung. Daher wurde im Rahmen dieser Arbeit ein Referenzspektrum, basierend auf gemessenen Proton-Proton-Spektren bei niedrigeren oder höheren Energien, skaliert mit NLO-pQCD-Rechnungen bzw. mit Hilfe einer Interpolationsmethode zwischen den Messungen bei zwei anderen Kollisionsenergien konstruiert. Für die Veröffentlichung [3] sowie R_{AA}, basierend auf den Daten der Datennahmeperiode LHC11h, wird in beiden Fällen im Rahmen dieser Arbeit das Referenzspektrum aus einem gemessenen Proton-Proton-p_{T}-Spektrum bei $\sqrt{s} = 2{,}76$ TeV konstruiert. Um die p_{T}-Reichweite des Referenzspektrums zu erhöhen, wird das gemessene Proton-Proton-Spektrum mit einer sogenannten modifizierten Hagedorn-Funktion parametrisiert. Diese Parametrisierung wird dann zu $p_{\mathrm{T}} = 100$ GeV/c extrapoliert; dies entspricht der p_{T}-Reichweite in zentralen Blei-Blei-Kollisionen des Datensatzes der Datennahmeperiode LHC11h. Für alle Zentralitäten beobachtet man $R_{\mathrm{AA}} < 1$. Für die 0 - 5 % zentralsten Kollisionen zeigt R_{AA} ein

Minimum von $R_{\mathrm{AA}} \approx 0.2$ bei $p_{\mathrm{T}} = 6 - 7$ GeV/c und steigt mit p_{T} zu höheren p_{T} an. Für $p_{\mathrm{T}} > 40$ GeV/c deutet R_{AA} in zentralen Kollisionen ein Plateau an, welches den in dieser Arbeit neu zugänglichen p_{T}-Bereich abdeckt. Ein sogenannter *punch-through* der Teilchen kann innerhalb der systematischen Unsicherheiten allerdings nicht ausgeschlossen werden. In den 70 - 80 % periphärsten Kollisionen zeigt R_{AA} nur eine schwache p_{T}-Abhängigkeit mit $R_{\mathrm{AA}} \approx 0.8$.

Zusätzlich zur Untersuchung der Unterdrückung der Teilchenproduktion durch den Energieverlust der Partonen im QGP kann die Untersuchung des relativen Energieverlusts der Partonen im Medium helfen, die Energieverlustmechanismen noch weiter zu präzisieren. In dieser Arbeit wird, analog zu [5], der relative Transversalimpulsverlust S_{loss} als Näherung für den relativen Energieverlust der Partonen verwendet. In zentralen Kollisionen nimmt S_{loss} mit p_{T} ab, was sich mit der Beobachtung deckt, dass R_{AA} mit p_{T} ansteigt. In periphären Kollisionen beobachtet man fast keine p_{T}-Abhängigkeit von S_{loss}. Außerdem wird die Zentralitätsabhängigkeit von S_{loss} für feste p_{T}-Bereiche untersucht. S_{loss} nimmt für alle diese p_{T}-Bereiche für zunehmend zentralere Kollisionen zu. Weiterhin nimmt S_{loss} innerhalb jeder Zentralitätsklasse zu höher werdenden p_{T} ab. Man beobachtet, wie in [6] vorgeschlagen, dass sich S_{loss} als Funktion der Zentralität für feste p_{T}-Bereiche proportional zu $N_{part}^{2/3}$ verhält.

Alternativ zur Analyse von S_{loss} wird zur genaueren Bestimmung des Energieverlusts und besonders dessen Pfadlängenabhängigkeit im Medium die Abhängigkeit von R_{AA} vom azimutalen Winkel $\Delta\phi$ der produzierten Teilchen relativ zur Ereignisebene untersucht. Dabei beobachtet man eine klare Abhängigkeit von R_{AA} von $\Delta\phi$: für Teilchen, die senkrecht zur Ereignisebene (*out-of-plane*) produziert werden, ist R_{AA} kleiner als für Teilchen, die in der Ereignisebene (*in-plane*) produziert werden. Dies lässt sich auf unterschiedliche Pfadlängen der Teilchen im Medium zurückführen: auf Grund der genähert mandelförmigen Form des Überlappbereichs der beiden kollidierenden Ionen, die besonders deutlich in semi-zentralen Kollisionen auftritt, ist die Pfadlänge der Teilchen *in-plane* kürzer als die Pfadlänge *out-of-plane*. Das Ergebnis der Messung wird mit einer Modellrechnung [7] verglichen, die R_{AA} basierend auf dem Energieverlust von Quarks und Gluonen im Medium berechnet. Um das Model mit den gemessenen Daten vergleichen zu können, wird die analytische Form des Modells an das inklusive, d. h. Ereignisebenen-unabhängige R_{AA} als Funktion von p_{T} angepasst. Die daraus bestimmten freien Parameter α_s und $\hat{q}$ des Modells sowie die Pfadlänge selbst, die in einer Glauber-Monte-Carlo-Simulation bestimmt wird, werden dann verwendet, um ein $\Delta\phi$-abhängiges R_{AA}, basierend auf dem Modell, vorherzusagen. Für mittlere Werte von $\Delta\phi$ stimmt die Vorhersage mit dem gemessenen R_{AA} überein. Die $\Delta\phi$-Abhängigkeit in

der Vorhersage ist allerdings weniger stark ausgeprägt als in den Daten. Für sehr hohe und sehr niedrige $\Delta\phi$ kann die Abweichung zwischen Daten und Modell möglicherweise durch Effekte des elliptischen Flusses erklärt werden, die in den Daten vorhanden, aber im Modell nicht beinhaltet sind. Weiterhin kann die $\Delta\phi$-Abhängigkeit von R_{AA} in eine Pfadlängenabhängigkeit übersetzt werden. Insgesamt zeigt diese Pfadlängenabhängigkeit keine starke Abhängigkeit von R_{AA} als Funktion der Zentralität. Dies lässt sich erklären, da die Unterdrückung in erster Näherung von der Pfadlänge im Medium abhängen sollte.

Zusammengefasst lässt sich feststellen: die Messung von R_{AA} in Blei-Blei-Kollisionen bei $\sqrt{s_{NN}} = 2{,}76$ TeV bei hohem p_{T} kann zusammen mit einer detaillierten Untersuchung von R_{AA} als Funktion des Winkels der Teilchen relativ zur Ereignisebene und der daraus bestimmten Pfadlängenabhängigkeit der Teilchen im Medium helfen, das theoretische Verständnis der Teilchenproduktion und der Unterdrückungsmechanismen in einem heißen und dichten Medium weiter zu verbessern. Weiterhin deuten aktuelle Modelle darauf hin, dass der Energieverlust allein die beobachtete Pfadlängenabhängigkeit von R_{AA} nicht beschreiben kann. Zusätzliche kollektive Effekte, wie z. B. der elliptische Fluss, müssen in die Modelle mit aufgenommen werden.

Die Messung der p_{T}-Spektren geladener Teilchen in Blei-Blei-Kollisionen wird zur Zeit zu noch höheren Kollisionsenergien am LHC erweitert. Zusammen mit den Ergebnissen dieser Arbeit im Vergleich mit Modellvorhersagen kann so ein immer genaueres Verständnis des Energieverlusts der in den Kollisionen entstehenden Partonen in heißer, dichter Materie entwickelt und so die Eigenschaften des QGP mit größerer Präzision charakterisiert werden.

Contents

Chapter 1.

Abstract

In high energy heavy-ion collisions at the LHC a new state of matter, the so-called *Quark-Gluon Plasma* (QGP), is created. This state of matter is believed to have existed during the very early stages of the universe, where quarks and gluons were formed and where they created the now existing matter.
The ALICE Experiment at the CERN-LHC is studying the properties of the QGP and is trying to better understand the nature of this still novel state of matter. The challenge is, that the QGP itself is very short-lived and can only be measured indirectly via particles in the final state of the heavy-ion collision. In this work, the focus lies on charged particles with high transverse momenta which result from the fragmentation of partons which are created in hard interactions in the early times of a heavy-ion collision before the creation of the QGP. The partons travel through the medium and loose energy via elastic collisions or the radiation of gluons. Finally they fragment into hadrons, which are then measured in the detectors of the experiment. In the experiment, the particle production in Pb–Pb collisions is compared to the particle production in pp collisions to gain knowledge about the suppression patterns and the energy loss mechanisms at play.
This thesis is structured as follows. In chapter 2, an introduction to the physics motivation of the QGP is given. This includes a description of soft and hard processes, which rule particle interactions in the collisions. In addition, different energy loss mechanisms and their effect on the measurement are discussed. Of specific interest in this work is the azimuthal angular dependence of the particle production, which is motivated in chapter 2 as well. Chapter 3 describes the experimental setup including a description of the relevant detectors for this work, the Inner Tracking System and the Time Projection Chamber. The following chapter 4 provides a detailed description of the data analysis, starting from the reconstruction of the particle traces in the detector, the so-called tracks, and the determination of the centrality and the event-plane of the collision. The

extraction of the tracking efficiency and acceptance correction of charged particles, a secondary contamination correction and p_{T} resolution correction, which are specific for this work, are discussed as well. In chapter 5, as result of the analysis, charged particle transverse momentum spectra in pp and Pb–Pb collisions are presented. Furthermore, the spectra are characterized by their average transverse momentum. Finally, in chapter 6 the measurement of the charged particle transverse momentum spectra in Pb–Pb collisions are compared to those measured in pp collisions at the same center-of-mass energy in terms of the nuclear modification factor. As a complementary measurement, this comparison between the charged particle production in Pb–Pb and pp collisions is discussed in terms of the relative momentum loss S_{loss}. This chapter closes with results on the dependence of the charged particle production relative to the event-plane angle, which is the main focus of this work.

Chapter 2.

Introduction

2.1. The Standard Model of Particle Physics

The Standard Model of Particle Physics describes the elementary particles, i.e. the building blocks of matter, as well as the interactions between them. The elementary particles can be divided into *fermions* and *bosons*, the fermions build matter and the bosons are the exchange particles of the interactions. The fermions can be ordered by their mass into three different so called *families* (see table 2.1) and into two basic groups of particles, the *quarks* and the *leptons*. Both have half-numbered spin. The first family of quarks includes the two lightest quarks, the *up* and the *down* quark, which have roughly the same mass. The second family includes the *strange* quark, which is already much heavier than the up or down quark. The *charm* quark is also included in the second family and is a factor of 10 heavier than the strange quark. The third family includes the heaviest quarks, the *bottom* quark and the *top* quark, where the top quark has a similar mass as a gold atom.
All particles which are constructed from quarks, are known as *hadrons*. They can be differentiated by their quark content: *Mesons* contain a quark and an antiquark, while *baryons* contain three quarks (three antiquarks in the case of an anti-baryon). As quarks are fermions, they have to follow the Pauli Principle, two identical fermions need to differ in at least one property. To explain the wavefunction of the Δ^{++} baryon with a quark content *uuu* and spin $s = \frac{3}{2}$, an additional property needs to be added to position space, quark flavour and spin, namely the *color*. The total sum of the color always has to be white, analogue to the additive color composition. In view of the color composition, quark color is often chosen as red, green or blue for a quark, and the corresponding anti-color for an anti-quarks. Hadrons are always color-neutral.

The leptons are grouped into families as well. The first family contains the *electron* and the corresponding electron neutrino. The second family contains the *muon* and the *muon-neutrino*. The heaviest lepton, the τ-*lepton* is contained in the third family, which also includes the τ-*neutrino*. For the mass of the neutrinos only an upper limit can be extracted from the measured data, as can be seen in table 2.1.
The Standard Model also includes three forces: the *strong*, the *weak* and the *electromagnetic* force. As mentioned before, the forces are mediated by so called *exchange particles*, the *bosons* (with integer spin): the *gluon* (strong force), the *photon* (electromagnetic force) and the $W^{\pm}/Z^0$-bosons (weak force). Not included in the Standard Model is the fourth force, the *gravitation*, which is described by General Relativity Theory.
Recently, the *Higgs-Boson* has been added to the Standard Model. It has been measured by the *Large Hadron Collider* (LHC) (see sec. 3.1 for details) and is one of the publicly well-known results of the LHC. The Higgs-Boson has been theoretically predicted in 1964 by Brout, Englert [8] and Higgs [9] and is part of the so-called *Higgs-mechanism*, which can explain the masses at rest of the elementary particles. The fact, that hadrons are always color-neutral is also reflected in the potential of the strong interaction, which is given by

$$V(r) = -\frac{4}{3}\frac{\alpha_s\left(Q^2\right)\hbar c}{r} + k \cdot r \tag{2.1}$$

r here denotes the distance between qq, $q\bar{q}$ or $\bar{q}\bar{q}$, Q^2 the momentum transfer, k a constant and α_s the strong coupling constant, which depends on the momentum transfer between the partons. The momentum transfer dependence of the coupling constant is referred to as *running coupling*. The potential has two parts: at small distances, it behaves like a Coulomb potential, while for large distances the potential increases linearly. If the distance between quark and anti-quark increases, the energy in the potential is large enough to create a new quark-antiquark pair.

Fig. 2.1 shows the strong coupling constant as function of the momentum transfer Q. The datapoints show different measurements and extraction methods using model calculations of quantum chromodynamics. At high momentum transfers, the coupling constant reaches small values (*asymptotic freedom*), while the coupling constant is large in the opposite direction (*confinement*).
In case of quarks, they cannot be studied as single quarks due to their confinement in the hadrons. One possible way to overcome this disadvantage is to study particle production in high energy collision of hadrons like proton-proton (pp) collisions with large momentum

Quarks

Name	charge	mass
u	2/3 e	$2.3^{+0.7}_{-0.5}$ MeV/c^2
d	-1/3 e	$4.8^{+0.5}_{-0.3}$ MeV/c^2
c	2/3 e	1.275 ± 0.025 GeV/c^2
s	-1/3 e	95 ± 5 MeV/c^2
t	2/3 e	$173.21 \pm 0.51 \pm 0.71$ GeV/c^2
b	-1/3 e	4.18 ± 0.03 GeV/c^2

Leptons

Name	charge	mass
e^-	$-e$	0.511 MeV/c^2
ν_e	0	< 2 eV/c^2
μ^-	$-e$	105.7 MeV/c^2
ν_μ	0	< 0.19 eV/c^2
τ^-	$-e$	1776.82 ± 0.16 MeV/c^2
ν_τ	0	< 18.2 eV/c^2

Bosons

Name	force	couples to
Photon (γ)	electromagnetic	all charged particles
Gluon (g)	strong	quarks & gluons
Z^0,$W^\pm$	weak	quarks, leptons
Higgs-Particle (H)	Higgs-Field	all massive particles

Table 2.1.: The quark and lepton families as well as the bosons and their rest masses in the Standard Model of Particle Physics [10].

transfer, and such probing asymptotic free quarks. Furthermore, in high energy collisions of heavy-ions a so called *Quark Gluon Plasma* (QGP) is created, a deconfined system of quarks and gluons, where quarks and gluons are *quasi-free* for a short moment in time and space. As the QGP is the central focus of this work, it is discussed in more details in sec. 2.3. The particle production in high-energy proton-proton collisions can constrain fragmentation and hadronization processes[1] and can serve as a baseline to understand the particle production in heavy-ion collisions. Therefore, the understanding of particle production in pp collisions is essential to investigate particle production in heavy-ion

[1]Fragmentation and hadronization describe the probability of the creation of new hadrons after an inelastic proton-proton collision.

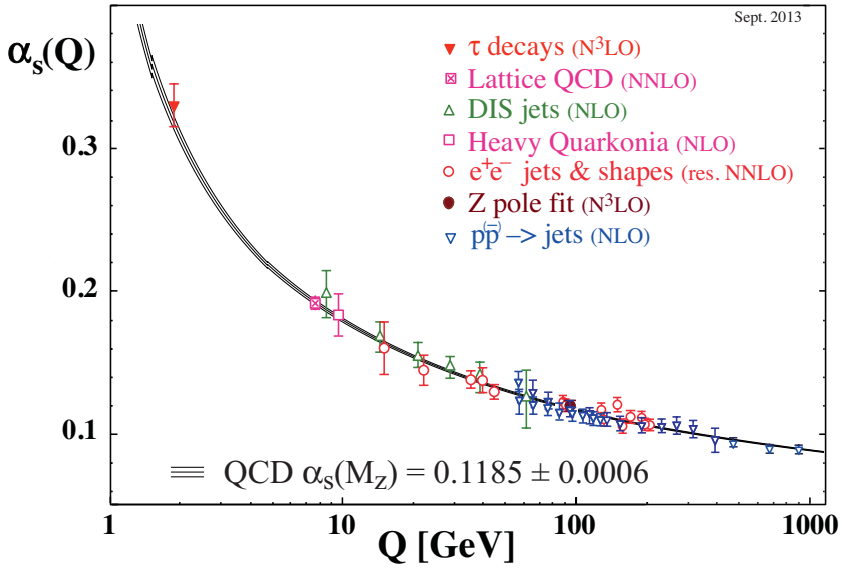

Figure 2.1.: Strong coupling constant α_s as function of the momentum transfer Q [10]. The datapoints show different model calculations based on measurements in pp collisions.

collisions. In the following, the particle production mechanisms in pp-collisions are briefly reviewed, which is followed by a discussion of particle production in the QGP.

2.2. Particle Production at High Collision Energies

If two protons collide at high energies, new particles are produced. The production mechanisms of these new particles in high energy collisions are usually categorized into two different types based on the transverse momentum of the created particles. At low p_{T} so-called *soft processes* dominate the particle production, while at high p_{T} so called *hard processes* play the most important role. In this section, the main differences between both types of processes and their influence on the total, i.e. the so called *inclusive*, particle production are discussed. In this work, the production of charged particles is investigated, therefore the discussion of the theoretical concepts focus mainly on charged particles. It should be stressed, that the production of other particles types cannot be neglected.

2.2.1. Soft Processes

Most of the particles produced in high-energy pp collisions are produced at low p_{T} and originate from soft processes. In these processes, the momentum transfer between the collision partners is small. Though these collisions dominate the total cross-section of all charged hadrons, their underlying description is difficult. To calculate the production rate of these particles (often referred to as *underlying event*) some of the so called *event generators* that are used in this work, e.g. Pythia [11], implement the exchange of a so-called *Pomeron*. A Pomeron denotes the effective summation of all possible exchange processes between a quark and a quark, a quark and a gluon or a gluon and a gluon (resp. the anti-particles). It has been introduced by Gribov, who implemented a prediction by Pomeranchuk (see [11] and ref. 2, 3 therein for details).
Basically, the total cross-section of the charged hadron production (further referred to as *hadronic cross-section*) is the sum of an elastic and an inelastic cross-section:

$$\sigma_{had,total} = \sigma_{had,el} + \sigma_{had,inel} \tag{2.2}$$

In case of an elastic pp-collision, the protons remain intact and are measured at beam-rapidity (*rapidity* is a lorentz invariant measure of a particle along the beam direction, see sec. C for details on the kinematics of a collision).
If an inelastic pp-collision occurs, the processes can be differentiated based on the type of the so called *diffraction* of the incoming protons. The Feynman-graphs of each diffractive process are shown in figure 2.2. Different colors represent different particle species. Black lines show the incoming protons, red double-lines the exchanged pomerons. An undiffracted proton is represented as a red single line, blue lines represent final state particles created in the collision.

The diffractivity of a process quantifies, if none, only one or both protons are diffracted and how the final state particles are distributed. In diffractive events an incident particle is excited. A so-called diffractive system is created that carries the quantum numbers of the respective incoming particle (except possibly the spin). Subsequently it evolves and decays. A measurement of the rapidity distribution of the particles can differ between each diffractive process:

- In **single-diffractive** processes, one proton remains intact at beam rapidity (it cannot be measured), while a signal, i.e. particles created in the collision, is seen in the opposite (forward or backward) direction.

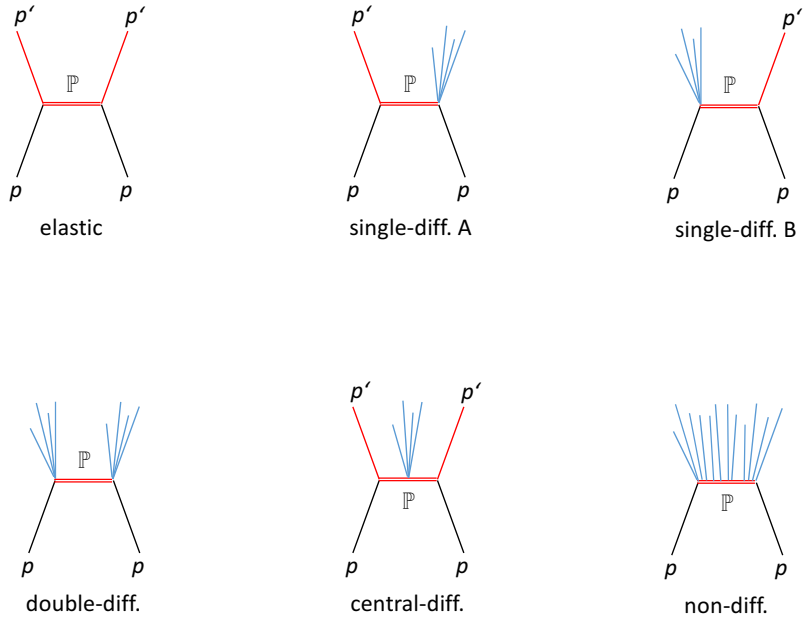

Figure 2.2.: Feynman-graphs for different types of diffractive proton-proton collisions. Black lines represent incoming protons, red double-lines are pomerons, red single lines are outgoing protons at beam-rapidity, blue lines represent final state particles created in the collision. Figure adapted from [11].

- In **double-diffractive** events, a signal is measured in forward and backward rapidity with a gap around mid-rapidity.
- **Central-diffractive** events are characterized by a signal around midrapidity, and two protons at beam-rapidity.
- The particles in **non-diffractive** events are distributed over the full rapidity range.

The total inelastic cross-section of charged hadrons $\sigma_{had,inel}$ is the sum of all different diffractive components:

$$\sigma_{had,inel} = \sigma_{single-diff,A} + \sigma_{single-diff,B} + \sigma_{non-diff} + \sigma_{double-diff} + \sigma_{central-diff} \quad (2.3)$$

The implementation of these soft processes in event generators and model calculations plays an important role how well they can describe the measured inelastic cross-section of charged hadron production in high energy collisions. In this work, transverse momentum spectra are used as a tool to test the implementation in the event generators. Specifi-

cally, the comparison in section 5.2 focuses on the description of the average transverse momentum $\langle p_{\mathrm{T}} \rangle$, as $\langle p_{\mathrm{T}} \rangle$ is sensitive to the particle production at low and intermediate p_{T}, where soft processes dominate the particle production. These comparisons can help to constrain the implementation of the soft processes in the event generators.

With higher momentum transfer between two colliding partons, the dominating underlying processes change from soft to hard processes. The main properties of these hard processes, their theoretical description and their modification in collisions of heavy-ions are discussed in the following.

2.2.2. Hard Processes

In particle production at high p_{T}, particles are produced in collisions of protons with a high momentum transfer, the particle production can be described by *perturbative quantum chromodynamics* (pQCD). In this case, the total inelastic cross-section of charged hadron production can be split into different parts, which are all independent; this is known as *factorization*. The total inelastic, lorentz-invariant cross-section of charged hadron production[2] is given by

$$E\frac{\mathrm{d}^3\sigma}{\mathrm{d}p^3} = K \sum_{a,b,c,d=q,\bar{q},g} \int_{x_{a,min}}^{1} \mathrm{d}x_a \int_{x_{b,min}}^{1} \mathrm{d}x_b f_a^{free}\left(x_a, Q^2\right) f_b^{free}\left(x_b, Q^2\right) \sigma_{ab\to cd} D\left(z_c, Q^2\right) \tag{2.4}$$

The three factors of this invariant cross-section $E\frac{\mathrm{d}^3\sigma}{\mathrm{d}p^3}$ are the *parton distribution function* (PDF) f^{free} of a free proton, the *cross-section of an elementary reaction* $\sigma_{ab\to cd}$, where a, b, c, d can be quark, antiquark or gluon, and the *fragmentation function* D. The PDF describes the probability to measure a parton at a certain momentum fraction x of the hadron[3]:

$$x = \frac{p_{parton}}{p_{hadron}} \tag{2.5}$$

Fig. 2.3 shows two exemplary parton distribution functions for free protons for two different squared momentum transfers $Q^2 = 10$ GeV^2 (left) and $Q^2 = 100$ GeV^2 (right).

[2] If not stated otherwise, *cross-section* in the following means *inelastic cross-section of charged hadron production* and *invariant cross-section* means *inelastic, lorentz-invariant cross-section of charged hadron production.*

[3] The momentum fraction is also known as *Bjorken-x.*

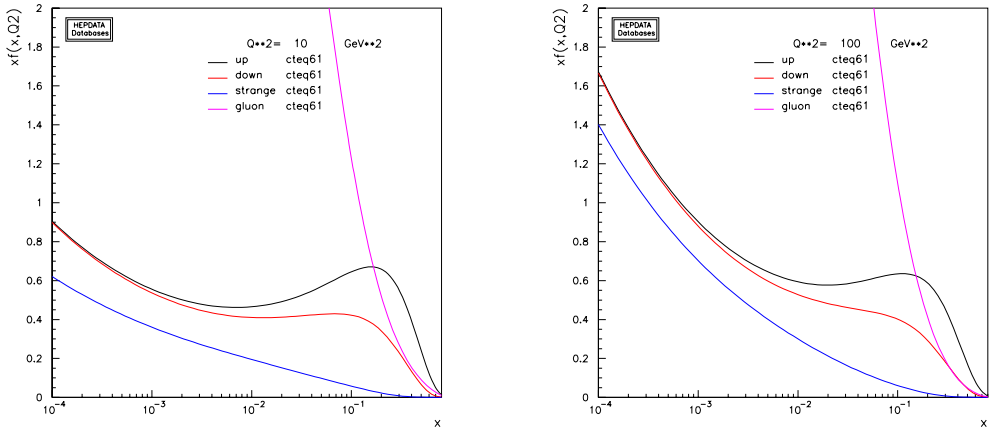

Figure 2.3.: Two exemplary parton distribution functions for free protons, left for $Q^2 = 10$ GeV^2, right for $Q^2 = 100$ GeV^2 (figures created with [12]).

Here, only the most abundant partons are shown (up, down and strange quarks as well as gluons) for the PDF set CTEQ6.1 ([13]).
At high x, the distribution function is dominated by the valence quarks, while at low x the fraction of gluons superseeds all quarks. An increase in the squared momentum transfer Q^2 results in a higher probability to find quarks at low x.
The elementary cross-section $\sigma_{ab\to cd}$ describes the probability, with which two new partons are created after a collision of two partons. Finally, the fragmentation function $D\left(z_c, Q^2\right)$ describes the transition of the partons to stable hadrons in the last stage of a collision, which is dependent on the momentum transfer Q as well as the momentum fraction x. Both, the PDF and the fragmentation function are measured in deep-inelastic collisions of electrons and protons.
For heavy-ion collisions factorization should still hold at high transverse momenta. As the protons and neutrons are bound in a nucleus, the PDF is modified. The nuclear PDF $f_i^{nucl}\left(x, Q^2\right)$ is modified relative to the PDF of a parton in a free proton $f_i^{free}\left(x, Q^2\right)$:

$$f_i^{nucl}\left(x, Q^2\right) \equiv R_i^A\left(x, Q^2\right) \cdot f_i^{free}\left(x, Q^2\right) \tag{2.6}$$

The parton species can be selected by the index i and can be a *valence quark*, *sea*

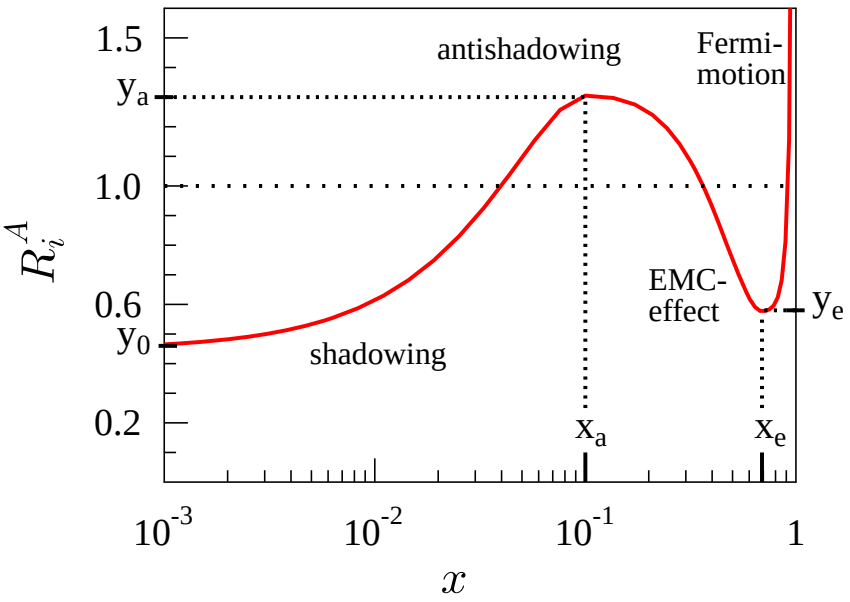

Figure 2.4.: Modification factor R_i^A [14].

quark or *gluon*. Fig. 2.4 shows the relative modification factor $R_i^A(x, Q^2)$ as function of x for a momentum transfer $Q^2 = 1.69$ GeV^2, which has been measured by various collaborations, e.g. the EMC-Collaboration and collaborations at AGS, which studied collisions in fixed-targed experiments. Four different effects can be distinguished in this modification:

- For $x \ll 0.1$ the nuclear PDF is suppressed compared to the PDF in a free proton. This is often referred to as *shadowing*.
- The excess at $x \approx 0.1$ acts into the opposite direction as the shadowing, it is named *anti-shadowing* and has its maximum at $(x_a|y_a)$.
- For $0.2 < x < 0.7$ a suppression of the nuclear PDF is observed, it is named the *EMC-effect* after the EMC-Collaboration. The minimum of the EMC-effect is at $(x_e|y_e)$.
- Nucleons bound in a nucleus can have a small energy of the order of $E \approx 30$ MeV. This energy results in the so-called *Fermi motion* of the nucleons, which causes a large excess in the nuclear PDF towards $x = 1$.

	RHIC	LHC	LHC
$\sqrt{s}$	200 GeV	2760 GeV	5023 GeV
$p_{\mathrm{T}} = 5$ GeV/c	0.025	0.002	0.001
$p_{\mathrm{T}} = 10$ GeV/c	0.050	0.004	0.002
$p_{\mathrm{T}} = 50$ GeV/c	0.250	0.018	0.010

Table 2.2.: Bjorken-x values for different energies at RHIC and LHC. For comparison, different p_{T} values are shown. The values have been determined with eq. 2.7, only measurements at $y = 0$ are taken into account.

An example of an advanced nuclear PDF has been developed by Eskola, Paukkunen and Salgado ([14], [15]). In this model, depending on x, different of the above mentioned processes come into play in pp, p–A or A–A collisions. The momentum fraction of each parton can be determined as

$$x = \frac{p_{\mathrm{T}}}{\sqrt{s}} \cdot e^{-y} \tag{2.7}$$

where y is the rapidity and $\sqrt{s}$ the available center-of-mass energy in a collision [16]. Depending on the center-of-mass energy of the collision for a given p_{T}, the nuclear PDF is probed at different momentum fractions. Table 2.2 shows the range of probed x, for a given center-of-mass energy for measurements at mid-rapidity ($y = 0$) for different p_{T}. At RHIC and LHC, measurements mainly probe the PDF at low x. This shows, that, especially at LHC, processes including a gluon (e.g. gluon-gluon or gluon-quark scatterings) dominate the particle production mechanisms. In addition, the probed x differs by one order in magnitude between RHIC and LHC.

2.3. Hot and Dense Medium

As discussed, the matter in the universe is built up by quarks, gluons and leptons. Quarks and gluons exist only in bound states (confinement). At high temperatures and/or high densities, the bound states of hadrons are dissolved and a new state of matter is formed, where quarks and gluons are no longer confined, the QGP. Shortly after the *Big Bang* the universe was in a phase, which is assumed to be the QGP. After the QGP phase, the

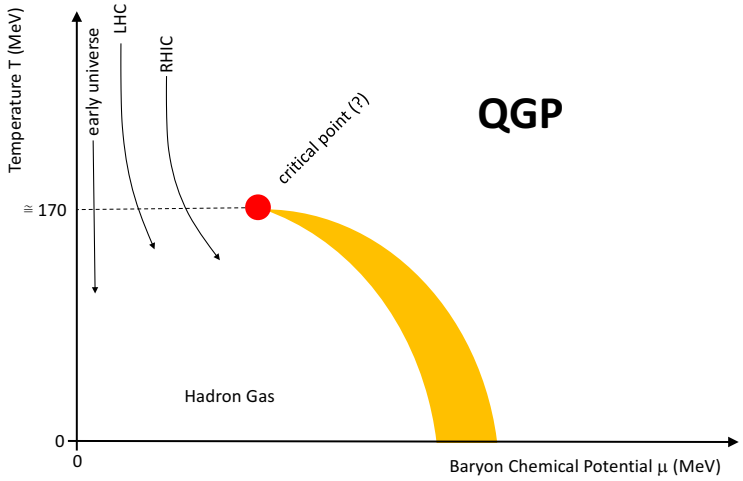

Figure 2.5.: The phase diagram of QCD matter.

universe expanded[4] and cooled down. During this cooling, the quarks and gluons built the hadrons, which later built stars and the surrounding planets. A detailed understanding of the properties of the QGP, the freeze-out and the building of hadrons will help to model the development of the universe and the formation of the visible world. To gain this understanding, the QGP needs to be created in a well-controlled setting. An often used setting are heavy-ion collisions, which are under study for many years now.
Fig. 2.5 shows a simplified sketch of the phase diagram of QCD matter (the temperature of the matter as function of the baryon-chemical potential μ). Three different paths which the QCD matter might undergo during its cooling are shown in the plot. At low μ and high T starts the path of QCD matter, which has been studied at RHIC in Au-Au collisions at $\sqrt{s_{NN}} = 200$ GeV. The higher the beam energy gets, the lower μ is probed (LHC). High energy accelerators (LHC and RHIC at top center-of-mass energies) aim to probe a μ very close to 0, where the path of the QCD matter in the early universe is expected to have happened. During the cooling down of the QGP, the plasma undergoes a phase transition (dashed line) or reaches a cross-over region (yellow area). The existence of a critical point at the end of the cross-over region is still under debate; the investigation of the QGP in heavy-ion collisions at different center-of-mass energies might help to solve this open question. Neutron stars are expected to probe low temperatures, but high μ, as gravitation compresses the hadrons to high densities.

[4] In the printed version, the order of the sentence was scientifically inaccurate; it is corrected in this version.

2.3.1. Signatures of the QGP

Already in the early 1970s [17], the study of heavy ion collisions to probe the properties of the Quark-Gluon Plasma has been proposed. Since then, different key signatures have been suggested; a selection will be presented in the following.

Electromagnetic Probes Photons and dileptons (a pair of a lepton and the corresponding anti-lepton) do not carry color charge. Hence they do not interact strongly with the QGP and outgo the QGP-medium unchanged. Photons from the initial hard processes can be used to characterize these processes. If a photon is produced back-to-back with a jet, i.e. a collimated spray of particles created in hard collisions, the total energy of the jet can be determined based on the measurement of the photon in the opposite direction of the jet. Thermal photons can give insight to the temperature of the QGP but cannot be measured directly; input from model calculations is crucial for this measurement. Dileptons are produced throughout all stages of the collision as well. In contrast to photons, dileptons are not blueshifted (as mass is lorentz-invariant), i.e. shifted to higher energies due to a boost from the expanding source, and help to constrain the parameters of the QGP. The low-mass dielectron production allows for a study of the in-medium properties of the light vector mesons as well as their production mechanisms in the vacuum.

Quarkonia The production of quarkonia (a bound state of a quark and an antiquark) and their melting in the QGP has been proposed by Matsui and Satz in 1986 as a signature of the QGP [18]. If a critical temperature T_C is reached by the formed state of matter, the associated production of quark and antiquark no longer forms a quarkonium, but can built heavy mesons. The critical temperature is different for different quarkonium states. If a specific quarkonium state is not observed, the binding energy of this state constrains the minimum temperature of the QGP.

Correlations The correlation function of two or more particles can be used to extract e.g. the size of the produced fireball. This technique, often referred to as *HBT* (from its developers Hanburry-Brown and Twiss [19]), was originally developed in astrophysics and later transferred to heavy-ion physics.

Fluctuations The production of particles and especially their multiplicity per event or mean transverse momentum per event is sensitive to the degrees of freedom of the QGP. The event-by-event fluctuations of these observables might change their characteristics close to or shortly after a phase-transition of the QGP.

Flow and jet quenching are the main signatures of the QGP discussed in this work and are therefore presented in more detail in the following sections 2.3.2 and 2.3.3.

2.3.2. Flow

The size of a Pb-nucleus is small compared to our visible world, but it cannot be neglected in a collision of two such nuclei. For simplicity in the following, a Pb-nucleus is assumed to be disc-shaped. One of the main parameters to characterize a Pb-Pb-collision is the so-called *impact-parameter* b, which is the shortest distance between the centers of the two nuclei. Together with the beam direction, the impact-parameter spans the so-called *reaction-plane* Ψ_R.
When two Pb-nuclei collide with $b > 0$, an almond-shaped overlap region is formed. The QGP is created only in this overlap region[5]. The spatial anisotropy of the QGP transforms into a momentum anisotropy of the quarks and gluons via multiple collisions. To measure this azimuthal anisotropic shape of the medium, the invariant cross-section of particle production is written as a Fourier expansion ([20], [21]):

$$E\frac{d^3N}{d^3p} = \frac{1}{2\pi}\frac{d^2N}{p_{\mathrm{T}}dp_{\mathrm{T}}dy}\left(1 + \sum_{n=1}^{\infty} 2v_n \cos\left[n(\phi - \Psi_{S,n})\right]\right) \tag{2.8}$$

Here, ϕ is the polar angle of each particle and $\Psi_{S,n}$ is the angle of the n-th order initial spatial symmetry plane[6]. The Fourier coefficients v_n are also called *flow magnitudes* and can in general be written as

$$v_n = \langle \cos\left[n(\phi - \Psi_{S,n})\right] \rangle \tag{2.9}$$

where $\langle\rangle$ indicates the average over all events and particles. In this specific expansion, all sine terms vanish due to the symmetry of reflection with respect to the reaction plane. In an experiment, the angles of the symmetry planes cannot be measured directly as the impact parameter cannot be measured. Instead, the so-called *event-plane* is determined from the measured angular distribution of particles. To determine the n-th order event-plane angle Ψ_n, the so-called n-th order *event flow vector* $\vec{Q_n}$ is calculated as:

$$\vec{Q_n} = \begin{pmatrix} X_n \\ Y_n \end{pmatrix} = \begin{pmatrix} \sum_i w_i \cos(n\phi_i) \\ \sum_i w_i \sin(n\phi_i) \end{pmatrix} \tag{2.10}$$

[5] An impact-parameter of $b = 0$ is possible but has a very small probability.
[6] The second order symmetry plane is the reaction plane: $\Psi_{S,2} = \Psi_R$

Here, ϕ_i is the polar angle of each particle and w_i a weighting factor, which is optimized for the highest resolution of the event-plane. The n-th order event-plane angle is defined as

$$\Psi_n = \frac{1}{n} \tan^{-1} \left(\frac{Y_n}{X_n} \right) \tag{2.11}$$

It is worth noting, that the n-th order event-plane angle ranges from $0 \leq \Psi_n < 2\pi/n$, which is attributed to the symmetry of the emission pattern.
The flow phenomenon assumes a hydrodynamical behaviour of the medium of interest, which is the case for the QGP. Fig. 2.6 shows a measurement of the flow coefficients as function of centrality measured by the ALICE collaboration [22]. The *elliptic flow* v_2 (shown as red markers) has its maximum for semi-central collisions, which is expected from the collision geometry: for semi-central collisions, the ratio of the semi-major axis to the semi-minor axis is largest and decreases both for more central and more peripheral collisions. If the parton density in a Pb-nucleus was evenly distributed within the nucleus, for $b = 0$ no elliptic flow would be expected.
Blue full markers represent the *triangular flow* v_3, which is smaller than v_2 and has only a weak centrality dependence. The blue open markers show $v_3\{4\}$. This calculation reduces the contribution from higher flow coefficents to v_3. As concluded in [22], the difference between $v_3\{2\}$ and $v_3\{4\}$ suggests, that v_3 is predominantly driven by event-by-event fluctuations of the initial geometry.
The correlation between v_3 and the reaction plane is weak, which is indirectly shown in Fig. 2.6 by the green and black markers. The markers show the size of the triangluar flow related to the reaction plane, which is zero within uncertainties.

2.3.3. Energy Loss in a QCD medium

In general, two different energy loss mechanisms have to be considered, when the energy loss in a QCD medium is discussed, namely the *collisional* and the *radiative* energy loss. The collisional energy loss is the dominant mechanism for the energy loss of partons at low p_{T}, where partons lose energy via collisions with the sorrounding medium particles. The latter is the main energy loss mechanism for partons at high transverse momenta, as is discussed in the following.
A high-energetic parton loses energy in a strongly interacting medium via gluon bremsstrahlung. Gluon bremsstrahlung is the emission of a gluon by the parton, if the parton is accelerated, i.e. the parton changes its flight path through the medium. The effect of gluon

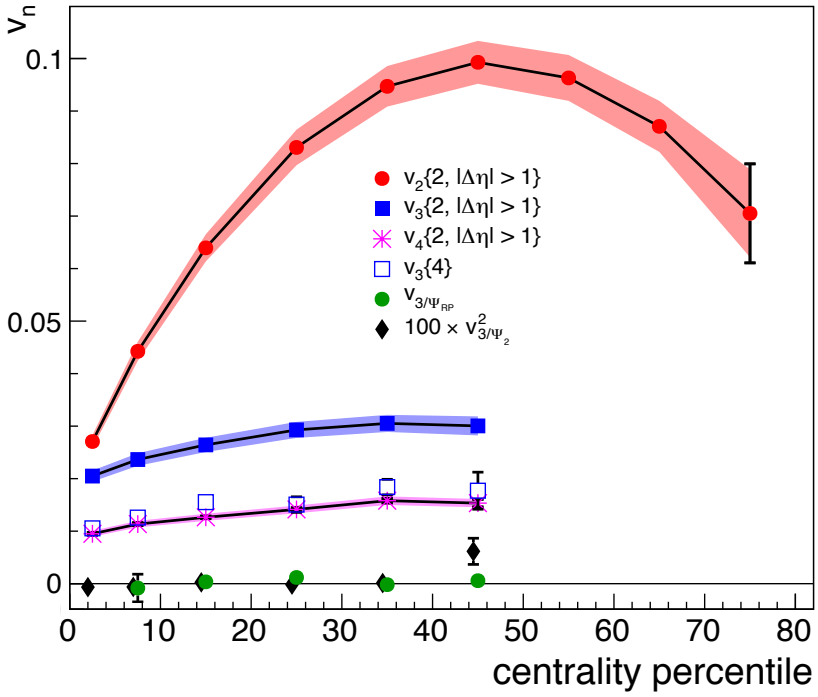

Figure 2.6.: Flow coefficients as function of centrality integrated over $0.2 < p_{\mathrm{T}} < 5$ GeV/c [22].

bremsstrahlung plays an important role for light quarks and gluons, as they can change their path through the QGP easily. For heavier quarks (c, b) the so-called *dead cone effect* reduces the gluon bremsstrahlung significantly. The dead cone effect describes the suppression of gluons radiated off the heavy quark at angles smaller than the ratio of the quark mass to its energy [7]. As a result of this suppression for heavy quarks, collisional energy loss is the main energy loss process for heavy quarks. An exemplary path of a light, hard parton in the QGP is shown in Fig. 2.7 in a schematic view. During its path, a gluon is radiated off the incoming parton. This gluon can scatter inelastically with the medium. As the strong coupling constant α_s is small in these scatterings, the interaction of the gluon and parton with the medium can be calculated with pQCD. The mean free path λ of the parton (i.e. the distance between the scattering centers) is much larger than the Debye screening length λ_D of the medium, which means, that the scattering centers are not correlated. Nevertheless, if the longitudinal momentum transfer of the gluon gets small, its corresponding wavelength increases. If the particle wavelength is larger than λ_D, the scattering centers cannot be treated separately and the gluons, which are radiated off the parton, interfere destructively. This effect, first proposed for QED processes by Landau and Pomeranschuk and modeled by Migdal and therefore named

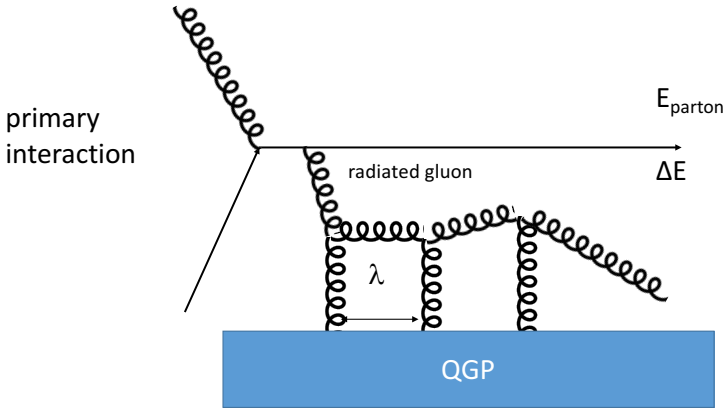

Figure 2.7.: A hard parton interacting with the medium via gluon radiation (figure adapted from [23]).

LPM effect, is applied in several QCD medium calculations (see e.g. [24]).
The expected energy loss ΔE in the energy loss regime where the LPM effect holds, depends quadratically on the path length L of the parton traversing the medium [25]:

$$\Delta E^{LPM} \approx \alpha_s C_R \hat{q} L^2 \tag{2.12}$$

The path length L can be determined with Glauber Monte Carlo simulations. C_R is the so-called *color factor* with $C_R = 4/3$ for quarks and $C_R = 3$ for gluons. The medium properties are mostly transcoded in the *average momentum transfer squared per unit path length* $\hat{q}$. As the implementation of the medium properties differs between models, a direct comparison between $\hat{q}$ at different energies is only meaningful within one model.

2.3.4. R_{AA}

The transverse momentum spectra of charged hadrons measured in Pb-Pb collisions can give insights into the particle production mechanisms at play. Of special interest is the modification of the spectra if a QGP is created in Pb-Pb collisions. To determine this modification, the so-called *nuclear modification factor* (R_{AA}) is used. The nuclear modification factor assumes, that the collision of two heavy ions can be treated as an

independent superposition of proton-proton collisions and is in general defined as

$$R_{\mathrm{AA}} = \frac{\text{yield per event in Pb-Pb collisions}}{N \cdot \text{ yield per event in pp collisions}} \tag{2.13}$$

Here, N is a scaling factor: In case of high p_{T} hadrons in the spectrum, the underlying hard collisions are expected to scale with the number of binary, i.e. hard, collisions of the partons in the protons, N_{coll}. N_{coll} is determined from Glauber calculations and not directly measurable. The inclusive R_{AA} can then be written as:

$$R_{AA,inclusive} = \frac{\frac{1}{n_{evts,AA}} N_{AA}}{N_{coll} \cdot \frac{1}{n_{evts,pp}} N_{pp}} \tag{2.14}$$

If no modification of the yield in Pb-Pb collision is observed, i.e. $R_{\mathrm{AA}} = 1$, the particle production in Pb-Pb collisions can be understood as a simple superposition of the particle production in pp collisions without any additional modification of the spectra due to a created medium. The average number of binary collisions N_{coll} is also given by the nuclear overlap function T_{AA} multiplied with the inelastic proton-proton cross-section σ_{inel}:

$$N_{coll} = T_{AA} \cdot \sigma_{inel} \tag{2.15}$$

R_{AA} can be extended to a more differential ratio of the number of particles per p_{T}, η, $\Delta\phi$ etc. produced in heavy-ion collisions compared to the same measurement in proton-proton collisions scaled with the number of binary collisions expected from Glauber simulations. The nuclear modification factor used in this work is defined as:

$$R_{AA}\left(p_{\mathrm{T}}, \Delta\phi\right) = \frac{\frac{1}{n_{evts,AA}} \frac{dN^3_{AA}}{dp_{\mathrm{T}} d\eta d\Delta\phi}}{T_{AA} \cdot \frac{1}{n_{evts,pp}} \frac{d\sigma^3_{pp}}{dp_{\mathrm{T}} d\eta d\Delta\phi}} \tag{2.16}$$

As discussed in the beginning of this section, different energy loss mechanisms are at play. They have different effects on the resulting R_{AA}, especially, as they can have different momentum dependencies included. In the following, a short summary of the momentum dependence of R_{AA} with different p_{T}-dependence scenarios based on [26] is presented. Here, the momentum loss Δp_{T} (which is for massless particles at midrapidity equivalent to ΔE) can have three different dependencies:

1. A **constant momentum loss** $\Delta p_{\mathrm{T}} = \kappa_{const}$ results in R_{AA} rising slowly towards $R_{\mathrm{AA}} = 1$.

2. A **linear momentum loss** $\Delta p_{\mathrm{T}} = \kappa_{const} p_{\mathrm{T}}$ results in a constant R_{AA}.
3. For **a logarithmic dependence** of the momentum loss $\Delta p_{\mathrm{T}} = \kappa_{log} \log(p_{\mathrm{T}})$ a similar shape of R_{AA} as for the constant momentum loss is expected.

It is worth to note, that the measured R_{AA} might include different energy loss mechanisms in different momentum regimes and therefore no clear distinction might be made. In addition, the measurement of inclusive charged particles includes different types of particles which have different momentum losses and therefore different R_{AA}. The inclusive transverse momentum spectrum in heavy-ion collisions is then a folding of the spectra of all particles, but will be dominated by the most abundant particles, i.e. π, K, p.
In addition to the absolut momentum loss Δp_{T}, the relative momentum loss $\Delta p_{\mathrm{T}}/p_{\mathrm{T}}$ can give insights into the energy loss mechanisms at play. Here, the relative momentum loss is used as proxy for the relative energy loss, which is not easily accessible.
The most recent measurements of R_{AA} before the start of the LHC have been obtained at the *Relativistic Heavy Ion Collider* (RHIC) at the Brookhaven National Laboratory on Long Island (see e.g. [27], [28]). These results, measuring the ratio between the particle production in Au-Au and p-p collisions at $\sqrt{s} = 200$ GeV, have shown a suppression of charged-particle production in heavy-ion collisions. As discussed previously, the existence of a critical point in the phase diagram of QCD matter is a current topic of research; a beam-energy scan might help here. First results from the beam-energy scan at RHIC are shown in Fig. 2.8. This study measured by the STAR experiment shows the nuclear modification factor of charged particles as ratio between central and peripheral collisions R_{CP} as function of p_{T} for all energies currently available at RHIC. The figure shows a clear evolution of the suppression of charged-particle production in heavy-ion collisions with increasing $\sqrt{s}$. The left panel shows the preliminary results of the STAR measurement. For energies $\sqrt{s} \geq 39$ GeV a suppression of the particle production is observed, which follows a similar pattern in all energies: an increase at low p_{T} is followed by a maximum at $p_{\mathrm{T}} \approx 2$ GeV/c, and R_{CP} decreases afterwards. For lower energies, an enhancement of the charged-particle production in Au-Au collisions is observed, which is largest for the lowest energies reported.
The right panel shows R_{CP} as a function of p_{T} at the same $\sqrt{s}$ obtained from simulations with HIJING [30] where no medium-induced jet quenching was performed. A clear distinction between different production mechanisms of charged particles could not be made [29].
Fig. 2.9 shows the first measurements of the nuclear modification factor of inclusive charged particles at $\sqrt{s_{NN}} = 2.76$ TeV with a measured pp-reference at the LHC measured

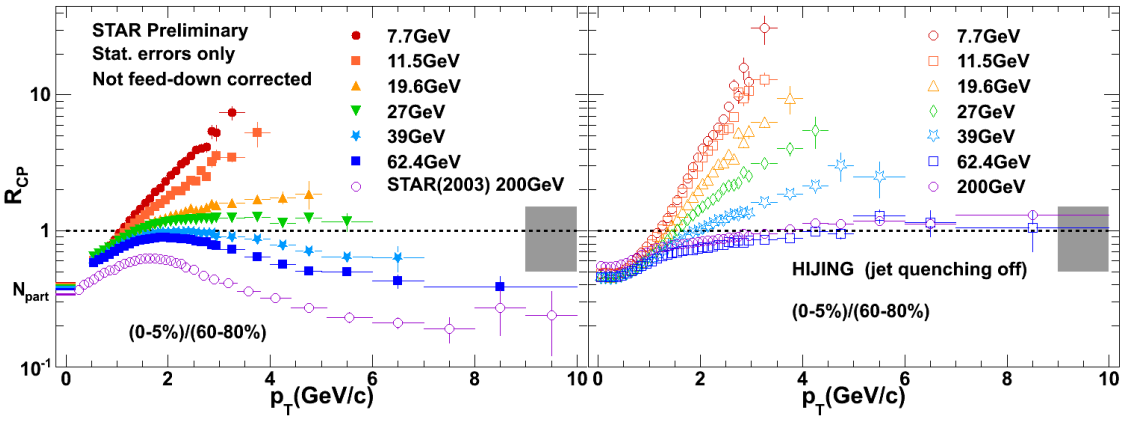

Figure 2.8.: Left panel: Preliminary results of R_{CP} measured by the STAR collaboration in a beam energy scan in Au–Au collisions at $\sqrt{s} = 7.7 - 200$ GeV. Right panel: R_{CP} at the same energies obtained from HIJING simulations without jet quenching. The gray error boxes at unity represent in both panels the uncertainty of N_{coll}. [29]

by ALICE and CMS. The measurements are represented as markers, red markers show the ALICE result, while black markers represent the CMS measurement. The lines show a variety of model predictions. All of these models are tuned on measured data at RHIC and where available before the preliminary results of the measurement at the LHC. While all models describe the data reasonably well, their underlying mechanisms differ: most of the models (expect WHDG) include a hydrodynamic description of the medium, interference effects of the gluon radiation are included in WHDG, ASW and HT. In addition, the extrapolation of the model parameters from the RHIC results as well as the included nuclear PDF are different between models. All models show a rise of R_{AA}, which can be traced back to the decreased relative energy loss with p_{T}. A more systematic study of all models, including comparisons to other observables, such as the particle production of identified particles or the elliptic flow is a current topic of research to confirm or rule out different energy loss mechanisms or medium descriptions.

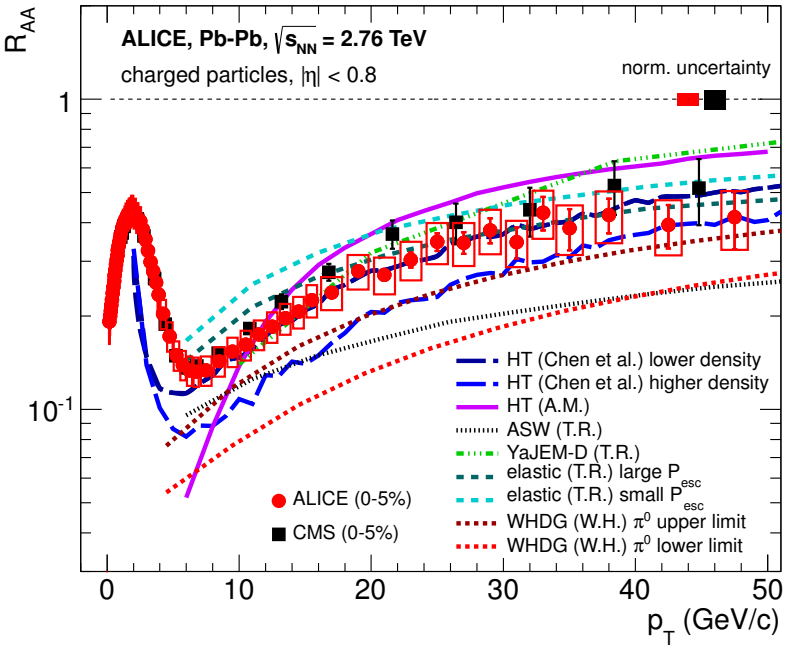

Figure 2.9.: Nuclear modification factor as function of the transverse momentum for charged particles measured by ALICE at $\sqrt{s_{NN}} = 2.76$ TeV (red markers) together with results from the CMS collaboration (black markers). Lines represent predictions from models (see text for details). Fig. published in [3], model reference therein.

Chapter 3.

The Experiment

3.1. Large Hadron Collider

The Large Hadron Collider (LHC), as the largest particle collider in the world, is located close to Geneva, Switzerland, at the European Organization for Nuclear Research (CERN). The LHC is built 50 - 100 m underground in a tunnel which has been previously used for the Large Electron Positron Collider and has a circumference of 27 km. The LHC can accelerate protons from beam energies of 450 GeV to up to 6.5 TeV (status 2016), which results in collision energies of $\sqrt{s} = 0.9 - 13$ TeV for pp collisions. Besides protons, lead ions can be accelerated in the LHC. Their kinetic energy is given by

$$E_{ion} = E_p \cdot \frac{Z_{ion}}{A_{ion}} \tag{3.1}$$

where E_p is the energy of a proton, Z_{ion} the electric charge and A_{ion} the mass of the ion. In case of a Pb-nucleus, the ratio $Z_{ion}/A_{ion} = 82/208$ leads to collision energies of $\sqrt{s_{NN}} = 5.02$ TeV for maximum beam energy. The particles are accelerated by accelerator cavities in the LHC tunnel. Bunches of particles (protons or Pb nuclei) are kept inside the circular beam pipe by strong dipol magnets. For beam focusing and tuning, more complex magnets (quadrupole, sextupole type) are used as well. The radio frequency of the accelerator cavities as well as the field setting in the dipol magnets define the possible beam energy. Fig. 3.1 shows a schematic view of the LHC accelerator complex. Low-charged ions (or protons) are extracted from their respective sources. All electrons are stripped off using stripper foils. Before being accelerated in the Proton Synchrotron (PS), protons and Pb-ions are accelerated differently. Protons are accelerated to $E = 1.4$ GeV in the booster and then injected to the PS, where they are accelerated to $E = 25$ GeV

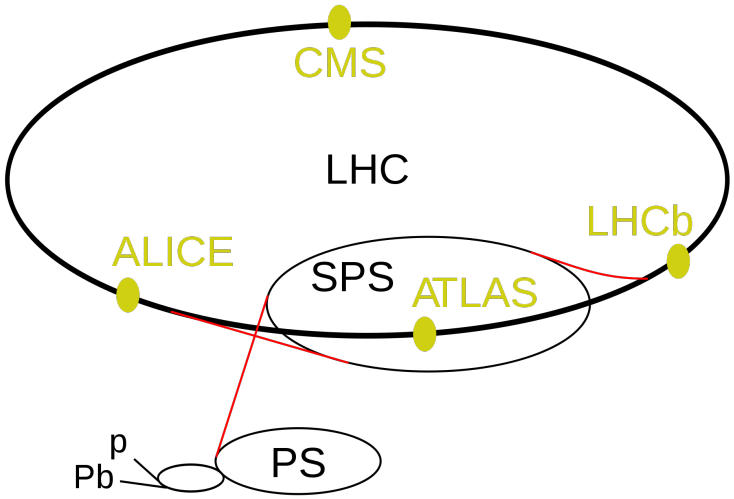

Figure 3.1.: Schematic view of the LHC accelerator complex [31].

followed by the acceleration to $E = 450$ GeV in the Super Proton Synchrotron (SPS). Finally, they are injected in the LHC and collide in the experiments with collision energies of up to $\sqrt{s} = 13$ TeV (pp) or $\sqrt{s} = 5.02$ TeV (p–Pb, Pb–Pb). Differently from protons, the Pb-ions are not stripped completely when injected in the PS. The PS accelerates the ions (mostly charge state Pb^{54+}) to $E = 5.9$ GeV/u. Before arriving in the SPS, the ions are stripped completely to a charge state Pb^{82+}. The SPS accelerates the ions to $E = 177$ GeV/u, at which energy they are injected into the LHC and accelerated to the final collision energy.

3.2. ALICE

ALICE (A Large Ion Collider Experiment) names one of the four large experiments located at the LHC. It is placed underground at the interaction point *Point 2*. While the beams are focused for ATLAS and CMS to have high interaction rates, for ALICE the bunches need to be defocused, as similar high rates can currently not be handled easily by the experimental setup.

ALICE is designed as a multi-purpose experiment and therefore hosts different detector techniques. A detailed description of the experiment can be found in [32]; in this chapter only the detectors relevant for this work are briefly introduced. The basic layout of ALICE can be split into two parts: the central barrel of the experiment located inside

a large magnet and the forward muon arm. The magnet, already in use at the L3 experiment at LEP, provides a solenoidal magnetic field of $B = 0.5$ T. For all charged particles in this magnetic field the Lorentz force F_L is of the same size as the centripetal force F_c:

$$\vec{F_c} = \vec{F_L} \tag{3.2}$$

$$\frac{m|\vec{v}|^2}{\vec{r}} = q \cdot \vec{v} \times \vec{B} = q \cdot |\vec{v}||\vec{B}| \sin\alpha \tag{3.3}$$

If the velocity vector and the magnetic field are perpendicular this leads to:

$$\frac{m|\vec{v}|^2}{|\vec{r}|} = q \cdot \vec{v} \times \vec{B} = q \cdot |\vec{v}||\vec{B}| \tag{3.4}$$

$$\Rightarrow |\vec{p}| = q \cdot |\vec{r}||\vec{B}| \tag{3.5}$$

where $|\vec{r}|$ is the radius of the curvature of each particle, q the electric charge of the particle and $|\vec{B}|$ the magnetic field.
As the electric charge cannot be measured in ALICE directly, equation 3.5 is usually written in terms of the rigidity p/z, where z is the number of elementary charges of the particle:

$$|\vec{p}| = q \cdot |\vec{r}||\vec{B}| \tag{3.6}$$

$$|\vec{p}| = ze \cdot |\vec{r}||\vec{B}| \tag{3.7}$$

$$\frac{|\vec{p}|}{z} = e \cdot |\vec{r}||\vec{B}| \tag{3.8}$$

This connection between the radius of the particle trajectory, which is measured, and the momentum of the particle allows for a determination of the momentum of the particle, if the magnetic field is known precisely. The higher the accuracy of the spatial measurement of the particles curvature, the higher the momentum resolution.

3.2.1. Detectors

As layed out, ALICE is designed as a barrel-type particle detector with a muon arm in forward direction (see fig. 3.2 for a schematic view of the experimental setup). Each detector-component in ALICE is dedicated to a specific task. To measure the track of a charged particle created in a pp or heavy-ion collision and traversing the different detectors of the experimental setup, the local space points of the detector signal (hits)

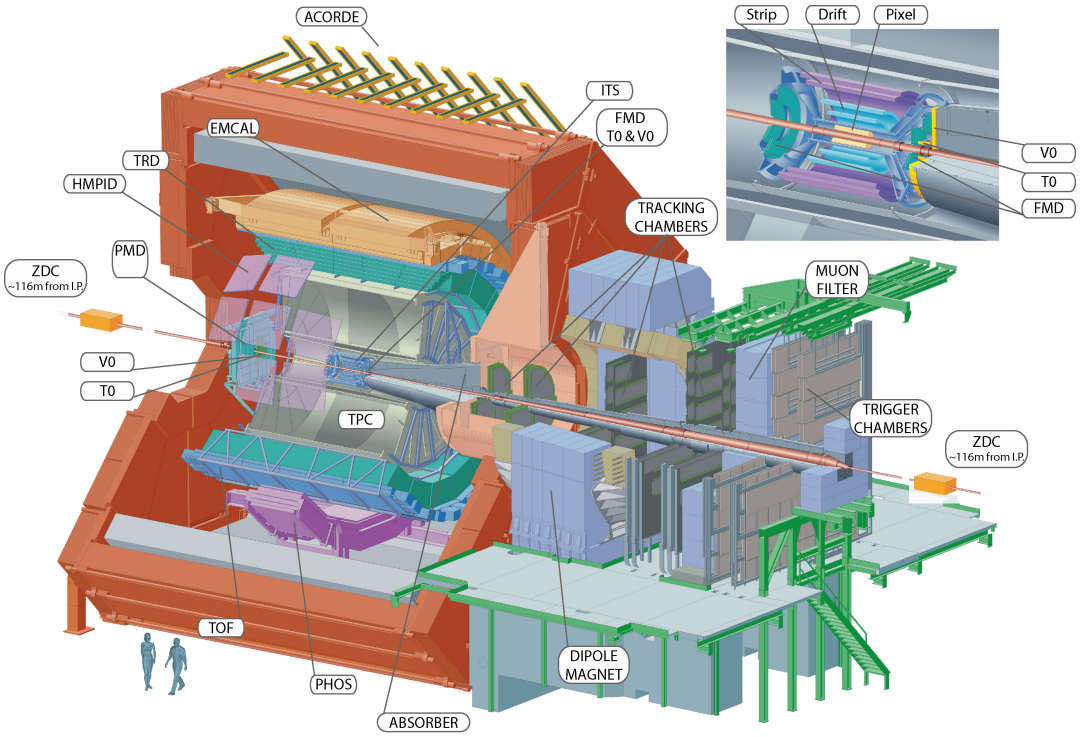

Figure 3.2.: Schematic view of the ALICE setup.[32]

along the track are connected by a computer algorithm. This procedure, the so-called *tracking*, will be explained in a separate section after a brief introduction of the detector and their setup. The **Inner Tracking System** (ITS) as the innermost detector and the **Time Projection Chamber** (TPC) as the largest tracking device in the setup will be explained in two separate sections. Going outwards from the ideal interaction point inside ALICE, the ITS and the TPC are followed by the **Transition Radiation Detector** (TRD). Its main purpose is the separation of electrons from pions and it adds additional space points for the tracking of particles. The TRD is based on the so-called *transition radiation*, the production of X-ray photons by the incoming particles. The TRD is followed by the **Time-of-Flight Detector** (TOF), which can identify charged particles via their specific time-of-flight from the primary interaction vertex. The TOF consists of various multigap resistive plate chambers. In particular, TOF is often used together with the TPC to cover a wider range in particle momentum for particle identification (PID). The **High Momentum Particle Identification Detector** (HMPID) can extend the track-by-track PID for pions and kaons up to $p \approx 3$ GeV/c and for protons up to $p \approx 5$ GeV/c in $\approx 5\%$ of the accessible phase space of particles in the central barrel. It is based on the so-called *Ring Imaging CHerenkov* technique (RICH), where particles can be identified by their velocity inside a medium. Photons are measured in the

two calorimeters of ALICE. The **Electromagnetic Calorimeter** (EMCal) measures photons and other electromagnetically interacting particles via electromagnetic showers. The **Photon Spectrometer** (PHOS) as the second calorimeter in ALICE is designed to measure photons with high spatial and energy resolution. It consists of highly granulated lead-tungstate crystals, which are followed by photomultipliers. Located at the endcaps of the ITS, the **V0 detector** is designed to measure particle multiplicity distributions at forward and backward rapidity. It can also help to determine event specific quantities, e.g. the event-plane, an ALICE-wide reference multiplicity or the collision centrality of an event; an independent measurement in the V0 can reduce autocorrelations when measuring the primary quantity in the TPC. The centrality of a collision can also be measured in the **Zero Degree Calorimeter** (ZDC), which is designed to measure the spectator particles of a heavy-ion collision. It consists of four calorimeters, two for the measurement of neutrons, and two to measure protons. The **Muon Arm** is located in forward direction and is not part of the central barrel detector setup. It consists of four main components. Nearly all particles which are not muons are excluded from the measurement with *absorbers*. The remaining particles are nearly only muons, which are measured in the *muon tracking chambers*. A *dipole magnet* bends the tracks, which allows for a measurement of the momentum of the particles. Separate *trigger chambers* allow for a fast triggering within the muon arm.

3.2.2. Inner Tracking System

The Inner Tracking System (ITS) consists of three different detector techniques, all based on silicon detectors. As the two innermost of the six layers, a **Silicon Pixel Detector** (SPD) is used, followed by two layers of a **Silicon Strip Detector** (SSD). The last two layers form **Silicon Drift Detectors** (SDD).
The ITS is located in the central barrel around the expected primary vertex of the collision. All six layers cover a pseudorapidity of $|\eta| < 0.9$ (SDD, layer 3 and 4) up to $|\eta| < 1.4$ (SPD, layer 1) and can measure charged particles down to low momenta of $p_{\mathrm{T}} \approx 150$ MeV/c. Besides tracking information, the SSD and SDD add information about the energy loss of particles, which helps to identify the particles. The high granularity of the ITS is used to identify weakly decaying particles via the reconstruction of the secondary vertex close to the primary interaction vertex. Figure 3.3 shows the layout of the ITS. The detection efficiency of the ITS was reduced in the beamtime in 2011 in comparison to the Pb-Pb beamtime in 2010 due to technical problems in the SPD. In

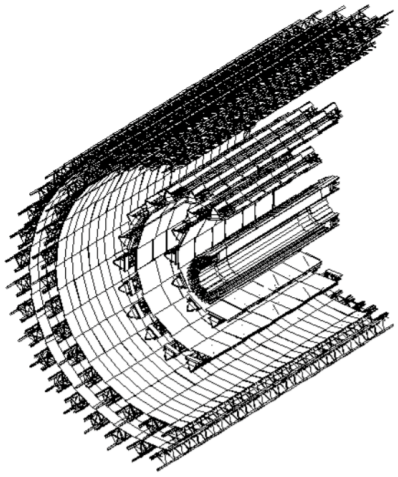

Figure 3.3.: Schematic layout of the ALICE-ITS [33].

the analysis described later, this affects the efficiency correction of the tracks of charged particles, which can be overcome by requiring hits in the SDD during the tracking process.

3.2.3. Time Projection Chamber

The large Time Projection Chamber (TPC) as the main tracking detector in ALICE is located around mid-rapidity. The TPC measures tracks from $p_{\mathrm{T}} \approx 100$ MeV/c up to $p_{\mathrm{T}} = 100$ GeV/c with a good momentum resolution. Additionally, particles can be identified based on their specific energy loss per unit length dE/dx in the TPC gas. During the beamtime in 2011, the TPC was filled with a $NeCO_2$ gas mixture. A central electrode splits the volume of the TPC in two subvolumes which are read out separately. Particles which traverse the read-out gas ionize the read-out gas. The electrons drift in the electric field of the detector to the end-caps of the TPC, where the signals are read out with multi-wire proportional chambers. While the electrons travel through the gas volume, additional gas atoms are ionized. Based on the time and position of the arrival of these clusters of electrons, the paths of particles can be reconstructed and tracks can be determined. The remaining ions travel much slower than the electrons to the central electrode, where they are absorbed. Fig. 3.4 shows the layout of the TPC. For the upcoming LHC-Run 3, the MWPC at the endcaps of the TPC will be replaced by *Gas*

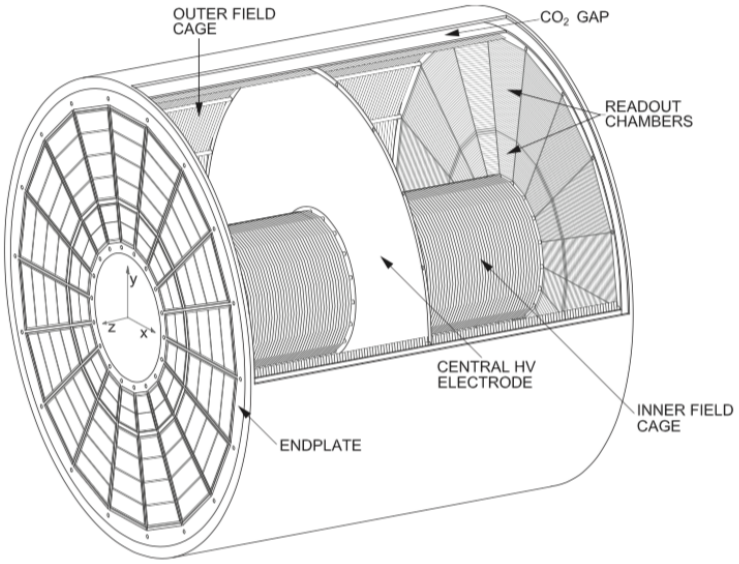

Figure 3.4.: Schematic layout of the ALICE-TPC [34].

Electron Multiplier (GEM), which shall enable the TPC to measure collisions at higher interaction rates. In addition, the read-out gas has been changed from neon to argon, which will increase the possible readout speed for the upcoming LHC beam-times.

3.3. Tracking

As briefly discussed, in the analysis of particle collisions, the term *tracking* means connecting all detector hits of a singe particle created in a collision to one track to determine the flight path of the particle. In ALICE, this flight path is described by a helix-type function which needs five parameters to describe the full track of each particle, namely the local y-coordinate of a track, the local z-coordinate of the track, the track momentum azimuthal angle, the track momentum inclination angle and the inverse of the transverse momentum. In the tracking analysis in ALICE, the so-called *Kalman-filter* algorithm is used. This recursive algorithm uses the current measurement of a hit position to predict the next measured point; based on the difference between the prediction and the real measured point, the Kalman-Filter updates its prediction procedure. The algorithm starts from a given point measured in e.g. the TPC and looks for the next point on the potential path of each particle in a given search window.
Based on the different detectors available for the tracking of the particles produced in the collisions and the track quality cuts applied in the analysis, different types of tracks

can be selected. This work focuses on the measurement of the transverse momentum of primary charged particles up to the highest p_{T} possible. Therefore, tracks are required to have a large traversing length in the TPC as well as a precise constraint to the primary vertex, which is achieved by requiring a track-matching between the TPC and the ITS; these tracks, based on the *combined TPC-ITS tracking* are called *long tracks*. Due to unstable conditions in the ITS in the data taking period 2011, an additional group of tracks is added to the data sample, the so-called *hybrid tracks*. These tracks require the same detectors as the long tracks, but instead of at least one hit in the SPD, one hit in the SDD is required to ensure a good pointing to the primary vertex.

Chapter 4.

Data Analysis

In this work, data of Pb-Pb collisions from the LHC run 2011 is analyzed. The focus lies on the extraction of the transverse momentum spectra of charged particles and their suppression compared to pp collisions. Here, parts of the analysis technique have been changed relative to previous publications on a similar topic based on a different data set, i.e. the first heavy-ion data set measured with ALICE in 2010. To investigate the influence of these changes, especially the main correction procedure, on the spectra and to point out potential differences between the two analyses, in the following, various comparisons of the two analyses along the analysis chain will be presented.
In the subsections of this chapter, the analysis procedure including the analysis steps from raw data to fully corrected spectra is discussed. The chapter is structured as follows: a general description of the reconstruction process in the first subsection is followed by a discussion of the event analysis in the second section, where the centrality determination as well as the event-plane extraction are explained. The third section discusses the quality assurance done in this analysis. The last section describes the track corrections, namely the efficiency and acceptance correction, secondary contamination correction and the p_{T} resolution correction.

4.1. Data Reconstruction

This work uses data which has been recorded in the data taking period LHC Run I. The measured detector hits have been connected to tracks during the so-called *reconstruction*. To reduce file sizes and computing time on the GRID, the data has been prefiltered. In this filtering process, a set of basic track requirements and event cuts has been applied

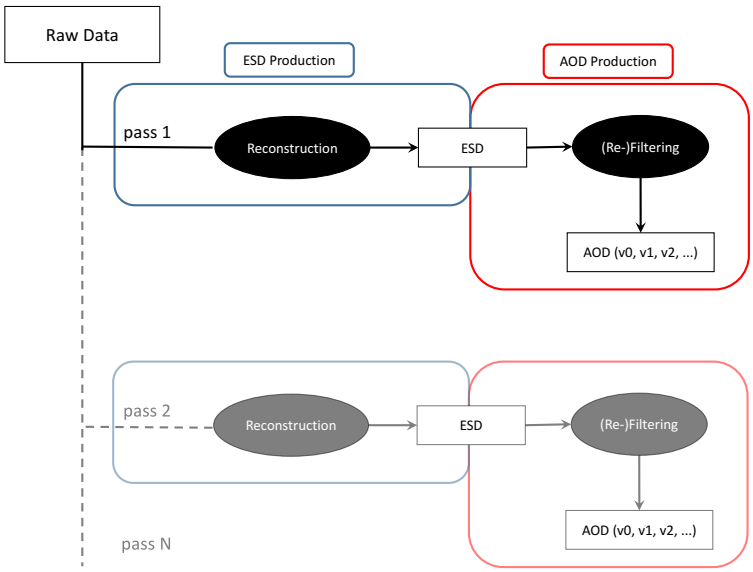

Figure 4.1.: Schematic view of different steps performed during the reconstruction and filtering of the raw data, which end in the AOD file type.

to store only tracks and events which fulfill a minimum quality for all analyses. The tracks are stored in the so-called *AOD* (Analysis Object Data) file format. Each track gets filter-bits assigned on which a fast preselection of the tracks can be performed in an analysis (see table B.1 for a summary of the analyzed filter-bits).
The steps of the creation of the AOD from the measured raw data are shown in Fig. 4.1 as schematic view. The measured raw data is reconstructed on the GRID and so-called *ESDs* (Event Summary Data) are created. During this reconstruction process, a first filtering of tracks is performed and first AOD files (v0) are created directly after the creation of the ESDs. As analyses in ALICE are in continuous update, the requirements on the AODs change with time. This is taken into account by re-filtering of the ESDs, which creates additional generations of AODs. A new set of ESDs (the so-called *reconstruction passes*) is generated, if an update of the reconstruction software includes important changes. Several crosschecks on a subset of the reconstructed events are performed before the reconstruction of the complete data-set is performed to identify open issues in the reconstruction algorithms or the detector calibration. If a new reconstruction pass is needed, all previous AODs become obsolete.
The basic steps of the analysis procedure after the reconstruction of the measured detector hits are shown in Fig. 4.2. In a first step, the event specific quantities such as centrality and the event-plane angle are obtained from the general analysis in ALICE. As the efficiency, secondary contamination and p_{T} resolution correction are different for every

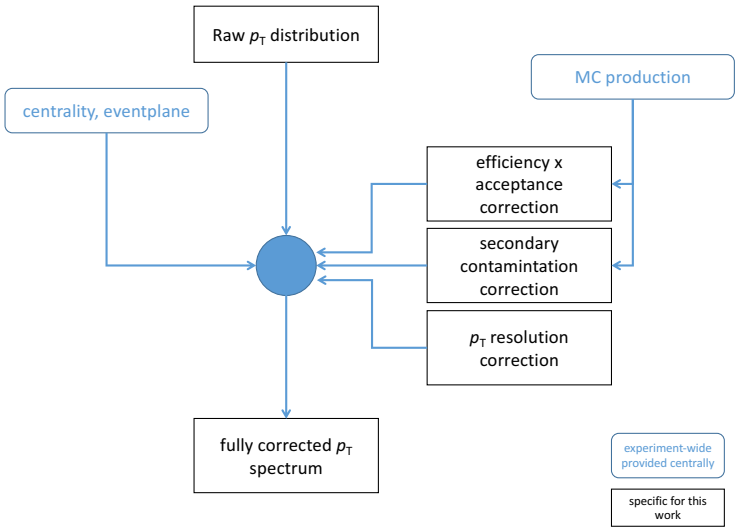

Figure 4.2.: Schematic view of the different analysis parts needed for a fully reconstructed spectrum as done in this work. Blue boxes represent experiment-wide, centrally provided parts while black boxes denote the parts, which are specific for this work.

analysis, they cannot be determined centrally and therefore have to be developed in this work. The efficiency and acceptance correction as well as the secondary contamination correction are determined in this work using input from a centrally produced MC sample, which is anchored, i.e. use the same detector conditions as during the measurement, to each data taking period. The p_{T} resolution in this work is calculated with a purely data-driven approach.

4.2. Event Analysis

In this work, the collisions of heavy-ions are studied. Each single collision has characteristic properties such as e.g. its collision vertex position that are important for the further analysis. In the following, the determination of the most relevant event properties and event selection criteria for this work are discussed.

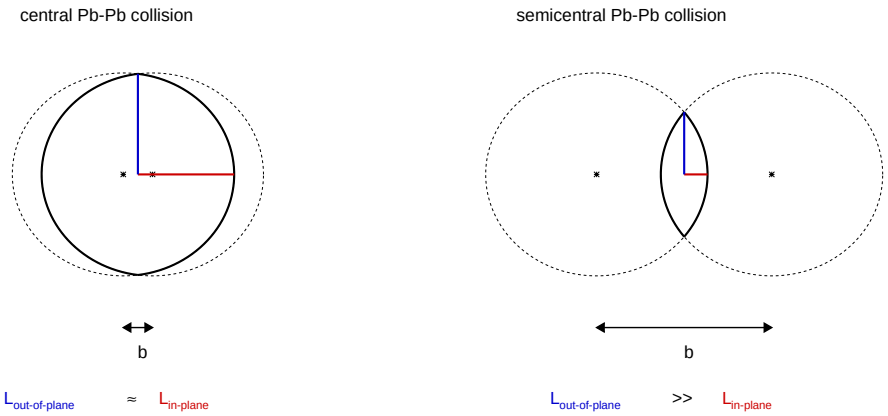

Figure 4.3.: Collision geometry for two different situations. **Left**: Central collision. **Right**: Semicentral collision.

4.2.1. Event Selection

In the analysis, all events need to pass an event selection, which includes events in the analysis based on their characteristic properties. An event is accepted, if the z-vertex position v_z relative to the center of the central barrel of the ALICE detector fulfills

$$|v_z| < 10 \text{ cm} \tag{4.1}$$

This means, that the collision happens in the center of the detector and tracks are measured in the detectors of the central barrel. Furthermore, a minimum of one track is required to contribute to the determination of the primary vertex position; in case of Pb-Pb collisions with centralities of 0-80 %, all events fulfill this requirement. This requirement becomes more important for an analysis in pp collisions for the determination of the inclusive inelastic cross-section and is included in a publication of the data measured in pp collisions [35]. In addition, the event needs to be selected by a central, semi-central or minimum bias trigger deployed by the V0 detector and the ITS. All events, which pass this event selection, are used in this analysis.

4.2.2. Centrality Determination

Depending on the collision geometry, the overlapping area of the two lead nuclei differs. The overlap region is defined in terms of the *impact parameter* b, which quantifies the

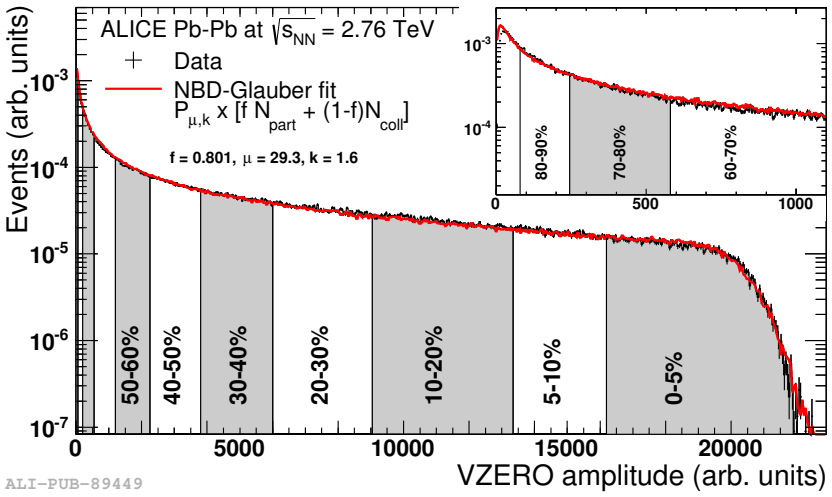

Figure 4.4.: Probability distribution of the V0 amplitude for Pb-Pb collisions at $\sqrt{s_{NN}}$ = 2.76 TeV. In addition, a parametrization with a negative binomial distribution of the measured data is shown, which is used as input for the Glauber MC model. [36]

distance between the center of each nucleus. Fig. 4.3 shows the schematic collision geometry for central and semi-central collisions, together with the impact parameter and the path-length L which a particle created in the center of the overlap-area would travel through the medium. Experimentally, the impact parameter is not accessible directly. To be able to select events based on the impact parameter, a measurable quantity which has a high correlation between centrality and impact parameter needs to be coupled to a model prediction from which the impact parameter of the collision can be determined for a given so-called *centrality class*. In this work, the centrality classes are determined by the measured multiplicity (i.e. amplitude) distribution in the V0 detectors (Fig. 4.4). This distribution is subdivided into parts, where events in the top 5% of the distribution correspond to the centrality class 0 - 5%, the next 5% of events correspond to the centrality class 5 - 10% and so on. ALICE provides the centrality determination experiment-wide together with the corresponding impact parameter values as well as values for the nuclear overlap function T_{AA} and the number of collisions N_{coll}. These values are determined with a Glauber MC, which is tuned such, that the measured multiplicity distribution in the V0 detector is described by the MC. Based on this Glauber MC, an impact parameter distribution corresponding to the measured multiplicity distribution can be extracted. In the Glauber approach, it is assumed, that the nucleons of the nucleus travel on straight lines. Two nucleons collide, if the distance d between the two nucleons is smaller than $\sqrt{\sigma/\pi}$, i.e. the two nucleons can be surrounded by a circle with the area σ, which describes the inelastic nucleon-nucleon

Centrality	b	T_{AA}	N_{coll}
0 - 5 %	0.00 - 3.50	26.32 ± 2.64 ± 1.91	1684.40 ± 169.23 ± 424.76
5 - 10 %	3.50 - 4.94	20.56 ± 1.70 ± 0.67	1316.00 ± 110.00 ± 140.00
10 - 20 %	4.94 - 6.98	14.39 ± 1.85 ± 0.64	920.90 ± 121.10 ± 135.39
20 - 30 %	6.98 - 8.55	8.70 ± 1.47 ± 0.39	556.65 ± 93.00 ± 77.01
30 - 40 %	8.55 - 9.88	5.00 ± 1.14 ± 0.26	320.05 ± 73.34 ± 43.12
40 - 50 %	9.88 - 11.04	2.67 ± 0.85 ± 0.18	171.25 ± 53.81 ± 22.55
50 - 60 %	11.04 - 12.09	1.32 ± 0.58 ± 0.10	84.28 ± 36.84 ± 9.75
60 - 70 %	12.09 - 13.05	0.59 ± 0.36 ± 0.05	37.86 ± 23.13 ± 4.01
70 - 80 %	13.05 - 13.97	0.24 ± 0.21 ± 0.02	15.57 ± 13.49 ± 1.45

Table 4.1.: Centrality intervals used in this work with the corresponding impact parameter b, nuclear overlap function T_{AA} and number of collisions N_{coll}. The geometric parameters have been obtained in a Glauber MC tuned on measured data.

cross-section. Alternatively, other detectors can be used to determine the centrality of a collision as well (e.g. the ZDC or the TPC), but are not used in this work. The resulting centrality intervals as well as values based on the Glauber MC are shown in Tab. 4.1; the experiment-wide determination of these values ensures a comparability of results from different analyses.

4.2.3. Event-plane Extraction

The determination of the event-plane has been discussed in section 2.3.2. It is based on the event flow vector

$$\vec{Q_n} = \begin{pmatrix} X_n \\ Y_n \end{pmatrix} = \begin{pmatrix} \sum_i w_i \cos(n\phi_i) \\ \sum_i w_i \sin(n\phi_i) \end{pmatrix} \tag{4.2}$$

which components are used to determine the event-plane angle of the n-th order

$$\Psi_n = \frac{1}{n} \tan^{-1} \left(\frac{Y_n}{X_n} \right) \tag{4.3}$$

In the following, the specific implementation of the determination of the second order event-plane angle Ψ_2 in ALICE is discussed. As the calculation of the event-plane angle consumes high computing times, the event-plane angle for each event is provided centrally

in ALICE. For the determination of the event flow vector only the angle ϕ_i of tracks in the TPC with the following criteria are used:

- $0.15 < p_{\mathrm{T}} < 20$ GeV/c
- $|\eta| < 0.8$
- for AOD analyses: filter bit 128 is required (TPC only tracks, constraint to the primary vertex using SPD)

An additional important ingredient for the determination of the event-plane angle are the so-called *weighting factors* for the determination of the event flow vector (see eq. 4.2); they are determined based on p_{T} and ϕ of each track. The total weight is defined as:

$$w_i = w_i(p_{\mathrm{T}i}) \cdot w_i(\phi_i) \tag{4.4}$$

The weight as function of p_{T} is defined as:

$$w_i(p_{\mathrm{T}}) \quad = p_{\mathrm{T}} \text{ for } p_{\mathrm{T}} < 2 \text{ GeV}/c \tag{4.5}$$

$$w_i(p_{\mathrm{T}}) \quad = 2 \text{ for } p_{\mathrm{T}} \geq 2 \text{ GeV}/c \tag{4.6}$$

The constant $w_i(p_{\mathrm{T}})$ for higher p_{T} avoids a bias from high-p_{T} particle production, e.g. a high momentum jet would bias the event-plane angle in the direction of the jet. Due to the non-uniform acceptance of the TPC in ϕ, the weight in azimuth is determined such, that a flat distribution of the event-plane angle is achieved which is expected from the statistical distribution of the Pb-Pb collision directions.

4.3. Quality Assurance

During and after the reconstruction, various checks are performed, after which a list of suitable runs is prepared for each data taking period. This quality assurance (usually abbreviated by *QA*) process is mainly done by detector experts for each detector separately, but additional quality assurance is done in the analyses as well. In the following, two examples of QA checks are presented. The first one is a result from the quality assurance procedure of the TPC and has been analyzed by the detector experts. The second one is done in this work and focuses on the QA of the event-plane angle distribution.

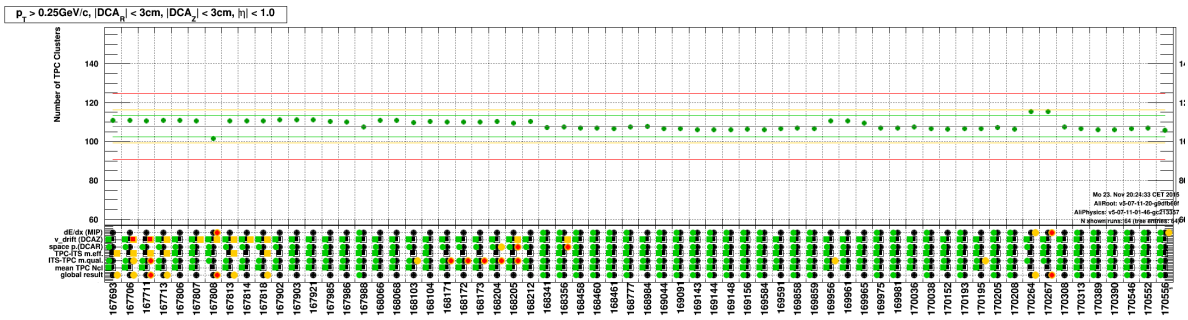

Figure 4.5.: Average number of clusters per track in the TPC as function of the run number for a selection of runs of the data taking period 2011. [37]

4.3.1. Average number of clusters per track in the TPC

The average number of clusters per track in the TPC is independent of the parameters of a Pb–Pb collision such as beam energy or centrality. It is therefore well suited to evaluate the run-wise performance of the TPC. Fig. 4.5 shows in the upper panel the average number of clusters per track in the TPC as obtained from the TPC QA as function of the run number for a selection of runs of the data taking period 2011. Tracks have been selected by basic cut settings, i.e. $p_{\mathrm{T}} > 0.25$ GeV/c, distance of closest approach to the primary vertex in r and z direction $|DCA_R| < 3$ cm and $|DCA_Z| < 3$ cm and $|\eta| < 1.0$. The distribution is nearly independent of the run number and stays within the limits proposed by the detector experts (shown as colored lines). The run 167808 has a lower average number of clusters per track, but is still inside the limits. This is a first hint, that the run might not be usable in the analysis. The lower panel of Fig. 4.5 shows additional QA variables, where the color code shows, if the measurement is within the suggested limits. These limits are either developed by the detector experts and base on the technical properties of the TPC or have been developed during the data taking periods.

4.3.2. Eventplane Recentering

A second quantity which has been part of the QA specific for this work is the determination of the event-plane and the effect of the recentering of the event-plane. During the reconstruction process, the event-plane angle is determined for each event. For some runs, this determination is not done properly, which results in an event-plane-angle distribution, which is not flat as expected. This is shown in Fig. 4.6: the large panel in the middle shows the event-plane-angle distribution for each run normalized to the

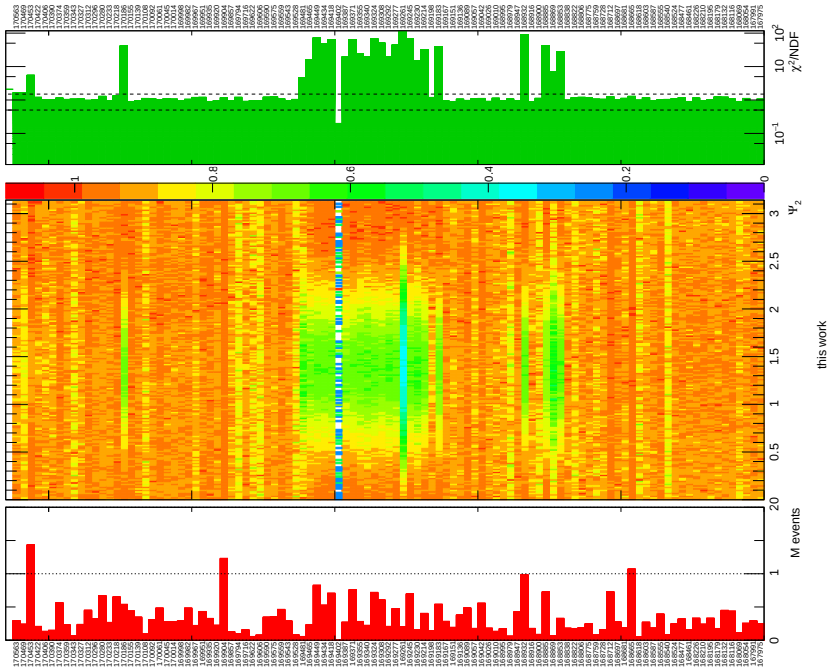

Figure 4.6.: χ^2 distribution (uppest panel), event-plane-angle distribution (middle panel) and number of events (lowest panel) as function of the run number (event flow vectors not recentered).

maximum number of events per event-plane angle bin of each distribution for a comparable color scale on the z-axis. It can be clearly seen, that a couple of runs have a dip for $\Psi_2 = 0$, which can be traced back to an untuned event-plane-angle determination. As a flat distribution is expected for the event-plane distribution, the event-plane distribution in Fig. 4.6 is parametrized by a constant function; the χ^2/NDF of each parametrization and the event-plane-angle distribution is shown in the upper panel of Fig. 4.6 as green bars. Most of the runs have a $\chi^2/NDF = 1$, which is in agreement with the expectation of a flat behaviour of the event-plane-angle. Those runs, which have a dip around $\Psi_2 = \pi/2$ show a strong deviation from $\chi^2/NDF = 1$. The lower panel of Fig. 4.6 shows the number of events per run as red bars.

Runs with a non-flat event-plane-angle distribution can either be excluded from the analysis, which reduces the statistics, or the event-plane angle can be recalibrated. In the event-plane framework in ALICE, the second possibility has been included [16], where the weights w_i of the event flow vector are retuned to flatten the event-plane-angle distribution. Fig. 4.7 shows this recentered event-plane-angle distribution.

The run 169584, which contains only few events after the event selection, is included in the analysis after a detailled check.

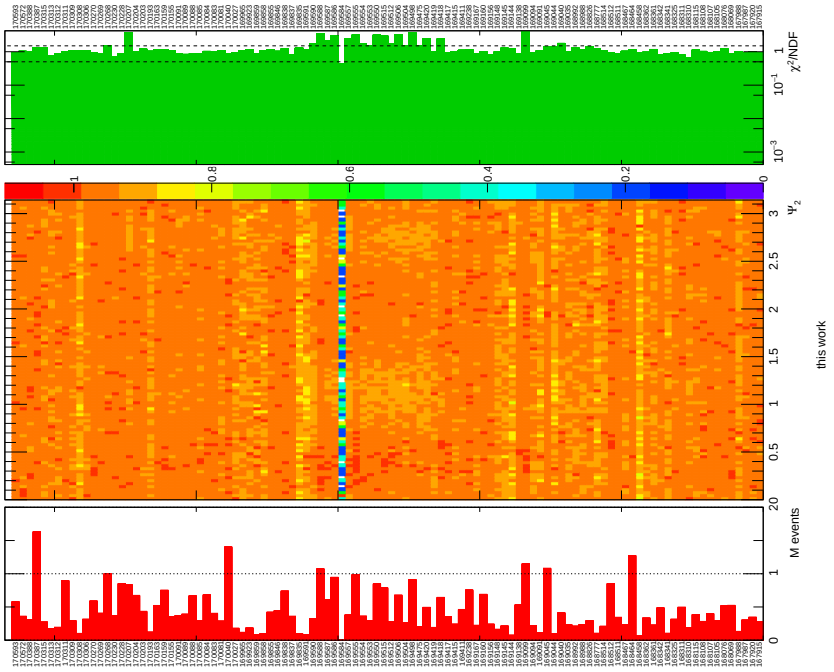

Figure 4.7.: χ^2 distribution (upper panel), event-plane-angle distribution (middle panel) and number of events (lower panel) as function of the run number after recentering of the event flow vectors.

4.4. Track Level Corrections

After the selection of the events, suitable measured tracks are selected for the analysis (with so-called *track cuts*) based on their properties in the detector. In this analysis, tracks of charged particles have been selected such, that the *quality* of the reconstructed transverse momentum is high, which means, that the parametrization of the measured detector hits (i.e. the track) has a small uncertainty. A first selection has been applied during the reconstruction and production of the AODs. A full list of the basic selection criteria is shown in table B.1, the adoption of the relevant criteria for this work are explained in this section. After the application of these track cuts, the resulting track sample is corrected for inefficiencies in the detector setup, the acceptance of the detector as well as the contamination from secondary particles which still remain in the data. The corrections are based on Monte Carlo information.

In this work, the efficiency and acceptance correction and secondary contamination correction have been treated separately; the procedures and the resulting corrections are presented after the explanation of the track selection. Table 4.2 shows the data

Period	Type	Comment
LHC10h	Data	taken in 2010, Pb–Pb collisions, $\sqrt{s_{NN}} = 2.76$ TeV
LHC11h	Data	taken in 2011, Pb–Pb collisions, $\sqrt{s_{NN}} = 2.76$ TeV
LHC11a10a_bis	MC	anchored to LHC10h, minimum bias
LHC14a1a	MC	anchored to LHC11h, for centrality 0 - 10 %
LHC14a1b	MC	anchored to LHC11h, for centrality 10 - 50 %
LHC14a1c	MC	anchored to LHC11h, for centrality 50 - 90 %

Table 4.2.: Data and MC productions of Pb–Pb collisions used in this work.

taking periods and corresponding MC productions for Pb–Pb collisions used in this work. Due to computing reasons, the MC production *LHC14a1* corresponding to the data taking period LHC11h has been split into three centrality parts by limiting the impact parameter distribution. In this production, neutral mesons (π^0 and η) have been included in the generation of each event to generate high statistics for calorimeter and photon conversion analyses; these so-called *injected signals* have been excluded for this work. The MC production *LHC11a10a_bis* corresponding to the data taking period LHC10h is a so-called *minimum bias production*, where all events are taken into account.

If a primary charged particle decays into a charged particle and a not-measured (e.g. neutral) particle, the decay topology has a *kink* at the secondary vertex. This kink results in two separate tracks being reconstructed. With the help of an algorithm to find these kinks, a so-called **kink daughter rejection** is applied, which rejects the secondary charged track in the decay. A basic track property is the **number of clusters per track in the TPC**, i.e. the number of measured hits in the TPC. A cut on the number of clusters has the disadvantage, that the distribution of the clusters on the track is not taken into account, e.g. a track with 35 clusters at the innermost radius of the TPC and 35 clusters at the outermost radius of the TPC has a better track fit than a track with 70 clusters at the innermost radius, but both tracks would be selected equally for an analysis. Therefore, a cut on another characteristic property of a track, the **number of crossed pad rows at the endcaps of the TPC**, $N_{crossedrows,TPC}$ is applied. This track property measures, how many read-out rows a track spans, independent of the positions of the measured clusters. Tracks are required to have $\boldsymbol{N_{crossedrows,TPC} > 100}$. Both cuts on the track characteristics (the cut on the number of clusters and the cut on the number of crossed rows) are enabled in this analysis.

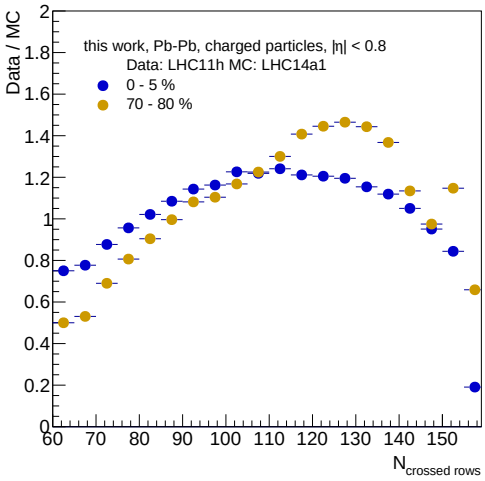

Figure 4.8.: Comparison of the ratio of the distribution of crossed rows in data and MC for central and peripheral events.

To determine Monte Carlo based corrections such as the efficiency of the analysis (as discussed in chapter 4.4.1), the distribution of each cut quantity should be similar in data an MC. Fig. 4.8 shows the ratio of the distribution of crossed rows in data and MC for central and peripheral events for the dataset LHC11h and the corresponding MC, LHC14a1. While for central events, the ratio deviates by $\approx 20\%$ from unity, the deviation from unity increases for peripheral events in this MC production. To improve the description of the track properties in MC, an additional cut was implemented by the detector experts and tested in this work. This new cut is purely geometrical and not affected by any detector description in the MC. The cut selects tracks based on their **active length in the TPC**, which measures the length of a track in the active volume of the TPC (in cm). A comparison of the distributions of the active length in the TPC between data and MC for central and peripheral events is shown in Fig. 4.9. The MC distribution has been reweighted such, that the underlying transverse momentum distribution agrees with the p_{T} distribution measured in data. The deviations between data and MC are $\approx 5 - 10\%$ and originate from the difference in the underlying distributions (e.g. η, ϕ). Tracks with an active length of less than 100 cm are rejected from the analysis by other cuts already at the stage of the filtering for the AODs. The track cuts on the active length in the TPC, the number of crossed rows and the number of clusters per track in the TPC are applied in addition to the track cuts shown in table B.1 of the filter bit *kTrkGlobal*.

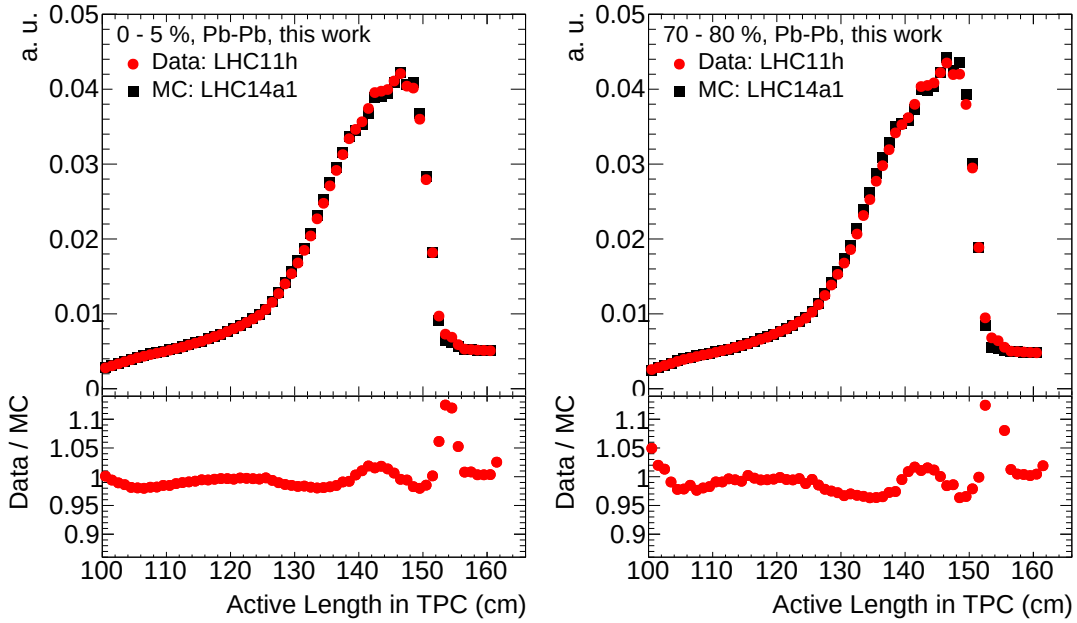

Figure 4.9.: Comparison of the ratio of the distribution of active length in the TPC in data and MC for central (left) and peripheral (right) events.

To determine a fully corrected spectrum, three different corrections are applied in this work. Firstly, the efficiency correction $c_{eff-acc}$ corrects for the efficiency and acceptance of the detector setup. Secondly, the contribution from secondary particles is corrected with the secondary contribution correction $c_{sec-cont}$. Thirdly, the transverse momentum resolution of the tracks at high p_{T} is corrected with the p_{T} resolution correction $c_{p_{\mathrm{T}}-res}$. All three corrections are applied to the raw particle yield to obtain the fully corrected invariant yield as function of p_{T}:

$$\frac{1}{N_{evt}}\frac{1}{2\pi}\frac{1}{p_{\mathrm{T}}}\frac{d^2N}{d\eta dp_{\mathrm{T}}} = c_{eff-acc}\left(p_{\mathrm{T}}\right)\cdot c_{sec-cont}\left(p_{\mathrm{T}}\right)\cdot c_{p_{\mathrm{T}}-res}\left(p_{\mathrm{T}}\right)\frac{1}{N_{evt}}\frac{1}{2\pi}\frac{1}{p_{\mathrm{T}}}\frac{d^2N_{raw}}{\Delta\eta\Delta p_{\mathrm{T}}} \quad (4.7)$$

4.4.1. Efficiency Correction

Every measurement with a detector is specific for this particular detector. The measured results need to be corrected for the detector properties. Here the measurement of charged tracks needs to be corrected for the *tracking and reconstruction efficiency* as well as for the acceptance. *Efficiency* here means, that tracks can be measured with a certain probability only. In some cases, the tracks are reconstructed with a different curvature than the curvature of the true particle trace and are therefore rejected by the tracking cuts. *Acceptance* names the fact, that ALICE covers only a part of the possible phase

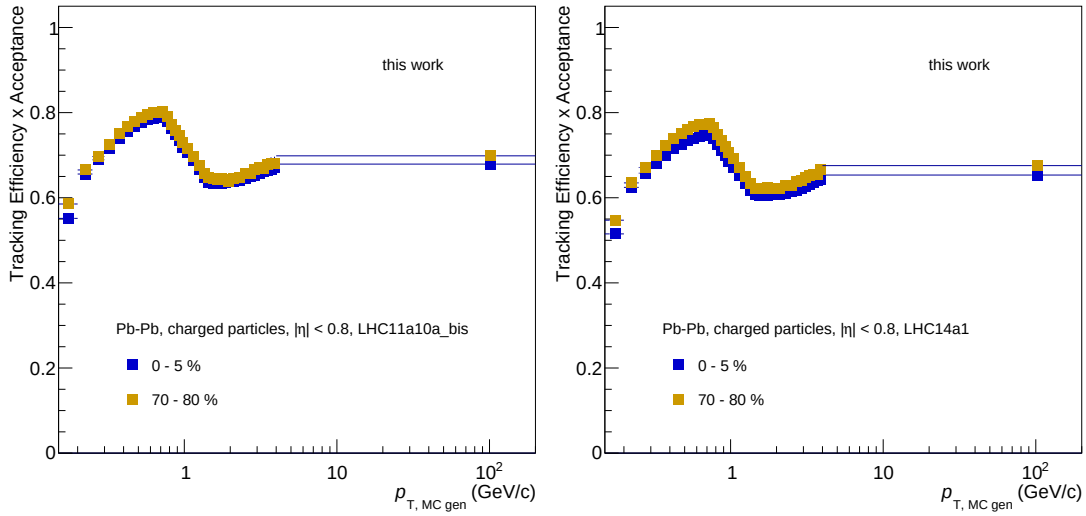

Figure 4.10.: Tracking efficiency times acceptance for charged particles with the cut settings discussed in the text for two different centrality selections (central and peripheral events) as function of p_{T} for the data taking periods 2010 (left) and 2011 (right).

space of the particles created in a collision.

To determine the efficiency of primary charged particles, collisions of heavy ions are simulated with Monte Carlo event generators. In this work, HIJING [30] is used as the event generator. The particles generated in these simulated collisions are then propagated through a simulated detector setup of ALICE, which is modeled with the GEANT [38] package. In ALICE, the generation of MC events as well as the propagation through a modeled detector is provided centrally to reduce the computing time needed on the GRID. Fig. 4.10 shows the product of tracking efficiency and acceptance [1] of primary charged particles as a function of the transverse momentum of the generated input particle. In this analysis the tracking efficiency is determined separately from the transverse momentum resolution. For the determination of the tracking efficiency the generated transverse momentum of each particle is used instead of the reconstructed p_{T} of the particle. A potential shift in p_{T} during the reconstruction is covered by the p_{T} resolution correction as discussed later in this section. The tracking efficiency is determined as

$$\epsilon \text{ x } A = \frac{\mathrm{d}N/\mathrm{d}p_{\mathrm{T}}|_{\text{after all cuts}}}{\mathrm{d}N/\mathrm{d}p_{\mathrm{T}}|_{\text{generated}}} \equiv c_{eff-acc} \tag{4.8}$$

Due to limited statistics at high p_{T}, the tracking efficiency is integrated above $p_{\mathrm{T}} = 4$ GeV/c to avoid statistical fluctuations in the correction procedure. The left panel of

[1] Unless otherwise stated, *tracking efficiency* is used as synonym for the product of tracking efficiency and acceptance in the following.

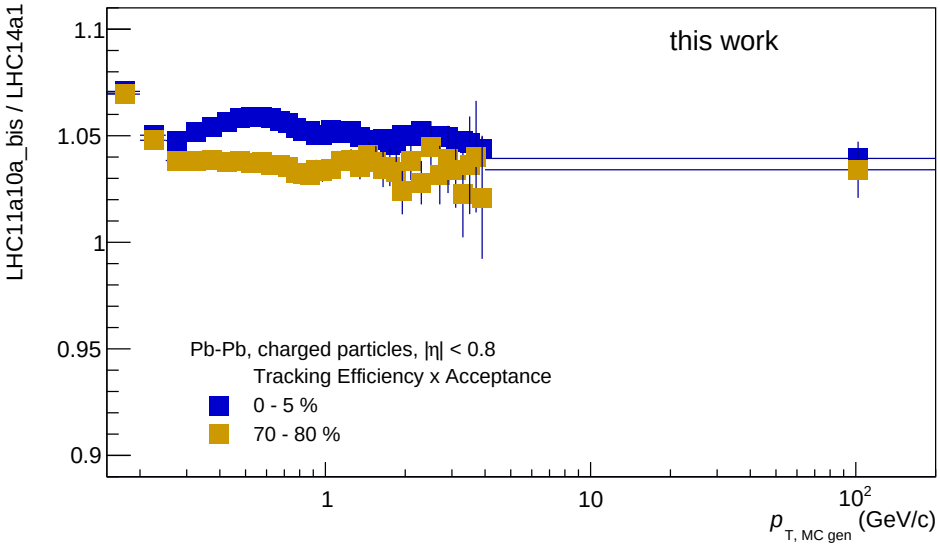

Figure 4.11.: Ratio of tracking efficiency x acceptance for charged particles for the data taking period 2010 and 2011 with the cut settings discussed in the text for central and peripheral events as function of p_{T}. The efficiency for the data taking period 2010 is slightly higher than for the data taking period 2011 (see text for details).

Fig. 4.10 shows the tracking efficiency for the data measured in 2010, which has been re-analyzed in this work based on AODs and a new analysis task; the right panel shows the tracking efficiency for the data measured in 2011 (see table 4.2 for the corresponding ALICE-internal abbreviations). The centrality-dependence of the tracking efficiency is small for both data-taking periods but cannot be neglected.
For the data-taking period in 2010, the efficiency is slightly higher, which can be attributed to a higher acceptance in the ITS (smaller number of dead pixels in the SPD). The increased number of dead pixels in the SPD in the data taking period 2011 is partially recovered by requiring hits in the SDD instead of hits in the SPD.
Fig. 4.11 shows the ratio of the tracking efficiencies between the data taking periods in 2010 and 2011 for central and peripheral events. The difference is stronger and has a stronger p_{T} dependence for central events in comparison to peripheral events, which can be attributed to the different acceptances in the ITS.

4.4.2. Secondary Contamination Correction

The reconstructed tracks which pass the track selection cuts contain not only primary charged particles, but, due to the statistical approach of the track cuts, also secondary particles from decays. All those particles need to be subtracted from the data sample.

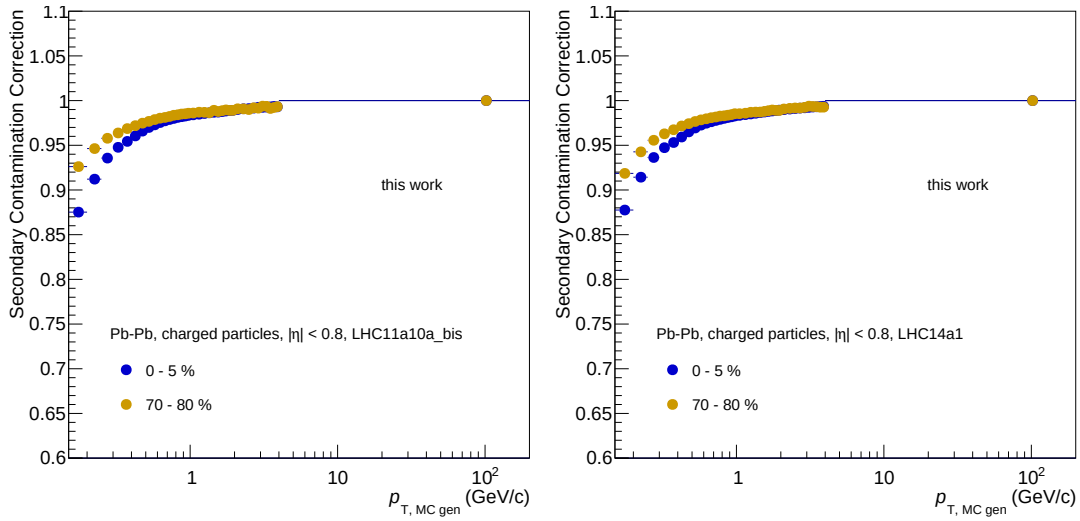

Figure 4.12.: Secondary contamination correction for charged particles with the cut settings discussed in the text for central and peripheral events as function of p_{T} for the data taking periods 2010 (left) and 2011 (right).

This subtraction is done via an evaluation of the secondary contamination based on MC generators. The resulting correction $c_{sec-cont}$ is shown in Fig. 4.12 for the data taking periods 2010 (left) and 2011 (right) for central and peripheral events.
Secondary particles are found mainly in the track sample at low transverse momenta, where the correction is highest. The correction decreases with increasing p_{T}, as the position resolution of a potential secondary vertex is higher for primary particles with higher transverse momenta. At high p_{T}, the secondary contamination correction has been rebinned to reduce statistical uncertainties from the MC sample.
The ratio between the secondary contamination corrections for the two data taking periods is shown in Fig. 4.13 for central and peripheral events. The slight difference at low p_{T} can be explained by the different acceptances in the ITS (smaller number of dead pixels in the data taking period in 2010).

4.4.3. p_{T} Resolution Correction

All tracks measured in the TPC have a finite momentum resolution, which results from the measurement of the clusters in the TPC. The measurement of the momentum resolution is based on information of the Kalman-Filter (see 3.3 for details of the tracking). The analysis of the p_{T} resolution is done in terms of $1/p_{\mathrm{T}}$ as the resolution behaves Gaussian around the measurement of the radius of each track in the TPC and the radius of the track is proportional to the inverse of the transverse momentum. It is assumed, that

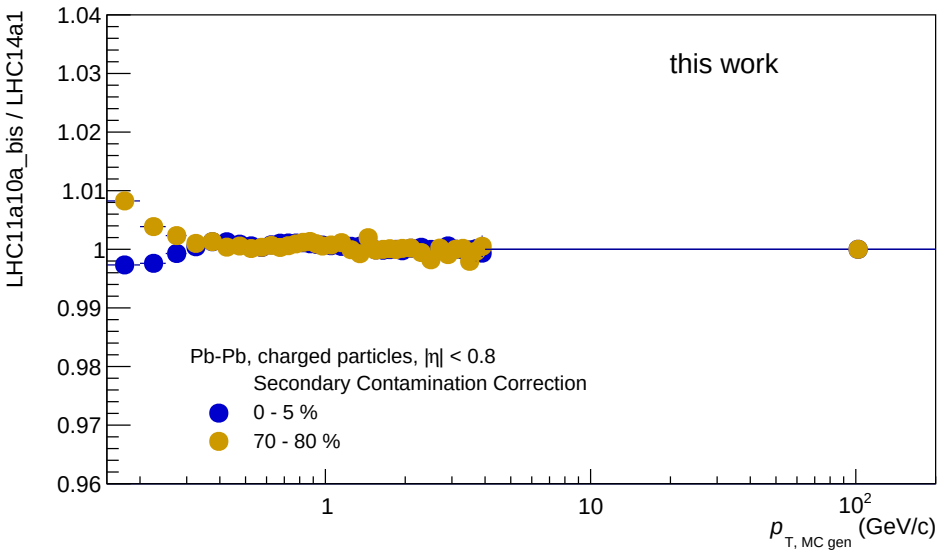

Figure 4.13.: Ratio of the secondary contamination corrections for charged particles with the cut settings discussed in the text for central and peripheral events as function of p_{T} for the MC corresponding to the data taking periods 2010 and 2011.

the relative resolution of the inverse of the transverse momentum equals the relative resolution of the transverse momentum:

$$\frac{\sigma\left(p_{\mathrm{T}}\right)}{p_{\mathrm{T}}} \approx \frac{\sigma\left(\frac{1}{p_{\mathrm{T}}}\right)}{\frac{1}{p_{\mathrm{T}}}} \tag{4.9}$$

The relative p_{T} resolution is determined as

$$\frac{\sigma\left(\frac{1}{p_{\mathrm{T}}}\right)}{\frac{1}{p_{\mathrm{T}}}} = \frac{\sqrt{Cov\left(\frac{1}{p_{\mathrm{T}}}, \frac{1}{p_{\mathrm{T}}}\right)}}{\frac{1}{p_{\mathrm{T}}}} \tag{4.10}$$

Here, Cov is the covariance matrix, which gives a measure of the width of the measurement of $\frac{1}{p_{\mathrm{T}}}$. The measured p_{T} resolution as a function of p_{T} is shown in Fig 4.14 for the data taking period LHC11h for nine centrality intervals. It has a minimum for $p_{\mathrm{T}} \approx 1.5$ GeV/c. In addition to the different centrality intervals, the centrality-averaged p_{T} resolution is shown as full red markers. The average shows, that the centrality dependence is small. For low p_{T}, the p_{T} resolution is dominated by multiple scatterings, which is a statistical process. The highest p_{T} resolution is reached for tracks with $p_{\mathrm{T}} \approx 1$ GeV/c. For higher p_{T} the momentum resolution gets worse, as the spatial resolution of the measured clusters decreases with increasing p_{T}.

The p_{T} resolution measured in the data taking period LHC11h can now be compared to

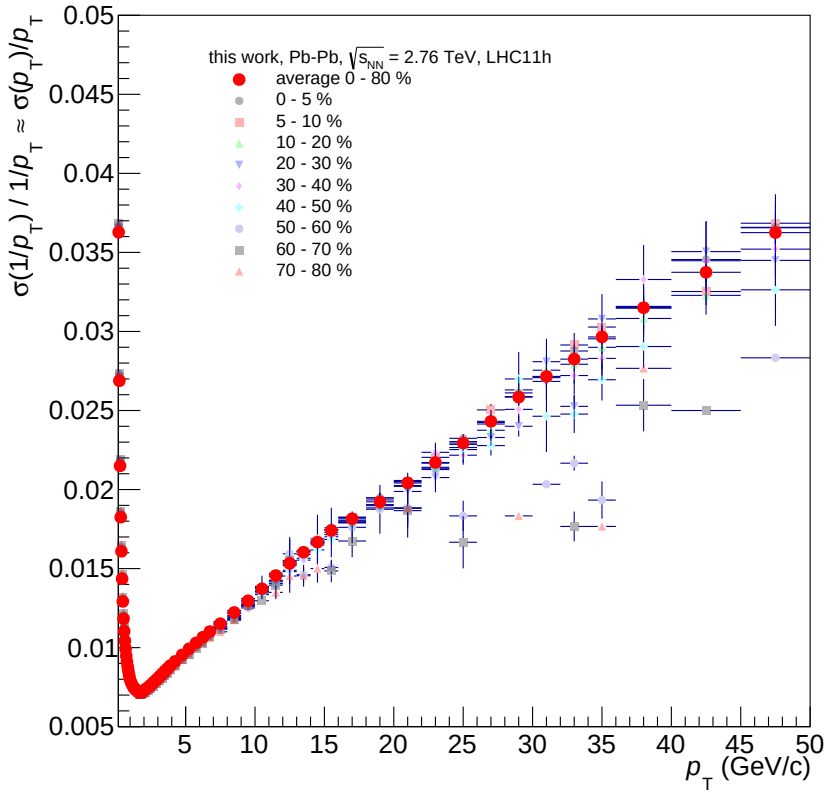

Figure 4.14.: Relative p_{T} resolution as function of p_{T} for the data taking period 2011 for nine different centrality intervals. Full red markers represent the p_{T} resolution averaged over these centrality intervals. Data points with a statistical uncertainty of $> 10\%$ are not shown in the plot but taken into account for the determination of the average.

the p_{T} resolutions measured in other data taking periods of LHC Run I; this comparison is shown in Fig. 4.15. The p_{T} resolutions measured for the data taking period 2011 and newer (represented as circles in Fig. 4.15) are smaller than the resolutions measured before. This is attributed to an update of the tracking algorithm (which is also used to determine the momentum resolution) after the pp reference run and before the second Pb–Pb beamtime. Tracks with high p_{T} need to be corrected for the p_{T} resolution, as the p_{T} resolution is affected by the reconstruction algorithm; low p_{T} tracks are not corrected for the p_{T} resolution. The correction of the p_{T} resolution is purely data-driven. To calculate this correction, an estimate of the approximate true, physical p_{T} distribution $dN/dp_{\mathrm{T}}^{approx.phys}$ is determined by removing the influence of the p_{T} resolution on the measured p_{T} distribution $dN/dp_{\mathrm{T}}^{measured}$. Here, the measured uncorrected transverse momentum distribution for each centrality interval is parametrized by a power-law function $f_{dN/dp_{\mathrm{T}}}$ for $p_{\mathrm{T}} > 5$ GeV/c to smoothen statistical fluctuations. This parametrization is unfolded by the measured

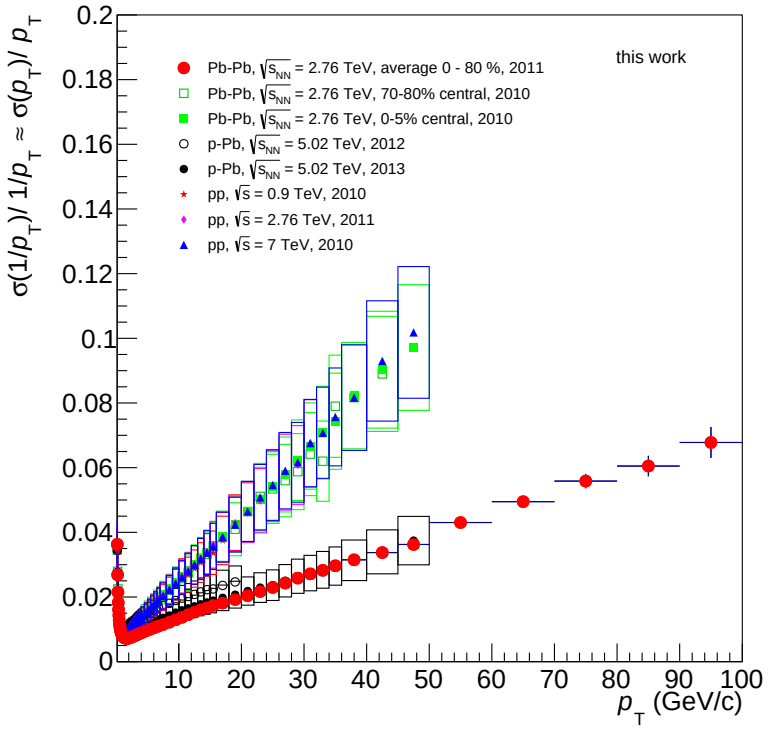

Figure 4.15.: Relative p_{T} resolution as function of p_{T} for the available datasets measured in ALICE in LHC-Run I.

p_{T} resolution to obtain a new parametrization $f^{unfolded}_{dN/dp_{\mathrm{T}}}$, which does not include the p_{T} resolution. The correction factor $c_{p_{\mathrm{T}}-res}$ is determined as:

$$c_{p_{\mathrm{T}}-res}\left(p_{\mathrm{T}}\right) = \frac{f^{unfolded}_{dN/dp_{\mathrm{T}}}}{f_{dN/dp_{\mathrm{T}}}} = \frac{dN/dp^{approx.phys}_{\mathrm{T}}}{dN/dp^{measured}_{\mathrm{T}}} \tag{4.11}$$

Fig. 4.16 shows the correction as function of p_{T} for central and peripheral events for the data set LHC11h. While the correction factor is small for peripheral events and has only a small p_{T} dependence, it shows a strong p_{T} dependence for central collisions resulting into a correction factor of $\approx 70\%$ for tracks at $p_{\mathrm{T}} = 100$ GeV/c. Although the centrality dependence of the measured p_{T} resolution is small, the underlying p_{T}-spectra differ strongly, which causes the difference in the p_{T} resolution correction.

Finally, all corrections are applied on the measured raw spectra in each centrality class, and the fully corrected spectrum is extracted.

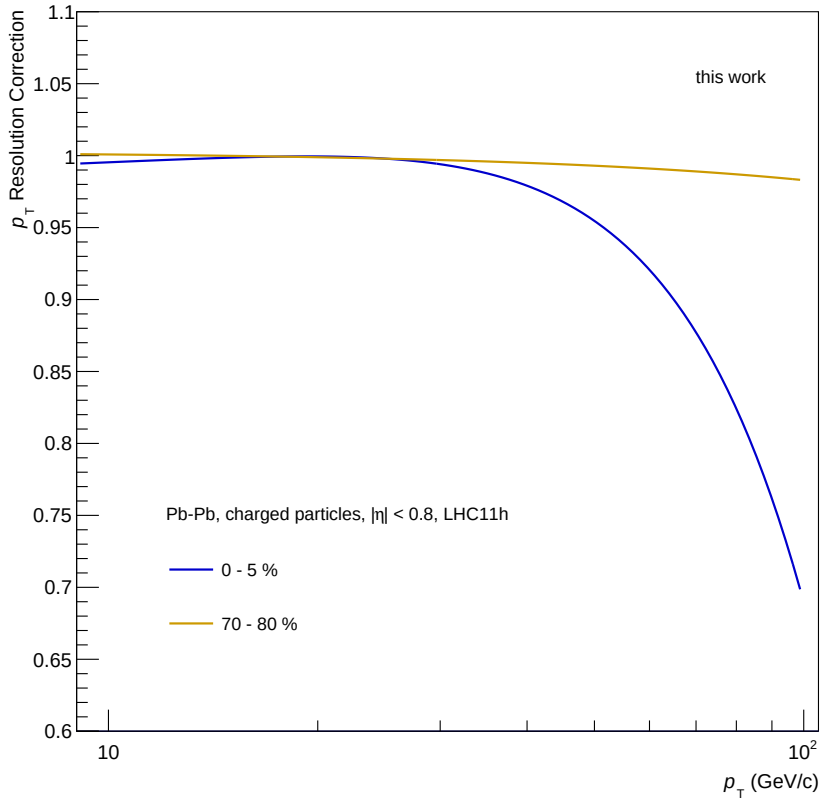

Figure 4.16.: p_{T} resolution correction as function of p_{T} for central and peripheral events obtained from measured data in the data taking period LHC11h (see text for details).

Chapter 5.

Charged Particle Spectra

The measurement of the p_{T} dependence of charged particle production in different collision systems can give insight into the particle production mechanisms in different momentum regimes as discussed in detail in sec. 2.2. For a better understanding of the results of the Pb–Pb data presented in this work, measurements in pp and p–Pb collisions function as valuable input. In preparation of the analysis of the Pb–Pb data, contributions to a joint effort to analyze pp and p–Pb data are part of this work as well [39]. Selected results from the final publications of these analyses [35, 40] relevant for the analysis of the Pb–Pb data are shown in the following chapter.
In the first section of this chapter, the p_{T} distributions in pp and Pb–Pb collisions, corrected for acceptance, efficiency, secondary contamination and p_{T} resolution as discussed in the previous chapter are presented. To complement the picture of particle production at high p_{T} which is discussed in depth in chapter 6, the second section in this chapter focuses on a characteristic derived property of the p_{T} spectrum for the low momentum part, the average transverse momentum $\langle p_{\mathrm{T}} \rangle$. Here, to better interpret the Pb–Pb data of this work, a comparison with results from pp and p–Pb collisions is presented.

5.1. Transverse momentum spectra

5.1.1. Measurement in pp collisions

The analyses of pp collisions have been performed similarly as of Pb–Pb collisions (see chapter 4). In addition, the pp measurements are normalized to the inelastic event

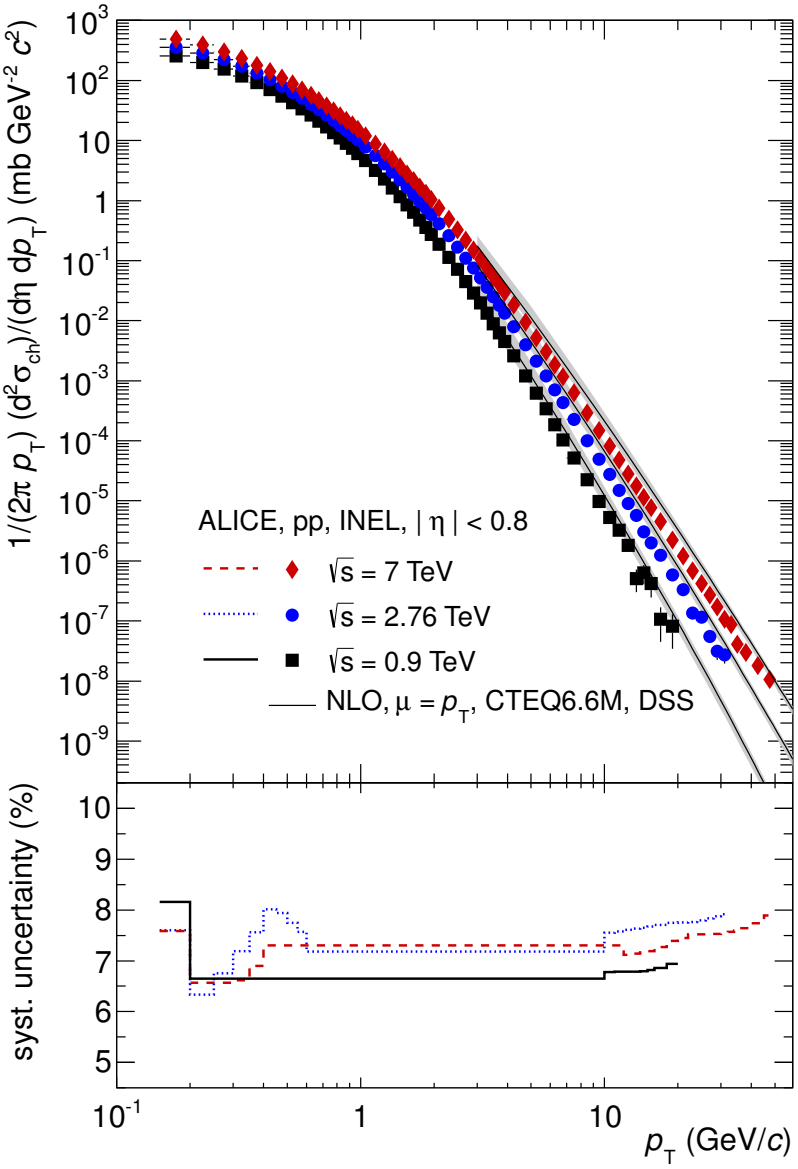

Figure 5.1.: Invariant yield of primary charged particles as function of p_{T} in pp collisions at $\sqrt{s} = 0.9, 2.76$ and 7 TeV (Fig. published in [35]).

cross-section σ_{inel} based on measurements in so-called *van-der-Meer-scans*:

$$\frac{1}{2\pi}\frac{1}{p_{\mathrm{T}}}\frac{d^2\sigma_{ch}}{d\eta dp_{\mathrm{T}}} = \sigma_{inel}\frac{1}{N_{evt}}\frac{1}{2\pi}\frac{1}{p_{\mathrm{T}}}\frac{d^2N_{ch}}{\Delta\eta\Delta p_{\mathrm{T}}} \tag{5.1}$$

Fig. 5.1 shows the invariant cross-section as function of p_{T} in pp collisions at $\sqrt{s} = 0.9, 2.76$ and 7 TeV as black, blue and red markers in the upper panel. The lower panel shows the total systematic uncertainties as function of p_{T} in the same colorcode for the three

different energies. In addition to the markers, the upper panel includes an NLO-pQCD calculation based on [1], an explanation of the underlying processes can be found in section 2.2.2. The cross-section obtained from the NLO-calculation [1] is a prediction based on previous measurements at lower energies, which are extrapolated to higher collision energies. The systematic uncertainty of the prediction shown in the plot as a gray band is determined by different renormalization scales μ_r and factorization scales μ_f, which are chosen as $\mu_r = \mu_f = p_{\mathrm{T}}, 2 \cdot p_{\mathrm{T}}, p_{\mathrm{T}}/2$ with $\mu_r = \mu_f = p_{\mathrm{T}}$ as central value. As one can see, the NLO-pQCD calculation overpredicts the measured data by a factor of two. A comparable effect has been observed elsewhere [41, 42]. This effect can be attributed to an incorrect particle composition in the model [2].
The result of the measurement at $\sqrt{s} = 2.76$ TeV is used in section 6.1 for the determination of a pp reference spectrum for the Pb–Pb results at the same energy. Furthermore, the results of all measurements as well as of the NLO-pQCD calculation are used in section 6.1.2 to determine a pp reference spectrum at $\sqrt{s} = 5.02$ TeV. As only the relative increase in cross-section is used for this determination for measurements and model separately, the overprediction of the model is of no concern for the later analyses.

x_{T} scaling

Historically, particle production at large p_{T} often has been compared in terms of a variable x_{T}. It is based on the assumption, that the particle production at high p_{T} does not depend on p_{T} itself but on the ratio between p_{T} and the collision energy, i.e. a definition of high p_{T} based on the available energy:

$$x_{\mathrm{T}} = \frac{2p_{\mathrm{T}}}{\sqrt{s}} \tag{5.2}$$

This definition results in the fact, that in the so-called x_{T}-scaling, a particle p_1 with $p_{\mathrm{T}} = 10$ GeV/c in a pp collision at $\sqrt{s} = 900$ GeV is comparable to a particle p_2 with $p_{\mathrm{T}} \approx 77$ GeV/c in a pp collision at $\sqrt{s} = 7$ TeV, or, in other words, p_1 results from a collision with a similar hardness as in a collision where p_2 is created. Generally, the cross-section of particle production at high p_{T} can be written as [43]:

$$E\frac{d^3\sigma}{dp^3} = \frac{1}{p_{\mathrm{T}}^{n_{eff}}} F\left(\frac{p_{\mathrm{T}}}{\sqrt{s}}\right) = \frac{1}{\sqrt{s}^{n_{eff}}} G(x_{\mathrm{T}})$$

F and G are functions, which scale with p_{T}^n or $\sqrt{s}^n$, respectively. For lowest-order pQCD calculations, the effective power-law parameter n_{eff} equals to 4.0. As higher order effects

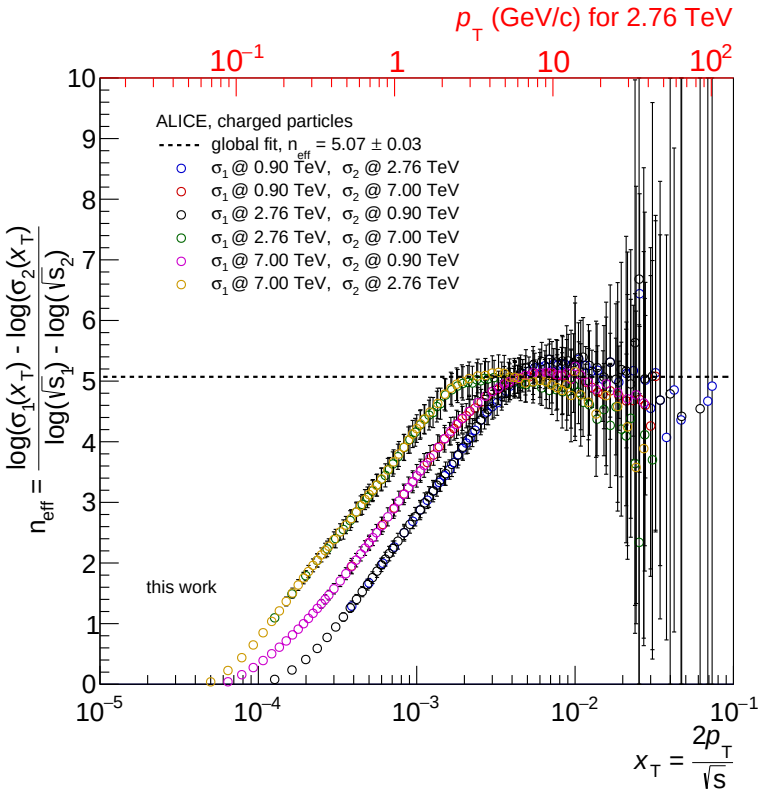

Figure 5.2.: Derivation of the effective power-law exponent n_{eff} based on measured data (see text for details). The dashed line represents a global fit to the data, which results in $n_{eff} = 5.07 \pm 0.03$.

such as running coupling as well as the evolution of the structure and fragmentation functions with momentum transfer play a role, the measured value of n_{eff} depends on x_{T} and $\sqrt{s}$ and can be determined from two different measurements of the invariant cross-section σ_1,σ_2 at the corresponding energies of $\sqrt{s_1}$ and $\sqrt{s_2}$:

$$n_{eff} = \frac{log(\sigma_1(x_{\mathrm{T}})) - log(\sigma_2(x_{\mathrm{T}}))}{log(\sqrt{s_1}) - log(\sqrt{s_2})}$$

Fig. 5.2 shows n_{eff} as function of x_{T} for combinations of selected data from pp collisions with ALICE. For guidance, the red axis on the top of the plot shows x_{T} translated to p_{T} for $\sqrt{s} = 2.76$ TeV. Error bars show the statistic uncertainties of the nominator only. A clear saturation of n_{eff} is visible, which is reached for $10^{-3} \lesssim x_{\mathrm{T}} \lesssim 10^{-2}$. The extraction of n_{eff} is performed with a global linear fit to the data for

$$\frac{5 \text{ GeV} \cdot 2}{2760 \text{ GeV}} < x_{\mathrm{T}} < \frac{35 \text{ GeV} \cdot 2}{2760 \text{ GeV}}$$

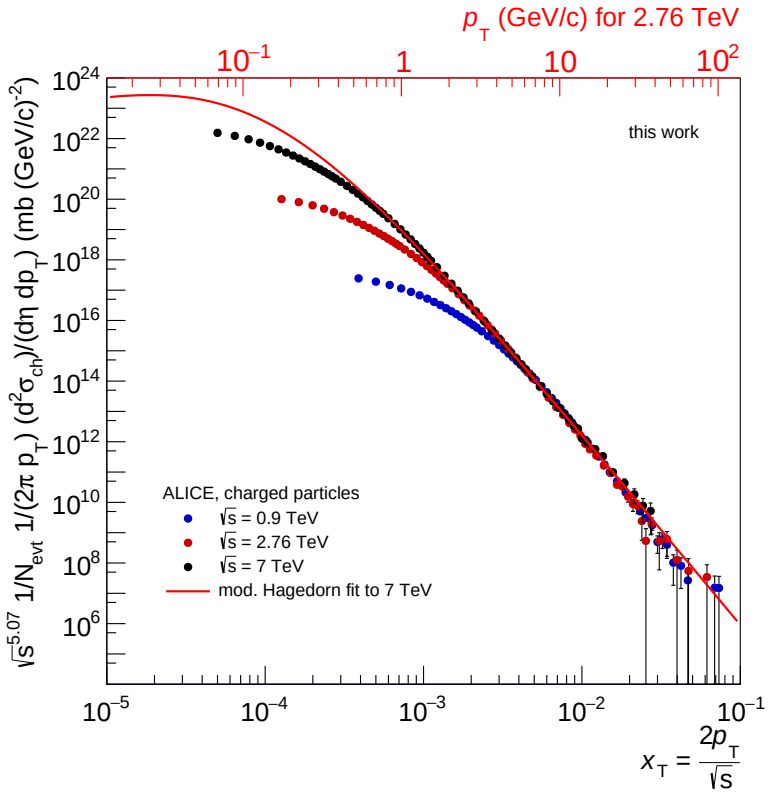

Figure 5.3.: Scaled invariant cross-section as function of x_{T} (lower axis) or p_{T} (upper axis) for charged particles measured in pp collisions with ALICE. The markers represent the measurement, while the line shows a parametrization of the high-p_{T} part of the measurement at $\sqrt{s} = 7$ TeV with a modified Hagedorn function.

and leads to

$$n_{eff} = 5.07 \pm 0.03$$

With this n_{eff} the measured invariant cross-sections at $\sqrt{s} = 0.9, 2.76$ and 7 TeV are scaled, which is shown in Fig. 5.3 together with a parametrization of the high-x_{T} part of the 7 TeV data. As expected, the scaled measured cross-sections are in agreement at high relative momenta, what is called x_{T}-scaling.
In summary, a wealth of data in pp collisions at different energies has been measured and can be used for comparison with the Pb–Pb data. The main focus of this work is however on the p_{T} spectra in Pb–Pb collisions, which are discussed next.

5.1.2. Measurement in Pb–Pb collisions

As discussed in chapter 4 in detail, various corrections are applied to the raw, i.e. uncorrected p_{T} distribution of charged particles as obtained from the application of the track finding algorythms. This procedure is performed similarly for all centralities and such the so-called invariant yield is extracted:

$$\frac{1}{N_{evt}}\frac{1}{2\pi}\frac{1}{p_{\mathrm{T}}}\frac{d^2N}{d\eta dp_{\mathrm{T}}} = \frac{1}{N_{evt}}\frac{1}{2\pi}\frac{1}{p_{\mathrm{T}}}\frac{d^2N_{corr}}{\Delta\eta\Delta p_{\mathrm{T}}} \tag{5.3}$$

Re-Analysis of LHC10h Minimum Bias Data

A re-analysis of the minimum bias data set LHC10h (see table 4.2 for a list of data-taking periods) has been performed in this work. Fig. 5.4 shows the invariant yield as function of p_{T} for primary charged particles measured in Pb–Pb collisions at $\sqrt{s_{NN}} = 2.76$ TeV for nine different centrality intervals. The results of the re-analysis are in agreement with the previously published [3] p_{T} spectra. The comparison between the re-analysis and the previously published results for the most central 0-5% collisions is shown in Fig. 5.5. A complete set of comparison plots for all centrality classes can be found in appendix A. The upper panels of the plots show the invariant yield as function of p_{T} for both analyses. The lower panels show the ratio of both spectra as markers, the gray band represents the systematic uncertainties of the published results. The results of both analyses agree within $< 5\%$ for all centrality intervals. This comparison shows, the results of the newly developed analyis task in this work are in agreement with the results of the previously used analysis procedure [39]. Based on this confirmation, the new analysis task will be used for the analysis of LHC11h data as discussed in the following section.

The dashed lines in Fig. 5.4 represent a pp reference spectrum based on an extrapolation of the measured data at $\sqrt{s} = 2.76$ TeV shown in Fig. 5.1. The extrapolation is discussed in detail in section 6.1. The reference is scaled by the number of collisions for each centrality class. The yields in Fig. 5.4 have been scaled with multiples of 10 for visualization. A clear centrality dependence of the shape of the p_{T} distribution can be observed. For peripheral collisions, the yield in Pb–Pb collisions is in reasonable agreement with the scaled pp reference, while for central collisions, the Pb–Pb spectrum is significantly suppressed compared to the scaled pp reference. At high p_{T}, this is commonly attributed to a suppression of the particle production due to energy loss in the QGP 2.3.3. At low p_{T}, the assumption of a scaling of the particle production with

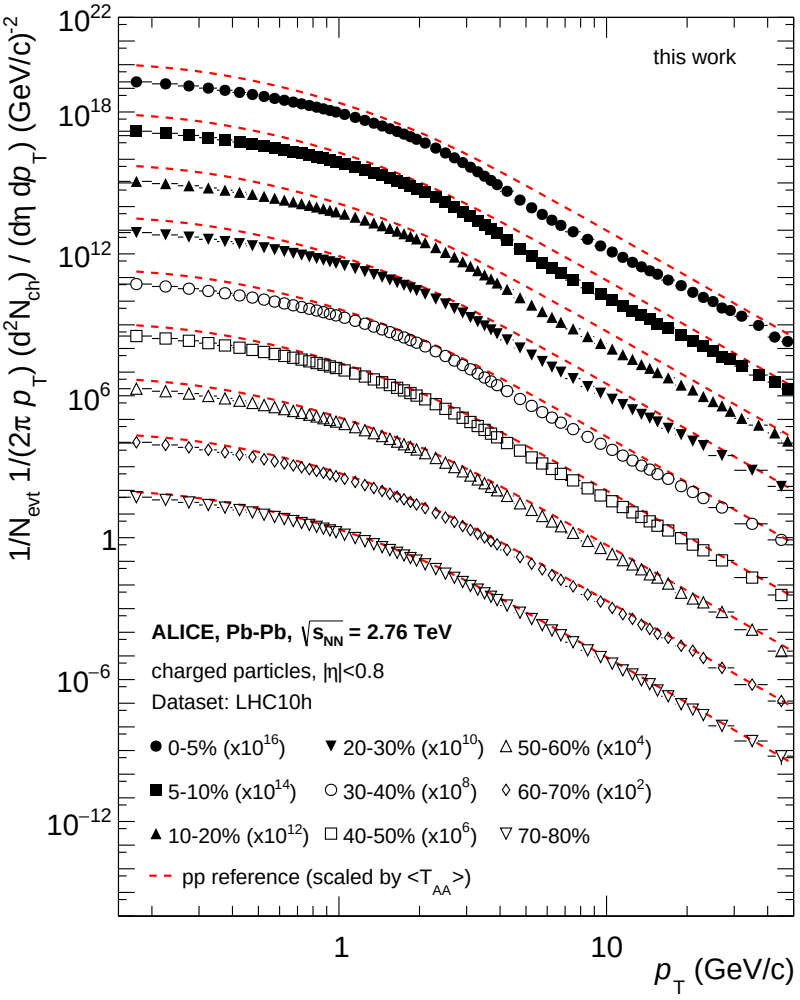

Figure 5.4.: Invariant yield of primary charged particles as function of p_{T} for nine different centrality intervals measured in Pb–Pb collisions at $\sqrt{s_{NN}} = 2.76$ TeV for the data-taking period LHC10h. The measured yields are compared to the T_{AA}-scaled proton-proton reference (see text for details).

the number of binary collisions fails. A detailed evaluation of the high-p_{T} effect will be discussed in chapter 6.

Extension of p_{T} reach in LHC11h Data

In the data-taking period LHC11h, not only minimum-bias triggers have been used. In addition, centrality triggers selected events with semi-central and central collisions. These triggers lead to the distribution of the number of events that is shown in Fig. 5.6. In this work, the central trigger (kCentral) is used for the 10% most central events, the semi-central trigger (kSemiCentral) for the 0 - 50% central events and the minimum-bias

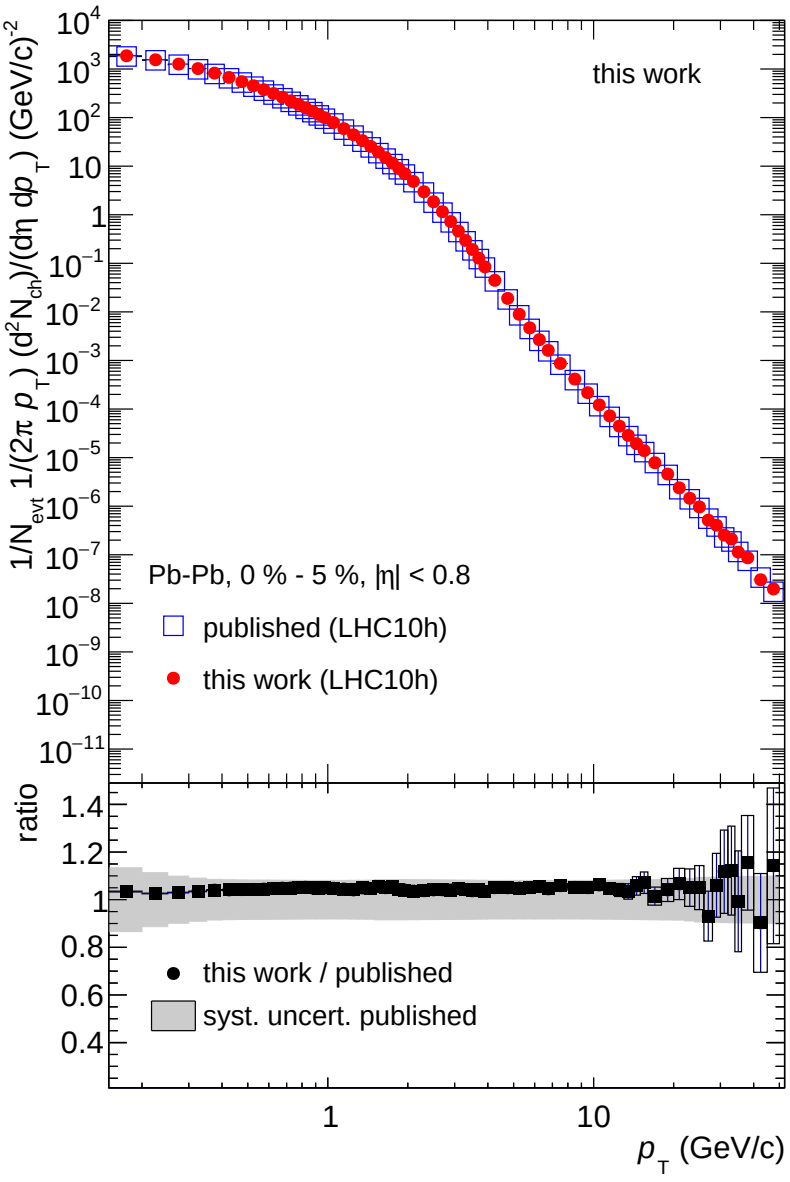

Figure 5.5.: Comparison of the re-analysis of the data set LHC10h to [3].

trigger (kMB) for the full range up to 80% centrality to increase the number of central and semi-central events in the data sample. As a consequence, the p_{T} reach of the spectra in these centrality classes is increased. The lowest centrality of the collision that is used for the determination of the centrality classes is set to 90%. This so-called anchor point defines up to which centrality of the collision, i.e. how peripheral, the VZERO multiplicity distribution (Fig. 4.4) is parametrized with a function to determine N_{coll} (compare section 4.2.2 for a description of the centrality determination). For the analysis in this work, the centrality has been limited to 0 - 80% to avoid contributions from

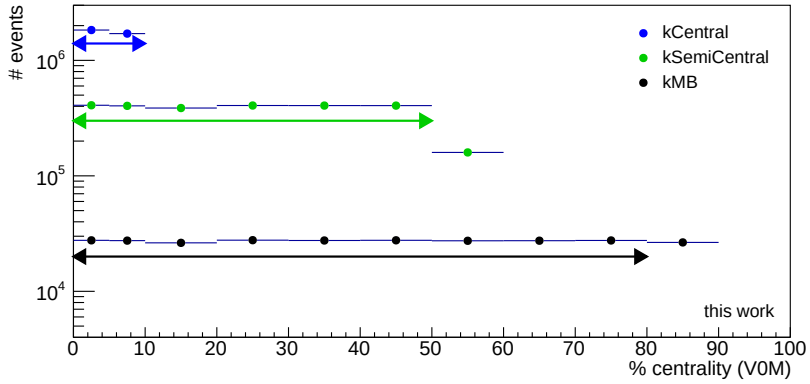

Figure 5.6.: Distribution of the number of events as function of the centrality estimated with the multiplicity in the V0 for the three different trigger settings in LHC11h. The arrows show the used range in the analysis.

edge effects in the parametrization. The analysis has been performed separately for the three trigger selections including a comparison of the raw uncorrected spectra of different trigger selections for each centrality interval. No difference in normalization has been found between the analysis of the centrality-triggered data sample and the minimum bias data sample (not shown).

To demonstrate the improvement by use of the new data sample LHC11h, Fig. 5.7 shows the statistical error of the raw p_{T} spectra as function of p_{T} measured in LHC10h (dashed lines) and LHC11h (solid lines). Here, data from the different trigger selections have been accumulated as discussed. For the centrality intervals where the central and semi-central triggers are fully efficient (0-10% and 0-50%, respectively), the statistical error is up to a factor 2 smaller at the same p_{T} in LHC11h compared to LHC10h; furthermore, here the enabling of a centrality trigger results in a higher p_{T}-reach. For peripheral events, where only the minimum-bias trigger is used in this analysis in LHC11h, the statistical error is much higher than in LHC10h, where more minimum bias triggers have been measured; this goes in line with a smaller p_{T}-reach for LHC11h. Bins with single counts have been excluded from the analysis.

The fully corrected spectra are shown in Fig. 5.8 as function of p_{T} for nine centrality intervals. Again, the dashed red lines represent the scaled pp reference spectrum. In addition, each pair of Pb–Pb and pp spectra has been scaled for visualization. As result of the increased statistics of semi-central and central collisions, the p_{T}-reach of the invariant yield for these collisions is increased. The suppression of the Pb–Pb spectra in comparison to the scaled pp reference that was observed in the LHC10h data (Fig. 6.6) can be confirmed. In addition, the new data extends the measurement to much higher p_{T} and is now reaching $p_{\mathrm{T}} = 100$ GeV/c for central and semi-central collisions. With this

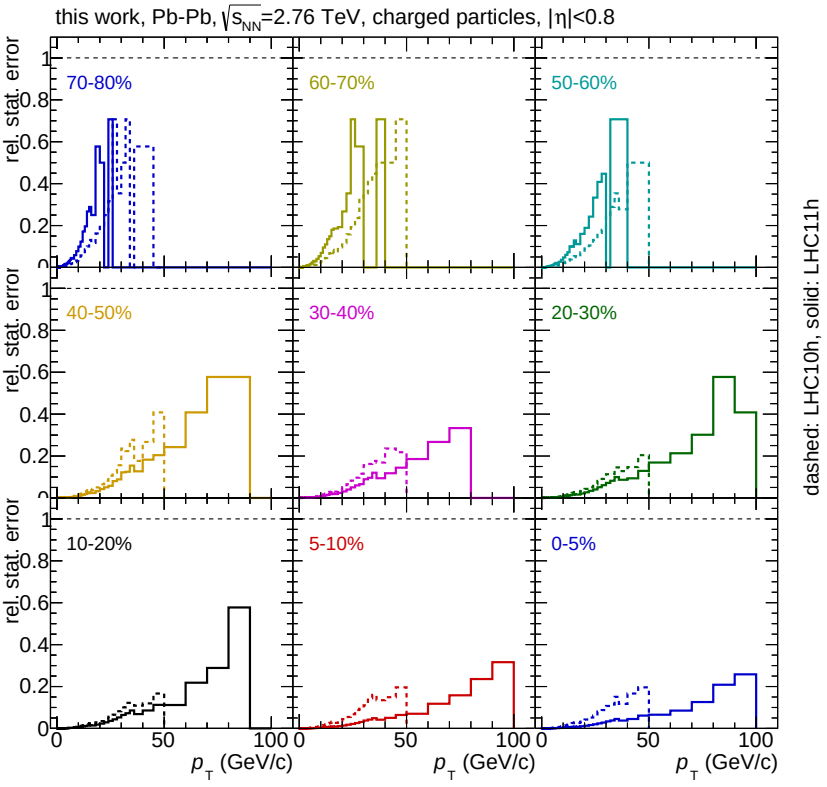

Figure 5.7.: Relative statistical error of the raw p_{T} spectra as function of p_{T} for nine different centrality intervals. Dashed lines represent the error in LHC10h, solid lines show the statistical error for LHC11h.

measurement, the energy loss mechanisms at higher p_{T} now can be constraint with a smaller uncertainty, which will help to improve the theoretical understanding of particle production in this energy regime. Again, more detailed discussion of these effects will be given in chapter 6.

The systematic uncertainties of the Pb–Pb spectra have been evaluated based on a variation of the track cuts. The main contribution to the systematic uncertainties arises from a variation of $N_{crossedrows,TPC}$, which is chosen as $N_{crossedrows,TPC} = 70, 100$ and 120 in the analysis. The total systematic uncertainty has been evaluated bin-by-bin as the quadratic sum of all individual contributions.

5.2. $\langle p_{\mathrm{T}} \rangle$ as function of multiplicity

As discussed, to complement the picture of particle production at high p_{T} this section now discusses the results of a characteristic derived property of the p_{T} spectrum for the

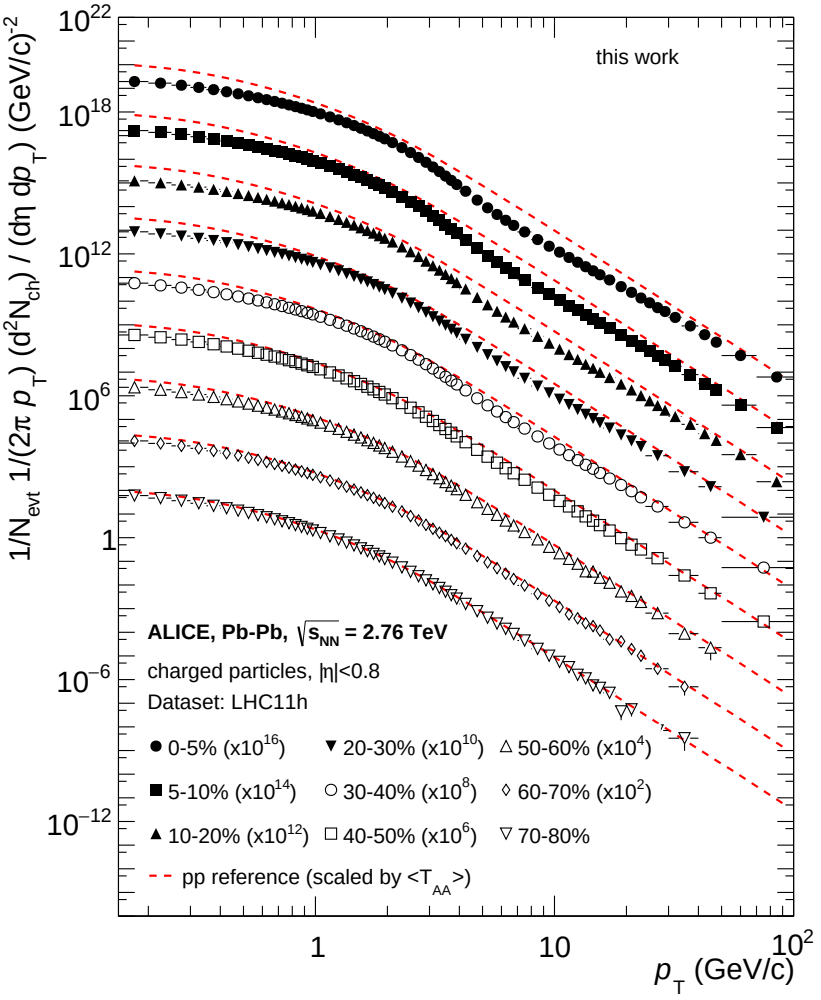

Figure 5.8.: Invariant yield of primary charged particles as function of the transverse momentum for nine different centrality intervals measured in Pb–Pb collisions at $\sqrt{s_{NN}} = 2.76$ TeV for the data-taking period LHC11h including centrality triggers (see Fig. 5.6). The measured yields are compared to the T_{AA}-scaled proton-proton reference (see text for details).

low momentum part, the average transverse momentum $\langle p_{\mathrm{T}} \rangle$. To better understand the results of Pb–Pb collisions, a short summary of the basic effects in pp and p–Pb collisions is given in the following. As previously discussed, the results are part of a joint effort to analyze the data and such are part of this work as well [39].

In general, distributions of a variable x are often characterized by the moments of the distribution. This chapter focuses on the first moment of the transverse momentum spectra of charged particles, i. e. the average transverse momentum $\langle p_{\mathrm{T}} \rangle$ and its dependence on the charged-particle multiplicity. This dependence between $\langle p_{\mathrm{T}} \rangle$ and the charged-particle multiplicity carries information about the underlying particle production

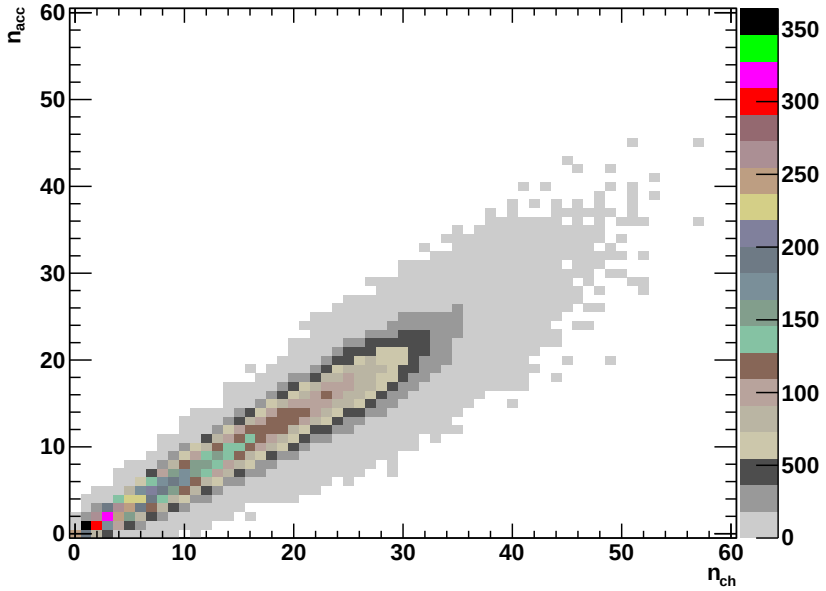

Figure 5.9.: PYTHIA generated correlation matrix $R\,(n_{ch}, n_{acc})$ for pp collisions at $\sqrt{s}$ = 0.9 TeV [44].

mechanisms and provides important input to model calculations.
For a general function $f(p_{\mathrm{T}})$, $\langle p_{\mathrm{T}} \rangle$ is defined as

$$\langle p_{\mathrm{T}} \rangle = \frac{\int p_{\mathrm{T}} \cdot f(p_{\mathrm{T}}) \mathrm{d}p_{\mathrm{T}}}{\int f(p_{\mathrm{T}}) \mathrm{d}p_{\mathrm{T}}} \tag{5.4}$$

In case this function is not continuous, but discretized in bins of p_{T}, e.g. a measured p_{T}-spectrum, this leads to

$$\langle p_{\mathrm{T}} \rangle = \frac{\sum_{i=0}^{N} y_i \cdot p_{\mathrm{T},i} \cdot w_i}{\sum_{i=0}^{N} y_i \cdot w_i} \tag{5.5}$$

where y_i is the yield at $p_{\mathrm{T},i}$ and w_i is the width of the corresponding bin.
To account for detector effects on the multiplicity, e.g. the influence of the acceptance, a correction algorithm has been developed in [44], where a detailed discussion of this correction algorithm can be found. Here only the key characteristics are outlined: The procedure is based on a correlation matrix $R\,(n_{ch}, n_{acc})$ obtained in MC simulations (see Fig. 5.9). This correlation matrix describes at which measured multiplicity n_{acc} an event with a generated (i.e. true) multiplicity n_{ch} on average is reconstructed. In a first approach, the *weighting procedure*, the measured $\langle p_{\mathrm{T}} \rangle\,(n_{acc})$ as function of the measured multiplicity n_{acc} is weighted with the correlation matrix R to determine $\langle p_{\mathrm{T}} \rangle\,(n_{ch})$ at the

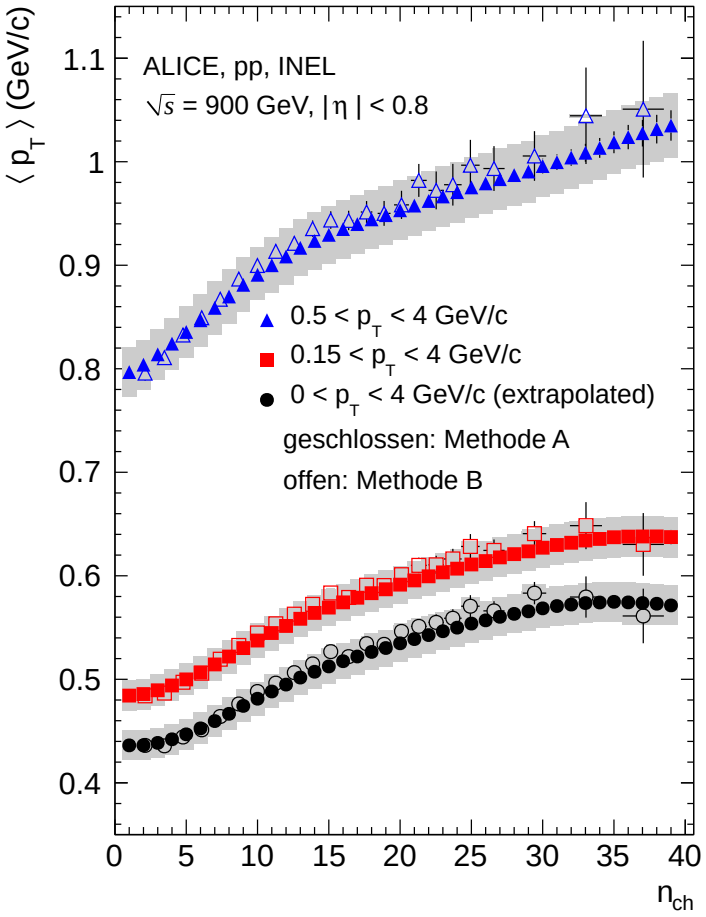

Figure 5.10.: Average transverse momentum $\langle p_{\mathrm{T}} \rangle$ in the range of $0.15 < p_{\mathrm{T}} < 4.0$ GeV/c as a function of the charged-particle multiplicity for inclusive charged particles in pp collisions at $\sqrt{s} = 0.9$ TeV. Open symbols represent the assignment procedure, closed symbols show the weighting procedure. The gray band shows the systematic uncertainty for the results of the weighting procedure. (Fig. published in [44]).

efficiency-corrected multiplicity n_{ch}:

$$\langle p_{\mathrm{T}} \rangle (n_{ch}) = \sum_{n_{acc}} \langle p_{\mathrm{T}} \rangle (n_{acc}) \cdot R(n_{ch}, n_{acc}) \tag{5.6}$$

Here, the normalized correlation matrix is used:

$$\sum_{n_{acc}} R(n_{ch}, n_{acc}) = 1 \tag{5.7}$$

In a second, different correction approach, the *assignment procedure*, the most probable corrected n_{ch}, i.e. n_{ch}^{mp}, is assigned to each n_{acc}. Here, the correlation matrix $R(n_{ch}, n_{acc})$

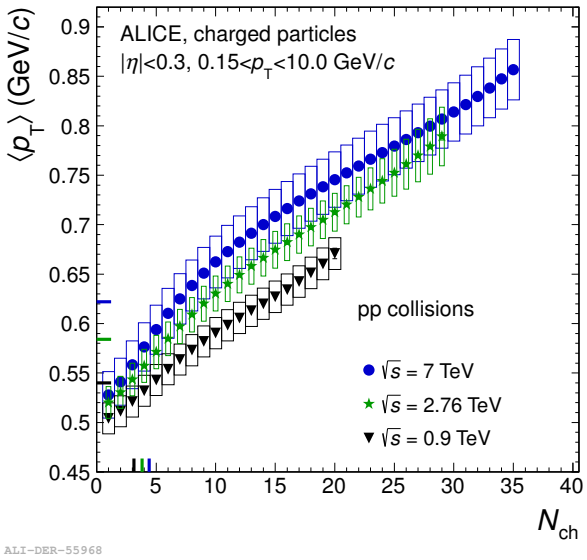

Figure 5.11.: Average transverse momentum $\langle p_{\mathrm{T}} \rangle$ in the range of $0.15 < p_{\mathrm{T}} < 10.0$ GeV/c as a function of the charged-particle multiplicity for inclusive charged particles in pp collisions at $\sqrt{s} = 0.9$, 2.76 and 7 TeV. The boxes represent the systematic uncertainties, statistical errors are of negligible size. The colored lines at the axes represent the inclusive $\langle p_{\mathrm{T}} \rangle$ and $\langle n_{ch} \rangle$ values. [40]

has been unfolded such, that the projection on the n_{acc}-axis agrees with the measured n_{acc} distribution. The mean of each n_{ch} distribution obtained from a projection of this unfolded matrix $R^{unfold}(n_{ch}, n_{acc})$ on the n_{ch}-axis for a given range in n_{acc} is then assigned as n_{ch}^{mp}. Fig. 5.10 shows a comparison of both methods for pp collisions at $\sqrt{s} = 0.9$ TeV for three different p_{T}-ranges. Open symbols represent the assignment procedure, closed symbols show the results of the weighting procedure. Both methods are in good agreement. In the following, only results for the weighting procedure are shown.

Fig. 5.11 shows the measured and corrected $\langle p_{\mathrm{T}} \rangle$ as function of n_{ch} for three pp collision energies, $\sqrt{s} = 0.9$, 2.76 and 7 TeV. The measurement extends to values, where the statistical error of the underlying n_{acc}-distribution is below 5%. Only tracks within a pseudorapidity interval of $|\eta| < 0.3$ are taken into account to have maximum overlap with measurements in p–Pb collisions, where the moving center-of-mass frame results in asymmetric collision geometries. For $|\eta| < 0.3$, the pseudorapidity distributions are flat for all collision systems (pp, p–Pb and Pb–Pb).

Tracks with $p_{\mathrm{T}} < 0.15$ GeV/c have a tracking efficiency $\epsilon_{tracking} < 50\%$ and are therefore rejected from the analysis. The upper range of $p_{\mathrm{T}} = 10$ GeV/c is chosen such, that all bins in n_{acc} have a comparable p_{T} reach.

An increase of $\langle p_{\mathrm{T}} \rangle$ with n_{ch} is observed. The increase with beam energy for a given

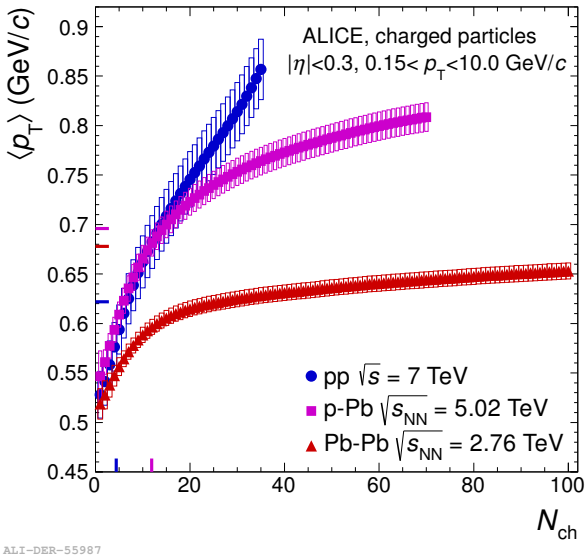

Figure 5.12.: Average transverse momentum $\langle p_{\mathrm{T}} \rangle$ in the range of $0.15 < p_{\mathrm{T}} < 10.0$ GeV/c as a function of charged-particle multiplicity for inclusive charged particles in pp, p–Pb and Pb–Pb collisions. The boxes represent the systematic uncertainties, statistical errors are of negligible size. The colored lines at the axes represent the inclusive $\langle p_{\mathrm{T}} \rangle$ and $\langle n_{ch} \rangle$ values. [40]

n_{ch} is small for low multiplicities and gets larger with increasing n_{ch}. Nevertheless, the difference between the measurements at $\sqrt{s} = 2.76$ TeV and $\sqrt{s} = 7$ TeV is small and both measurements agree within the systematic uncertainties. The main contribution of the systematic uncertainties originates from the uncertainty of the weighting procedure and has been estimated in a MC closure test. For this test, results obtained with Pythia6, Tune Perugia0 have been weighted with the correlation matrix R based on information from PHOJET and vice versa. The weighted $\langle p_{\mathrm{T}} \rangle$ as function of n_{ch} is compared to the input distribution of $\langle p_{\mathrm{T}} \rangle$ as function of n_{ch} to estimate the systematic uncertainty. This estimated uncertainty is n_{ch}-independent and amounts to $\approx 3\%$.

Fig. 5.12 shows $\langle p_{\mathrm{T}} \rangle$ as function of n_{ch} in pp collisions at $\sqrt{s} = 7$ TeV, p–Pb collisions at $\sqrt{s_{NN}} = 5.02$ TeV and Pb–Pb collisions at $\sqrt{s_{NN}} = 2.76$ TeV collisions in the same kinematic region as in Fig. 5.11. Based on the results measured in pp collisions shown in Fig. 5.11, the difference in center-of-mass energy can be neglected. For pp collisions, the results at $\sqrt{s} = 7$ TeV are used for comparison, as they extend to higher values of n_{ch} compared to the data at $\sqrt{s} = 2.76$ TeV in this dataset, both due to kinematic reasons (more phase space in collisions at $\sqrt{s} = 7$ TeV than in collisions at $\sqrt{s} = 2.76$ TeV) as well as higher statistics measured at $\sqrt{s} = 7$ TeV.

The mean transverse momentum as function of n_{ch} measured in p–Pb collisions is similar to the one measured in pp collisions up to $n_{ch} \approx 14$. The differences between pp and

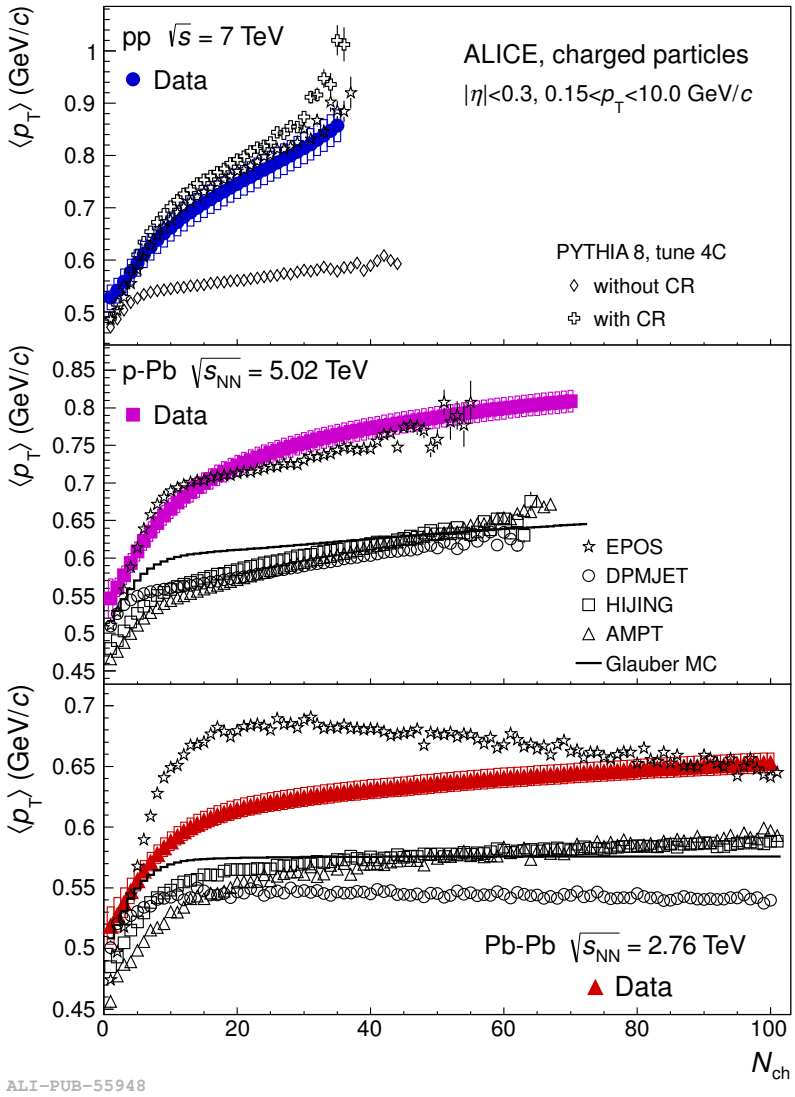

Figure 5.13.: Average transverse momentum $\langle p_{\mathrm{T}} \rangle$ as a function of charged-particle multiplicity in the range of $0.15 < p_{\mathrm{T}} < 10.0$ GeV/c for inclusive charged particles in pp, p–Pb and Pb–Pb collisions. The boxes represent the systematic uncertainties, statistical errors are of negligible size. The measured correlations are compared to different MC generators (see text). [40]

p–Pb for $n_{ch} > 14$ can be attributed to different production mechanisms. For higher multiplicities, $\langle p_{\mathrm{T}} \rangle$ in p–Pb flattens, while $\langle p_{\mathrm{T}} \rangle$ in pp collisions still rises with n_{ch}. In Pb–Pb collisions, $\langle p_{\mathrm{T}} \rangle$ has a strong rise with multiplicity for $n_{ch} < 14$, for higher n_{ch} $\langle p_{\mathrm{T}} \rangle$ only has a small rise.

In pp, higher multiplicities can only be reached by higher momentum transfer, which then results in more particles after the fragmentation. Due to the higher momentum transfer, these particles have higher p_{T} in the final state. A detailed explanation of

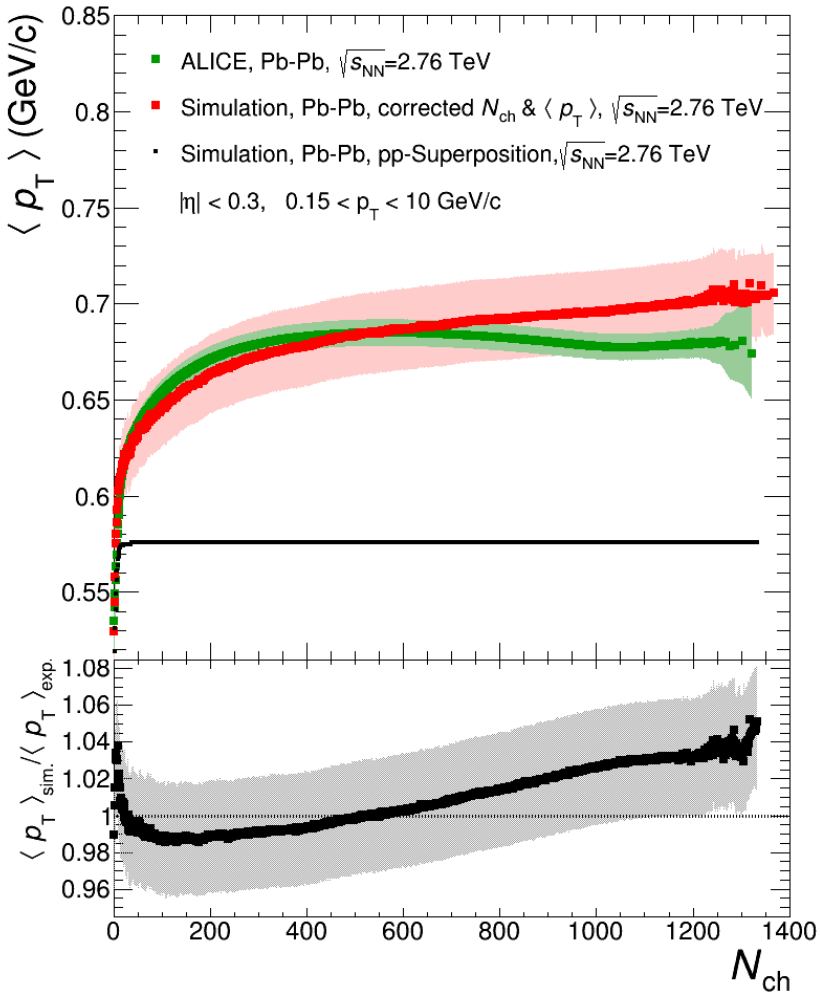

Figure 5.14.: $\langle p_T \rangle$ as function of the charged particle multiplicity in Pb–Pb collisions for the most recent calculation [45]. The green markers in the upper panel represent the measured correlation. As red squares the modeled correlation including all corrections is shown. The lower panel shows the ratio between the simulated and the measured correlation.

the different processes, which result in different measurements in pp, p–Pb and Pb–Pb collisions for $\langle p_T \rangle$ as function of n_{ch}, is presented in [40]; here in the following, only a brief summary is given.

In Pb–Pb collisions, higher multiplicities are reached in more central events. At lowest multiplicities ($n_{ch} \approx 1-3$) $\langle p_T \rangle$ in Pb–Pb collisions is in agreement with $\langle p_T \rangle$ in pp and p–Pb collisions, which can be attributed to the fact, that low multiplicity Pb–Pb events are created in very peripheral collisions, where only two protons at the outermost part of the nucleus collide. For increasing multiplicities, the collisions become more and more central. These collisions are then dominated by many soft interactions, which causes

$\langle p_{\mathrm{T}} \rangle$ to stay lower than in pp collisions.
In p–Pb collisions, low multiplicity events are thought to be produced in collisions of the proton with single protons in the corona (the outermost part) of the Pb-nucleus. These events are equal to pp collisions except for the fact, that the target nucleon is bound into a nucleus. Events with a larger number of tracks are attributed to collisions of the protons with the denser part of the Pb-nucleus closer to the center. These events can then consist of more collisions, e.g. with three protons in the nucleus, while the first has a high momentum transfer and the second and third have lower momentum transfer. This combination of one high-momentum transfer collision and two low-momentum transfer collisions leads to a higher $\langle p_{\mathrm{T}} \rangle$ at higher n_{ch} than in Pb–Pb collisions, but a smaller $\langle p_{\mathrm{T}} \rangle$ than in pp collisions, where these high multiplicity events occur at only one high-momentum transfer collision.
Fig. 5.13 shows $\langle p_{\mathrm{T}} \rangle$ of the measured data in comparison to MC generators separately for each collision system. Colored markers represent the measured data, while the black open markers show the model calculations. The uppermost panel shows the measurement in pp collisions together with the results of the MC generator Pythia8 [46], Tune 4C. In the publication, two different Pythia8 settings for the so-called color reconnections (CR) are discussed. The comparison of MC and data shows, that only the results including color reconnections can describe the measured data, while switching off color reconnections results in a lower $\langle p_{\mathrm{T}} \rangle$. The results obtained in p–Pb collisions are shown in the middle panel of Fig. 5.13 together with the results from five different MC generators. Most of the models (DPMJET, HIJING, AMPT and Glauber MC) underpredict the measured data by more than 25%. Only the EPOS model can describe the data.
The results in Pb–Pb collisions are shown in the lowest panel of Fig. 5.13. While DPMJET, HIJING, AMPT and the Glauber MC underpredict the data (as in p–Pb), but show a similar shape as the data, EPOS overpredicts the data.
In a recent analysis [47], the Glauber MC as shown in Fig. 5.13 has been improved. This new analysis includes measured data from p–Pb collisions to describe $\langle p_{\mathrm{T}} \rangle$ as function of multiplicity in Pb–Pb collisions. Fig. 5.14 shows the most recent calculation. The upper panel shows $\langle p_{\mathrm{T}} \rangle$ as function of multiplicity for the measured data as green markers and the model as red squares. The lower panel shows the ratio between the measurement and the model. Both agree within 5%.

After this short insertion with the discussion of particle production at low p_{T}, the following chapter will discuss in detail the particle production at high p_{T} in Pb–Pb collisions.

Chapter 6.

The Nuclear Modification Factor

As discussed in the introduction (chapter 2), energy loss mechanisms at play in a QGP created in Pb–Pb collisions can be studied by comparing the particle production at high p_{T} in Pb–Pb collisions to a reference particle production in pp collisions at the same energy. The transverse momentum spectra of charged particles in Pb–Pb and pp collisions have been presented in chapter 5.
This chapter focuses now on the nuclear modification factor R_{AA}, which has been introduced in section 2.3.4. This chapter is structured as follows: the first section describes the construction of a pp reference spectrum for center-of-mass energies of $\sqrt{s} = 2.76$ TeV and $\sqrt{s} = 5.02$ TeV based on the measurements presented in section 5.1.1. In the second section, R_{AA} as function of p_{T} and centrality is calculated using these pp reference spectra and the Pb–Pb data presented in section 5.1.2. Furthermore, an additional evaluation of particle production in the QGP based on the relative momentum loss of the particles is discussed. Finally, the chapter is concluded by results on the angular dependence relative to the event-plane of the collision of the charged particle production.

6.1. Construction of a pp reference

An important ingredient for the determination of the nuclear modification factor is the reference spectrum measured in proton-proton collisions. For Pb–Pb collisions at $\sqrt{s_{NN}} = 2.76$ TeV, pp collisions have been measured by ALICE at the same center-of-mass energy (see section 5.1.1). As the p_{T}-reach of the measured pp spectrum is smaller than the p_{T}-reach of the particle production measured in Pb–Pb collisions (compare Fig.

5.1 (pp) and Fig. 5.4, resp. Fig. 5.8 (Pb–Pb), the measured pp spectrum needs to be extrapolated to higher p_{T}. In the following, this *extrapolation* is described. The analysis has been part of a joint effort [39] with the results published in [35] and is part of this work.

6.1.1. Extrapolation

Fig. 6.1 shows the differential cross section of inclusive charged particles measured in pp collisions at $\sqrt{s} = 2.76$ TeV (datapoints in the upper panel as in Fig. 5.1) together with a parametrization by a so-called *modified Hagedorn function* [48] for $5 < p_{\mathrm{T}} < 32$ GeV/c. The function used here is defined as:

$$\frac{1}{2\pi p_T}\frac{d^2\sigma_{\mathrm{ch}}}{d\eta dp_T} = A\frac{p_T}{m_T}\left(1+\frac{p_T}{p_{T,0}}\right)^{-n} \tag{6.1}$$

m_T denotes the transverse mass $m_T = \sqrt{m_{eff}^2 + p_T^2}$. Here, an effective mass of $m_{eff} = 140$ MeV/c has been assumed for all particles. $p_{T,0}$ is a free parameter in the parametrization. For small p_{T}, the term $\left(1+\frac{p_T}{p_{T,0}}\right)^{-n}$ behaves like an exponential function with an inverse slope parameter of $p_{T,0}/n$ while for large p_{T} the Hagedorn function behaves like a power-law function. The transverse momentum spectrum in Fig. 6.1 shows a clear power-law dependence, i.e. a linear dependence on a log-log plot, on p_{T} for $p_{\mathrm{T}} > 10$ GeV/c, as expected from pQCD calculations. The modified Hagedorn function describes the cross section better over a wider range in p_{T} than a simple power-law function. The resulting parametrization is then extrapolated to higher p_{T}. The continuous red line shows the parametrization of the measured data, the dashed red line represents the extrapolation for $p_{\mathrm{T}} > 32$ GeV/c.

The ratio of data and fit is shown in the lower panel. Open circles show datapoints, which have been used for the evaluation of the systematic uncertainty of the parametrization only. The filled markers show, that the spectrum is well described by the parametrization. The grey band indicates the systematic uncertainty of the measured data. To evaluate the systematic uncertainty of the extrapolated reference, the lower end of the fit range of the parametrization has been varied by $p_{\mathrm{T}} = \pm 2$ GeV/c. The total systematic uncertainty of the extrapolated reference is shown as a red box in the lower panel. As the influence of the variation of the fit range is higher at higher p_{T} due to the leverarm, the systematic uncertainty increases here.

The final reference as used in this work is constructed with the measured datapoints up

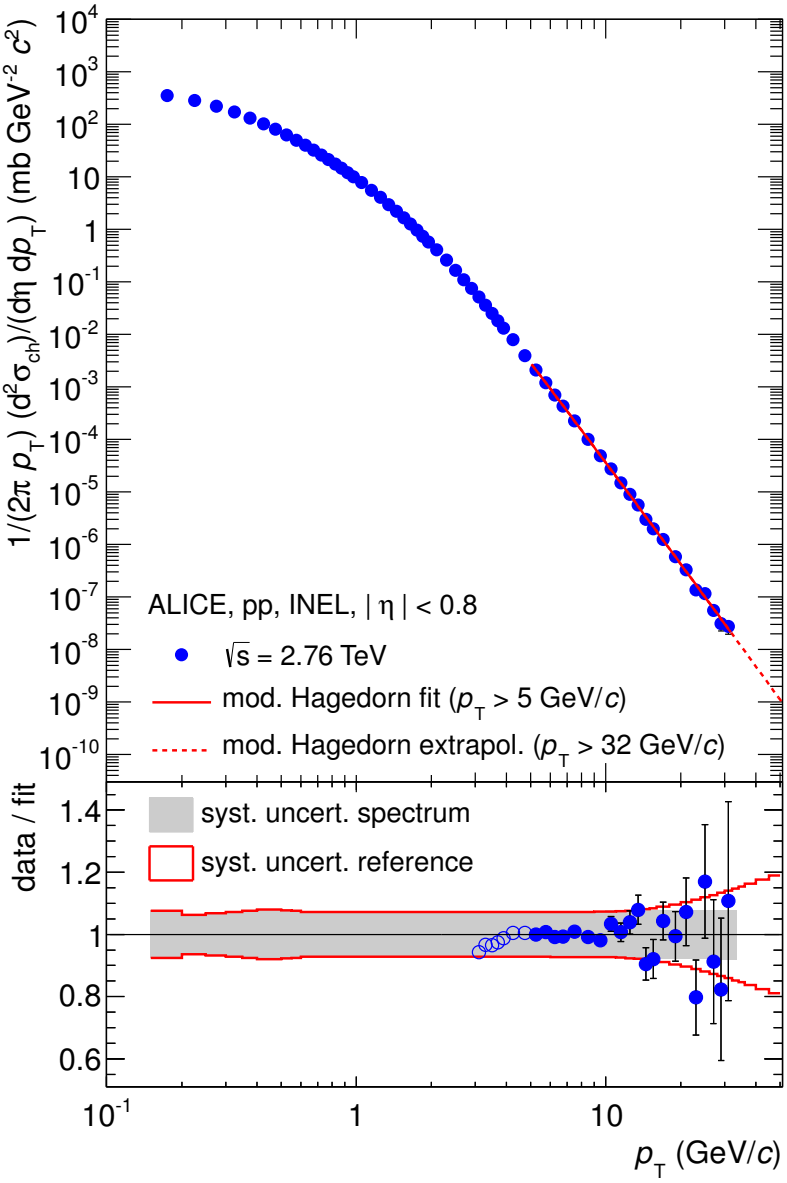

Figure 6.1.: Top: Differential cross section of inclusive charged particles in inelastic pp collisions at $\sqrt{s} = 2.76$ TeV as a function of p_{T} together with a modified Hagedorn parametrization for $p_{\mathrm{T}} > 5$ GeV/c. Bottom: Ratio of data to parametrization. The grey band indicates the total p_{T} dependent systematic uncertainty of the data, open circles show data points only used for the evaluation of the systematic uncertainty of the parametrization. [35]

to $p_{\mathrm{T}} = 5$ GeV/c. For higher p_{T}, the parametrization is used to smooth the statistical fluctuations and to extend the p_{T} reach. The reference is shown later in this chapter in Fig. 6.4. Including of EMCal-triggered data to increase the p_{T} reach and to reduce the

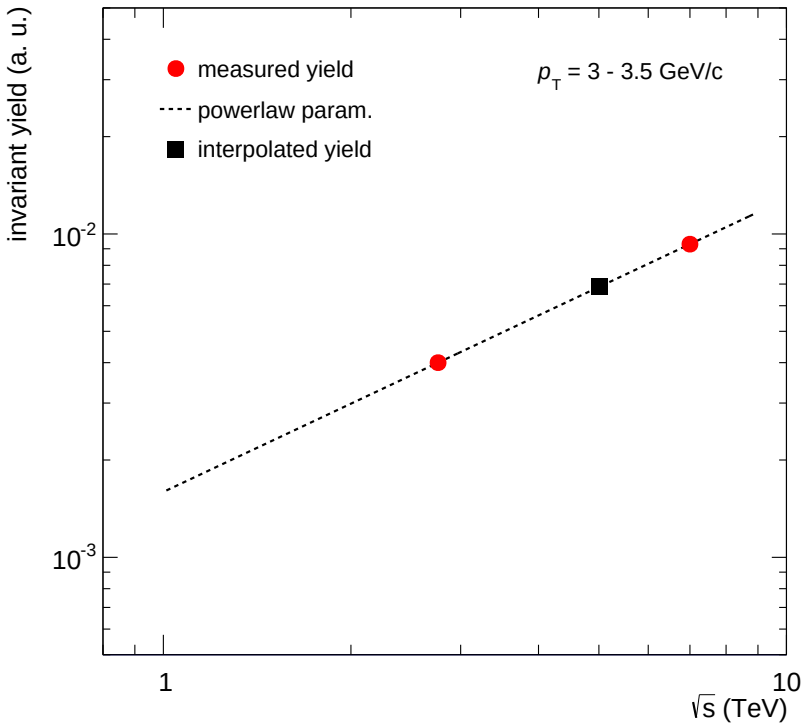

Figure 6.2.: Concept of the interpolation method for a pp reference at $\sqrt{s} = 5.02$ TeV. The measured yields for a fixed p_{T} are parametrized by a powerlaw function, the yield at any given energy in between can be interpolated.

systematic uncertainties has been studied with MC generators in [49] and is currently being implemented and tested on measured data.

6.1.2. Interpolation and Scaling

If no data from pp collisions is available at the same center-of-mass energy as the Pb-Pb collisions, an *interpolation and scaling* procedure can be applied on measured data at different center-of-mass energies to extract a pp reference spectrum at the energy of interest. In ALICE, this procedure has been applied in the publication of R_{AA} based on the data taking period LHC10h before the measurement of the pp reference spectrum at $\sqrt{s} = 2.76$ TeV [4]. Furthermore, a pp reference has been constructed in the same way for the publication of the nuclear modification factor in p–Pb collisions at $\sqrt{s_{NN}} = 5.02$ TeV [50] as no reference at this energy was available at the time of the publication[1]. The

[1]The data measured in 2016 in pp and Pb–Pb collisions at $\sqrt{s} = 5.02$ TeV is currently being analyzed (status end of 2016).

construction of both references is part of this work. The procedure will be discussed in the following for the latter case; here, a split approach is used.

Interpolation

For $p_{\mathrm{T}} < 5$ GeV/c the measured pp yields at $\sqrt{s} = 2.76$ TeV and $\sqrt{s} = 7$ TeV (as shown in Fig. 5.1) are interpolated for a fixed p_{T} with a power-law function. This power-law behaviour is suggested by the inclusive measurement of the charged particle pseudorapidity density as function of the center-of-mass energy [51]. Figure 6.2 shows the concept of this interpolation procedure. Red circles show the measured yields at $\sqrt{s} = 2.76$ TeV and $\sqrt{s} = 7$ TeV for an exemplary p_{T} interval of $3 < p_{\mathrm{T}} < 3.5$ GeV/c. The powerlaw parametrization is depicted as a dashed line, the full square shows the interpolated yield at $\sqrt{s} = 5.02$ TeV. This procedure is repeated for all p_{T} intervals.

Scaling

For $p_{\mathrm{T}} \geq 5$ GeV/c a different approach is used. Fig. 6.3 shows the ratios of the NLO calculations from Fig. 5.1 as function of p_{T} on top of the same ratios measured in pp collisions. Although the absolute values of the NLO calculation overpredict the measured data by a factor two (compare Fig. 5.1), the ratios obtained from NLO and measured data agree over a wide range in p_{T}. This good agreement can also be seen in the lower panel of Fig. 6.3, where the ratio of data and NLO is shown. A variation of the renormalization and factorization scale of the NLO calculation gives a systematic uncertainty on the double ratio of 0.5–23.6 % for 0.9 TeV / 2.76 TeV, 1.0–37.8% for 0.9 TeV / 7 TeV and 2.4–12.3% for 2.76 TeV / 7 TeV. The agreement between NLO and data is better for smaller differences in beam energies. To construct the pp reference, measured data at a different center-of-mass energy is scaled by the ratio obtain from the NLO calculation. For $p_{\mathrm{T}} > 5$ GeV/c the measured yield at $\sqrt{s} = 7$ TeV is scaled down to the center-of-mass energy of $\sqrt{s} = 5.02$ TeV:

$$\mathrm{d}^2\sigma^{\mathrm{pp}}_{ch}/\mathrm{d}\eta\mathrm{d}p_{\mathrm{T}}\,|_{5.02TeV} = \frac{\mathrm{d}^2\sigma^{\mathrm{pp}}_{ch}/\mathrm{d}\eta\mathrm{d}p_{\mathrm{T}}\,|_{\mathrm{NLO},5.02TeV}}{\mathrm{d}^2\sigma^{\mathrm{pp}}_{ch}/\mathrm{d}\eta\mathrm{d}p_{\mathrm{T}}\,|_{\mathrm{NLO},7TeV}} \times \mathrm{d}^2\sigma^{\mathrm{pp}}_{ch}/\mathrm{d}\eta\mathrm{d}p_{\mathrm{T}}\,|_{7TeV} \tag{6.2}$$

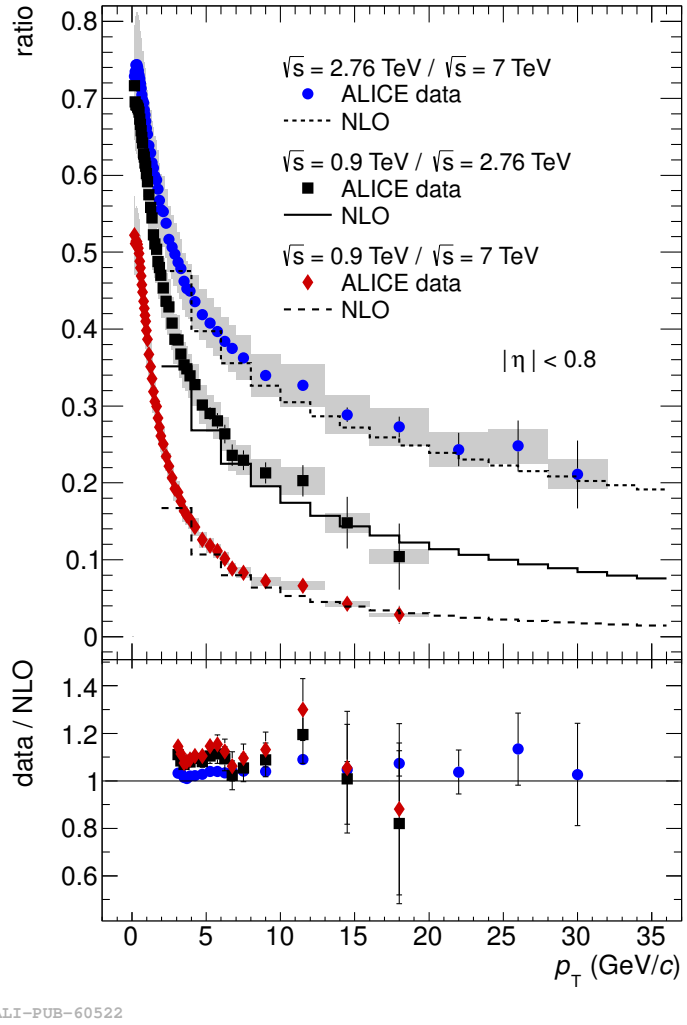

Figure 6.3.: Top: Ratio of differential cross sections of charged particles in INEL pp collisions at different collision energies as a function of p_{T}. Grey boxes denote p_{T} dependent systematic uncertainties. Normalization uncertainties are not shown (see text for details). The histograms show the same ratio determined from NLO calculations. Bottom: Ratio of data and NLO calculations derived from the upper panel. [35]

Combined Methods

The constructed combined reference at $\sqrt{s} = 5.02$ TeV is shown in Fig. 6.4 as orange markers. For $p_{\mathrm{T}} > 20$ GeV/c the data is parametrized with a power-law function, which can be used to smooth statistical fluctuations. As mentioned, historically, a similar approach has been used for the first publication of the charged particle R_{AA} measured by ALICE at $\sqrt{s_{NN}} = 2.76$ TeV (part of this work). Here, three different references have been determined:

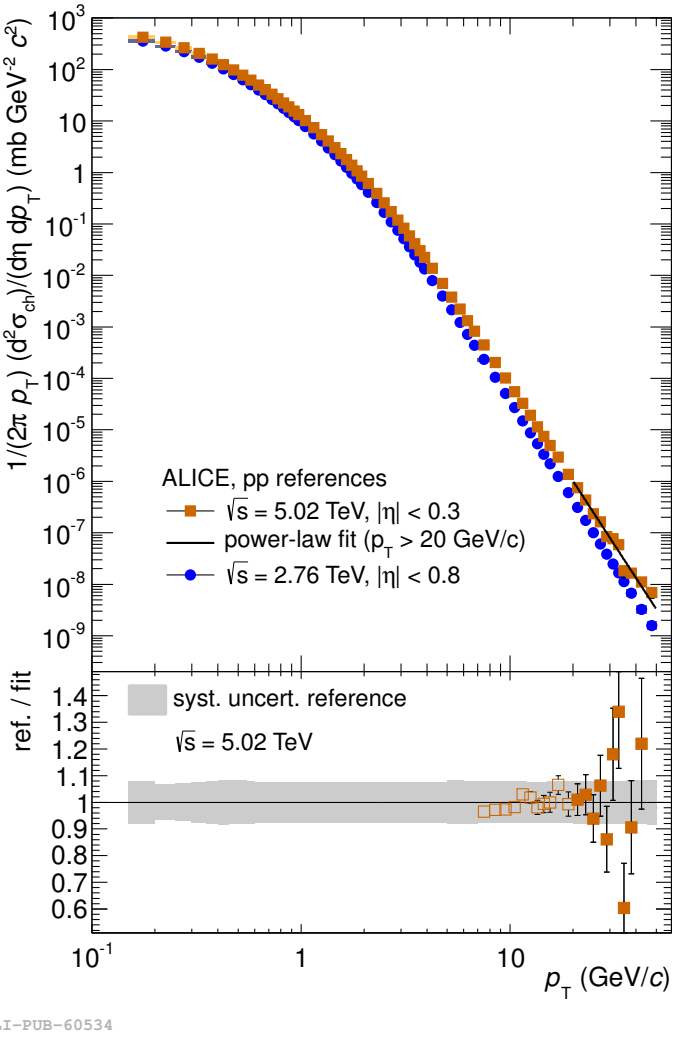

Figure 6.4.: Top: Extrapolated pp reference at $\sqrt{s} = 2.76$ TeV as a function of p_{T} as blue markers. Orange markers show the constructed pp reference at $\sqrt{s} = 5.02$ TeV as a function of p_{T} together with a power-law parametrization for $p_{\mathrm{T}} > 20$ GeV/c. Bottom: Ratio of data to parametrization. The grey band indicates the total p_{T} dependent systematic uncertainty of the data, open circles show data points only used for the evaluation of the systematic uncertainty of the parametrization. [35]

(I) interpolation between data measured by ALICE at $\sqrt{s} = 0.9$ TeV and $\sqrt{s} = 7$ TeV

(II) interpolation between data measured by CDF at $\sqrt{s} = 1.96$ TeV [52] and ALICE at $\sqrt{s} = 7$ TeV

(III) scaling of data measured by ALICE at $\sqrt{s} = 0.9$ TeV

The first one (I) has been used as main reference for the publication, while the others(II,III) served as a cross check. The three references are shown later in this chapter in Fig. 6.5 for the resulting R_{AA}.

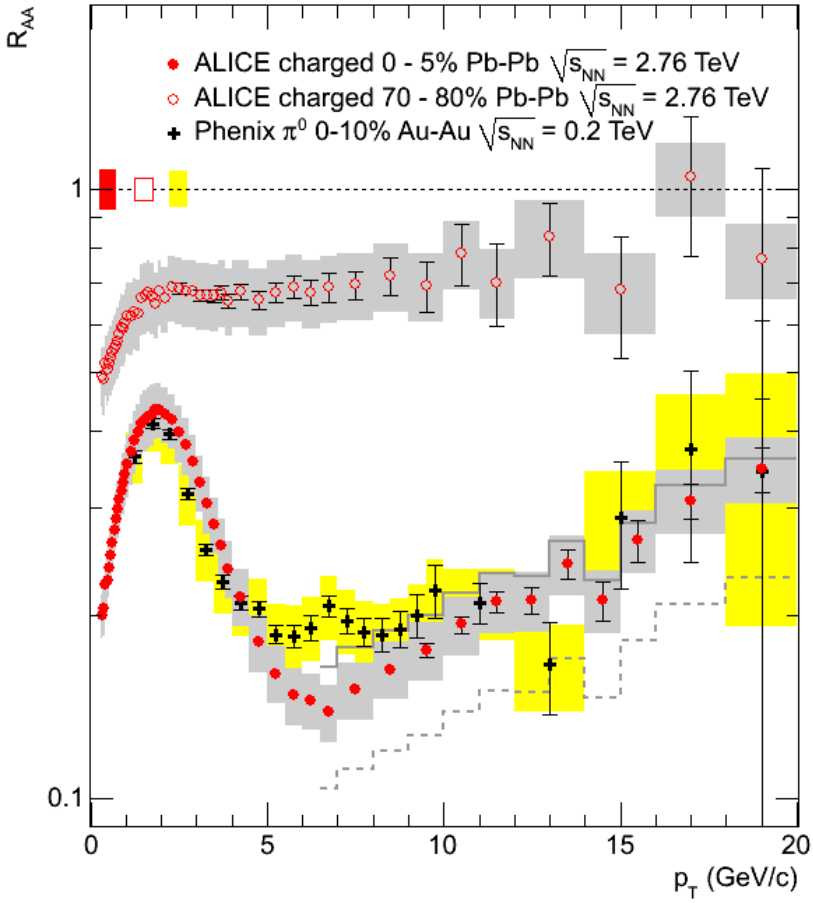

Figure 6.5.: R_{AA} in central (0–5%) and peripheral (70–80%) Pb–Pb collisions at $\sqrt{s_{NN}} = 2.76$ TeV measured in ALICE as red markers [4]. Black crosses represent the measurement of neutral pions of PHENIX at $\sqrt{s_{NN}} = 0.2$ TeV in Au–Au collisions [53].

6.2. Minimum Bias R_{AA}

One of the first results of the first heavy-ion beamtime at the LHC in 2010 was the nuclear modification factor of charged particles published by ALICE [4]. As discussed, no pp reference was measured at that time and at that energy and therefore the pp reference discussed at the end of the previous chapter has been used. The resulting R_{AA} as a function of p_{T} is shown in Fig. 6.5 for two different centrality selections as red markers in comparison to earlier measurements by PHENIX at RHIC [53]. For central collisions, not only the default pp reference (I) as discussed in the previous section is shown, but also the two alternative approaches. The solid line represents the interpolated reference (II), the dashed line shows the reference from the scaling approach (III).

Publication	Pb–Pb data taking period	pp reference(s)
[4]	LHC10h	(I) interpolation ($\sqrt{s} = 0.9$ TeV and 7 TeV) (II) interpolation ($\sqrt{s} = 1.96$ TeV and 7 TeV) (III) NLO scaling ($\sqrt{s} = 0.9$ TeV)
[3]	LHC10h	(IV) extrapolation ($\sqrt{s} = 2.76$ TeV)
this work	LHC10h, LHC11h	(IV) extrapolation ($\sqrt{s} = 2.76$ TeV)

Table 6.1.: Publications of R_{AA} in ALICE with the corresponding Pb–Pb data sets (see Tab. 4.2) and pp references.

The comparison of R_{AA} of charged particles at the LHC energy and R_{AA} of neutral pions at the RHIC energy shows that the R_{AA} agrees between RHIC and LHC energies within systematic uncertainties. If the fractional energy loss at LHC energies is similar to the one at RHIC energies, R_{AA} at the LHC would be higher than at RHIC, due to the harder, i.e. flatter, pp reference spectrum. The observation in the data implies however that the suppression observed at the LHC is stronger than at RHIC. Due to the limited p_{T} reach of the charged particle spectra in PHENIX, here π^0 measured in PHENIX with a higher p_{T} reach are used for the comparison. This is justified as pions are the dominant contribution to the inclusive charged particle spectra at RHIC and it is assumed that charged pions and neutral pions undergo the same processes (production and suppression). In the PHENIX publication it is suggested, that the suppression of pions is constant above $p_{\mathrm{T}} \approx 5$ GeV/c with a suppression factor of ≈ 5. In contrast, R_{AA} at the LHC shows a strong rise with p_{T}. The direct comparison in Fig. 6.5 shows, that a rise of R_{AA} with p_{T} in principle is also visible in PHENIX. The Pb–Pb data sets used in the analyses and the corresponding pp references are once more summarized in table 6.1.

In the pp beamtime in 2011, ALICE has measured a reference spectrum at $\sqrt{s} = 2.76$ TeV, i.e. at the same center-of-mass energy as in Pb–Pb collisions. Based on the reference spectrum presented in section 6.1.1, including the extrapolation to higher p_{T} (see Fig. 6.4), an extension of R_{AA} up to $p_{\mathrm{T}} = 50$ GeV/c was published [3]. The R_{AA} for minimum bias collisions was already discussed in chapter 2, Fig. 2.9. It is slightly lower than in the preceding publication [4], but agrees with it within the systematic uncertainties given by the alternative references. The corresponding data sets are quoted in table 6.1 as well.

As part of this work, a re-analysis of the data set from the data taking period LHC10h as

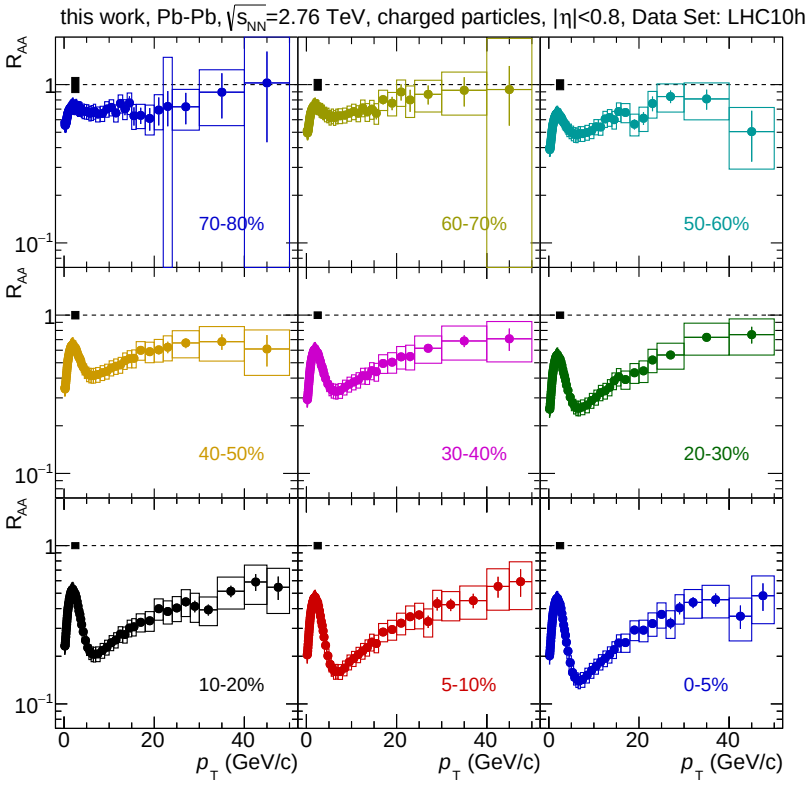

Figure 6.6.: R_{AA} as function of p_{T} for inclusive charged particles for the Pb–Pb data set from the data taking period LHC10h for nine different centrality intervals calculated with the pp reference (IV).

well as a new analysis of the data set from the data taking period LHC11h are presented. For both data sets, the extrapolated pp reference (IV) as presented in section 6.1.1 is used. A detailed description of the analysis has been discussed in chapter 4. Fig. 6.6 shows R_{AA} in Pb–Pb collisions at $\sqrt{s_{NN}} = 2.76$ TeV based on the re-analysis of the data set from the data taking period LHC10h for nine different centrality intervals based on the p_{T} spectra presented in section 5.1.2. Fig. 6.7 shows R_{AA} in Pb–Pb collisions at $\sqrt{s_{NN}} = 2.76$ TeV from the data set from the data taking period LHC11h. The underlying invariant yield measured in Pb–Pb collisions has been measured up to $p_{\mathrm{T}} = 50$ GeV/c for LHC10h and up to $p_{\mathrm{T}} = 100$ GeV/c for LHC11h. Error bars in the plots show statistical errors of the Pb–Pb spectra, while boxes show the quadratic sum of the systematic uncertainties of the Pb–Pb spectra and the pp reference spectrum as well as the statistical errors of the pp reference spectrum.

For both data taking periods R_{AA} shows a similar behaviour: in central collisions a clear suppression is observed with a minimum in R_{AA} for $p_{\mathrm{T}} = 6 - 7$ GeV/c and a rise towards higher p_{T}. The maximum at lower p_{T} can be explained by contributions from

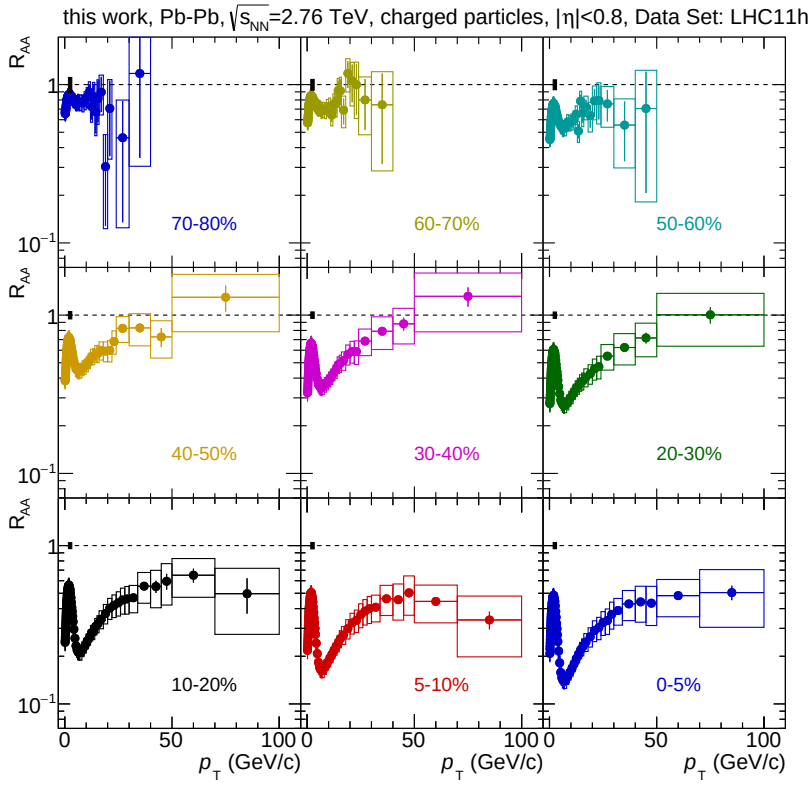

Figure 6.7.: R_{AA} as function of p_{T} for inclusive charged particles for the Pb–Pb data set from the data taking period LHC11h for nine different centrality intervals calculated with the pp reference (IV).

flow (compare section 2.3.2). Towards higher p_{T}, R_{AA} rises with a hint of a plateau at $p_{\mathrm{T}} = 50 - 100$ GeV/c, but no conclusion can be drawn within the systematic uncertainties, which are dominated by the extrapolation of the reference.

With the analysis of the data set from the data taking period LHC11h in this work, the p_{T}-reach of R_{AA} in central events is extended by a factor two compared to the previously published results based on the data set from the data taking period LHC10h [3]. With the higher p_{T} reach in this work, the region of $p_{\mathrm{T}} = 50 - 100$ GeV/c is now accessible. As suggested by theory, the QGP becomes more and more transparent for particles with higher momenta, i.e. these particles have a smaller energy loss. This phenomenon, the so-called *punch-through*, results in an R_{AA} closer to unity, which means, that the suppression of the charged particle production in Pb–Pb collisions at high p_{T} would be much smaller than at low p_{T}. However, Fig. 6.7 suggests a plateau within the newly accessible p_{T} range, but a punch-through cannot be excluded within the systematic uncertainties. If a punch-through exists, the results of this work suggest however, that it occurs for charged particle with even higher p_{T}, i.e. $p_{\mathrm{T}} > 100$ GeV/c.

Going to more peripheral collisions, the suppression as well as the p_{T} dependence decreases, resulting in a nearly p_{T}-independent R_{AA} for the most peripheral collisions (centrality 70 - 80 %). This observation was already discussed along Fig. 5.4 (LHC10h) and Fig. 5.8 (LHC11h), where the invariant yield in Pb–Pb collisions has been compared to the binary scaled pp reference earlier in the text.
As discussed in chapter 5, the charged particle spectra in Pb–Pb collisions obtained in the re-analysis of the data set from the data taking period LHC10h agree with the spectra in [3] within $< 5\%$. This proofs, that the analysis code developed in this work can reproduce the preceding, published analysis. Therefore this analysis code can be used to analyze the data set from the data taking period LHC11h, which is original to this work.
In the following sections, results based on the data set from the data taking period LHC11h only will be presented, as the p_{T}-reach is higher for central and semi-central collisions in this data set.

6.3. Relative Transverse Momentum Loss

The p_{T} dependence and overall behaviour of the nuclear modification factor of charged particles at high p_{T} as presented in the previous section is commonly attributed to effects of an energy loss of the underlying partons in the QGP before the fragmentation into hadrons as discussed in chapter 2. To further constrain this energy loss of a parton at high p_{T}, additional measurements are needed. Experimentally, the energy loss of a parton in the medium is not accessible directly. A measurable approximation of the parton energy loss has been suggested in [5], where the relative energy loss $\Delta E/E$ of a parton in the QGP is approximated by the relative transverse momentum loss $S_{loss} = \Delta p_{\mathrm{T}}/p_{\mathrm{T}}$ of hadrons. In contrast to R_{AA}, S_{loss} does not assume a suppression of the particle production, but a change in the p_{T} of the produced particles. To evaluate this change in p_{T}, the p_{T} of a given yield in N_{coll} scaled pp collisions is compared to the p_{T} of the same yield in Pb–Pb collisions. In practical terms S_{loss} is determined by a comparison of the p_{T}-dependent yield in pp (x N_{coll}) and Pb–Pb collisions. Both spectra are compared at the same absolute value of the yield; the corresponding p_{T} values $p_{\mathrm{T},pp}$ and $p_{\mathrm{T},Pb-Pb}$ lead to the absolute difference Δp_{T}. For Pb–Pb collisions, this yield is the measured quantity, while for pp a parametrization is used. This difference is compared to the p_{T} of the pp

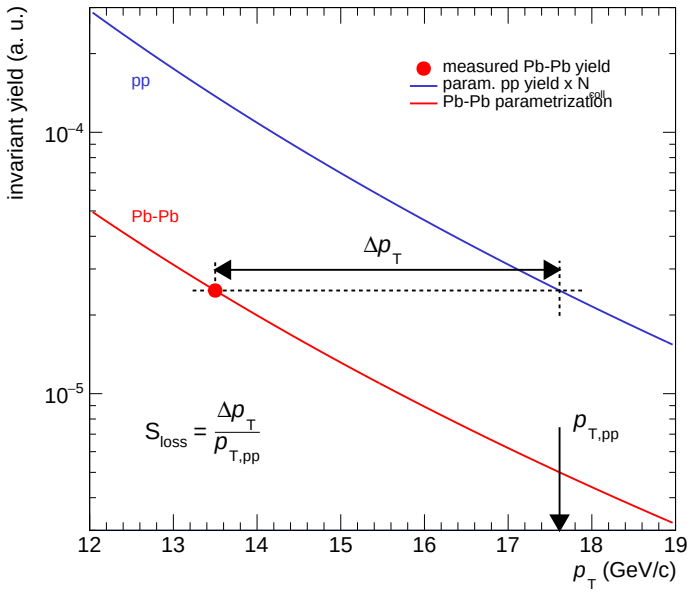

Figure 6.8.: Concept of the determination of the relative momentum loss S_{loss}.

reference spectrum $p_{\mathrm{T},pp}$ to obtain the relative transverse momentum loss S_{loss}:

$$S_{loss} = \frac{\Delta p_{\mathrm{T}}}{p_{\mathrm{T},pp}} = \frac{p_{\mathrm{T},Pb-Pb}|_{yield,Pb-Pb} - p_{\mathrm{T},pp}|_{yield,Pb-Pb}}{p_{\mathrm{T},pp}} \tag{6.3}$$

The concept of this calculation is visualized in Fig. 6.8.

A recent measurement of the S_{loss} parameter of neutral pions has been presented for Au–Au collisions at $\sqrt{s} = 200$ GeV [5] and is shown in Fig. 6.9. Here, S_{loss} is constant up to $p_{\mathrm{T}} = 10$ GeV/c and slowly decreases at higher p_{T} for minimum bias, central and semi-central collisions. For peripheral collisions, S_{loss} is nearly p_{T}-independent. This behavior is consistent with the slow rise of R_{AA} with p_{T}, as a smaller parton energy loss in the medium can be related to a less suppressed spectrum measured in Pb–Pb collisions.

In this work, a measurement of the S_{loss} parameter of charged particles[2] based on data measured with ALICE is presented. Fig. 6.10 shows S_{loss} as function of p_{T} for charged particles measured in Pb–Pb collisions in ALICE at $\sqrt{s_{NN}} = 2.76$ TeV for central and peripheral events. For central events, S_{loss} has its maximum for $p_{\mathrm{T}} = 10$ GeV/c and decreases for higher p_{T}. This decrease in S_{loss} can also be seen in R_{AA} (compare Fig. 6.7), namely that R_{AA} increases for $p_{\mathrm{T}} = 10$ GeV/c to $p_{\mathrm{T}} = 40$ GeV/c. For higher p_{T},

[2] As discussed earlier in this chapter, for neutral pions and charged particles at high p_{T} a similar argumentation concerning energy loss should hold.

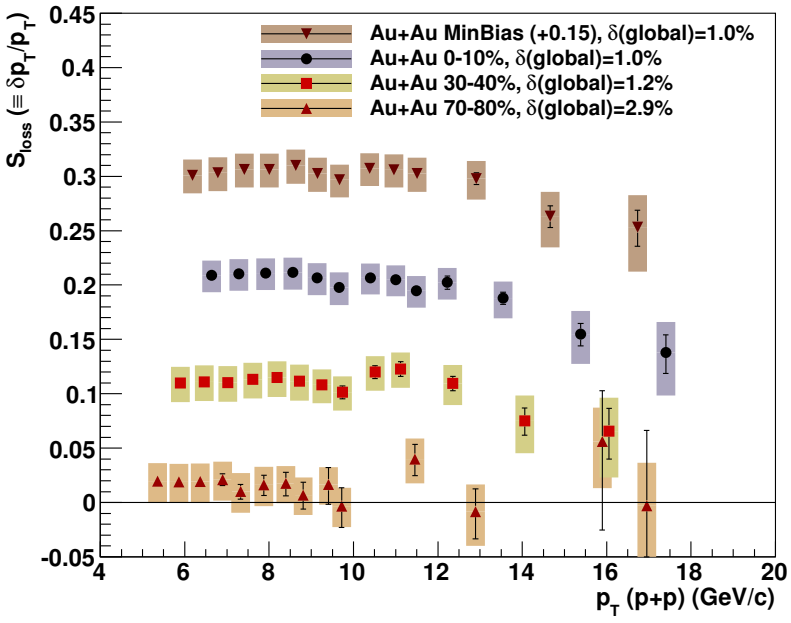

Figure 6.9.: S_{loss} parameter for neutral pions as function of p_{T} measured in Au–Au at $\sqrt{s_{NN}} = 200$ GeV collisions at PHENIX. [5]

R_{AA} has no p_{T}-dependence in central events. This is supported by S_{loss} (Fig. 6.10), which is p_{T}-independent for $p_{\mathrm{T}} \gtrsim 40$ GeV/c. This means, that charged particles produced in central events with $p_{\mathrm{T}} \gtrsim 40$ GeV/c are measured at transverse momenta, which are approximately 10% lower than the expected p_{T}. For peripheral events, S_{loss} has nearly no p_{T}-dependence. In addition, S_{loss} for peripheral events is smaller than in central events. Both properties are in line with the already observed behavior of R_{AA} as function of p_{T} in peripheral collisions: for $p_{\mathrm{T}} \gtrsim 10$ GeV/c, R_{AA} shows only a weak p_{T}-dependence. Furthermore, R_{AA} in peripheral collisions shows only a weak suppression of the particle production in Pb–Pb collisions compared to the particle production in pp collisions. All in all, Fig. 6.10 shows a similar general trend as observed in PHENIX, but as S_{loss} extends to higher p_{T} in ALICE compared to PHENIX, the decrease of S_{loss} with p_{T} is much more prominent.

To investigate the centrality dependence of S_{loss} even more, S_{loss} is analyzed for three different p_{T}-selections as function of centrality. Here, the p_{T}-selection is applied on the measured yield in Pb–Pb collisions.

- The first p_{T} selection probes the minimum of R_{AA}, where the suppression is largest ($6.5 < p_{\mathrm{T}} < 7$ GeV/c). This suppression originates in the largest momentum loss.

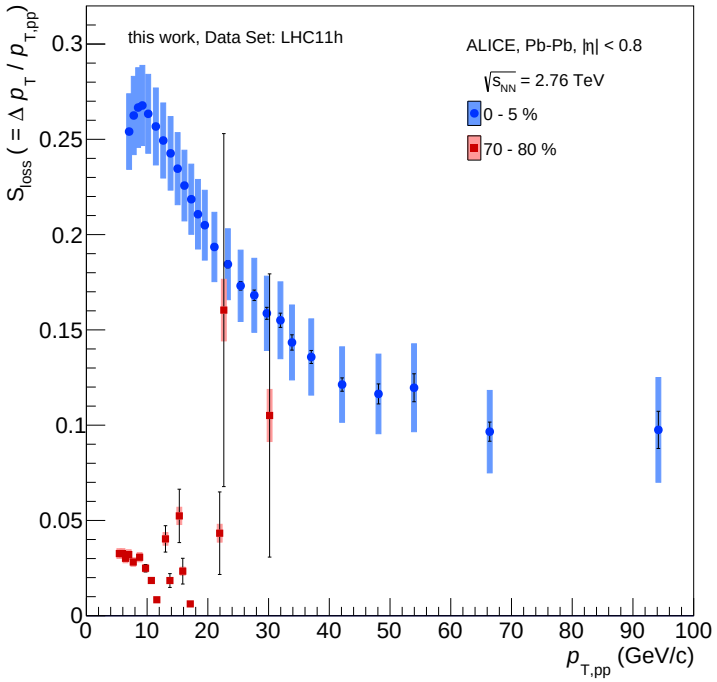

Figure 6.10.: S_{loss} parameter for charged particles as function of p_{T} measured in Pb–Pb collisions at ALICE for central and peripheral collisions for the data set LHC11h.

- The second p_{T} selection probes the rising of R_{AA} ($14 < p_{\mathrm{T}} < 15$ GeV/c). Here, the momentum loss is expected to be smaller than in the first p_{T} selection.
- The third p_{T} selection finally probes a potential plateau in R_{AA} ($30 < p_{\mathrm{T}} < 40$ GeV/c). Again, S_{loss} should be smaller than in the first two p_{T} selections.

Fig. 6.11 shows S_{loss} as a function of N_{part} (compare table 4.1 for the corresponding centrality classes) for the three p_{T} selections. Markers represent the calculated S_{loss}. The blue markers show S_{loss} for the first p_{T} selection, where the suppression in R_{AA} is highest; here, the largest S_{loss} is observed. For higher selected p_{T} (red markers for the second p_{T} selection, black markers for the third), S_{loss} is lower within each centrality class. For peripheral collisions, i.e. small N_{part}, the statistical errors increase. All three p_{T} selections show a clear centrality dependence. In Fig. 6.11 the measurement of S_{loss} is compared to a theory parametrization based on [6], similar to the comparison presented in [54]. The underlying model determines the energy loss of a parton traversing the QGP. In this model, the energy loss is proportional to $N_{part}^{2/3}$. The model assumes, that the relative energy loss to first order is proportional to the gluon density in the

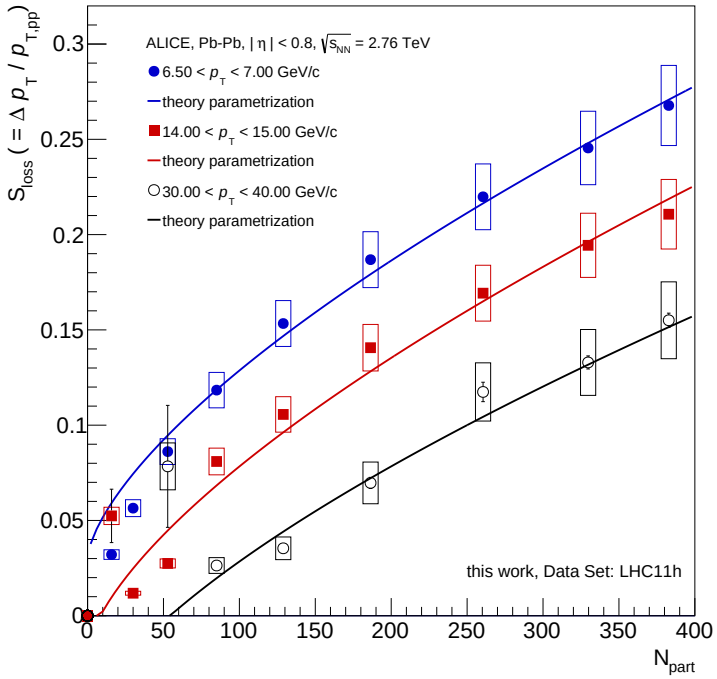

Figure 6.11.: S_{loss} parameter for charged particles as function of centrality measured in Pb–Pb collisions at ALICE for three different momentum selections together with a parametrization.

medium dN_g/dy, the path-length L of the particle[3] in the medium and anti-proportional to the transverse area A_T of the created medium:

$$\frac{\Delta E}{E} \propto \frac{dN_g}{dy} L \frac{1}{A_T} \tag{6.4}$$

All three quantities depend on the number of participants:

$$\frac{dN_g}{dy} \propto N_{part} \tag{6.5}$$

$$L \propto N_{part}^{1/3} \tag{6.6}$$

$$\frac{1}{A_T} \propto N_{part}^{-\frac{2}{3}} \tag{6.7}$$

which results in the following simplified parametrization of the model:

$$\frac{\Delta E}{E} \propto N_{part}^{2/3} \tag{6.8}$$

[3]The model itself determines the energy loss for jets. For this work, high p_{T} single particles are assumed to behave similarly.

For the analysis, it is assumed, that the relative transverse momentum loss of the charged particles is proportional to the relative energy loss of the partons:

$$S_{loss} = \frac{\Delta p_{\mathrm{T}}}{p_{\mathrm{T}}} \approx \frac{\Delta E}{E} = a \cdot N_{part}^{2/3} \tag{6.9}$$

In this simplified parametrization of the model, the amplitude a contains information about the medium, e.g. the strong coupling constant α_s. Due to the complex interplay between these parameters they have not been treated separately. The measured data in Fig. 6.11 is then parametrized with equation 6.9 to evaluate the centrality dependence suggested by the model.
The parametrizations are shown in Fig. 6.11 with the same color code as the markers for the three p_{T} selections as function of N_{part}. The parametrizations are in agreement with the measured data within the systematic uncertainties. Following the theory, this implies a linear dependence of the energy loss on the path-length of the particle in the medium. Due to the simplification applied in this analysis, the reality might be more complex, however. Therefore, the dependence of particle production on the path-length L in the medium will be investigated more thoroughly in the following section.

6.4. Event-plane Dependent Nuclear Modification Factor

As discussed in section 2.3.2 a typical almond-shaped overlap region between the two nuclei is formed in a semi-central Pb–Pb collision. Depending on the azimuthal angle of a particle produced in the medium relative to the azimuthal angle of the event-plane, which is created in this overlap region, the particle traverses different path-lengths in the medium. Fig. 6.12 shows the path-length obtained from a Glauber MC for charged particles in Pb–Pb collisions at $\sqrt{s_{NN}} = 2.76$ TeV as function of centrality for two different selections of the azimuthal angle ϕ of the particle relative to the second-order event-plane angle Ψ_2. In this analysis, the selection $0 \leq |\phi - \Psi_2| \leq \frac{\pi}{4}$ is labeled *in-plane* and the selection $\frac{\pi}{4} < |\phi - \Psi_2| \leq \frac{\pi}{2}$ is labeled *out-of-plane*. A schematic view of the definition of this selection is shown in Fig. 6.13.
The path-length decreases for more peripheral events for both selections, which is related to the increasing impact parameter b (compare table 4.1). While the path-length in-plane and out-of-plane agrees for central collisions, their difference (black line in Fig. 6.12) increases towards more peripheral and has its maximum for semi-central collisions (50 -

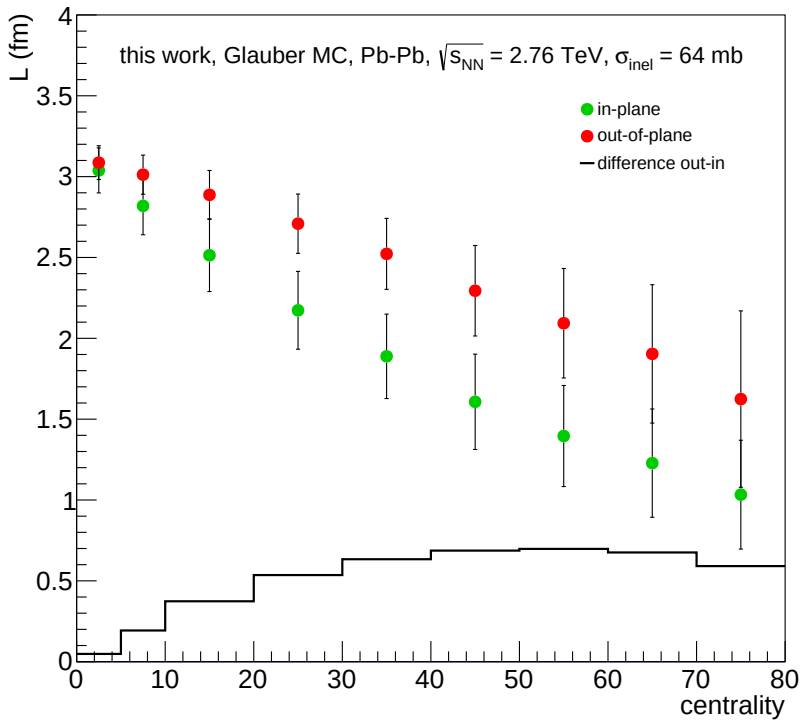

Figure 6.12.: Path-length determined with a Glauber Monte Carlo simulation as function of centrality. Red markers represent the path-length for out-of-plane particle production, green markers the path length for in-plane particle production. As black line the difference between out-of-plane and in-plane path length is shown.

60%). This difference only slightly decreases for more peripheral collisions.
Depending on the azimuthal angle of the produced particle relative to the event-plane angle, the suppression observed in R_{AA} is expected to be larger for longer path-lengths through the medium (out-of-plane) or smaller for shorter path lengths through the medium (in-plane) (compare Fig. 4.3). Fig. 6.14 shows R_{AA} as function of p_{T} for charged particles in Pb–Pb collisions at $\sqrt{s_{NN}} = 2.76$ TeV for nine different centrality intervals for LHC11h for the above mentioned two event-plane selections as well as for the inclusive measurement. Full markers show the inclusive R_{AA}, while open squares represent the out-of-plane measurement and open circles the in-plane measurement. The observed suppression is different for all three selections: as expected, the out-of-plane measurements show the highest suppression due to the longest path length through the medium. The measurement in-plane has the smallest suppression as the path-length is shortest. The inclusive measurements are in between, as there the measurements are averaged over all path-length. As expected from Fig. 6.12, the difference between in-

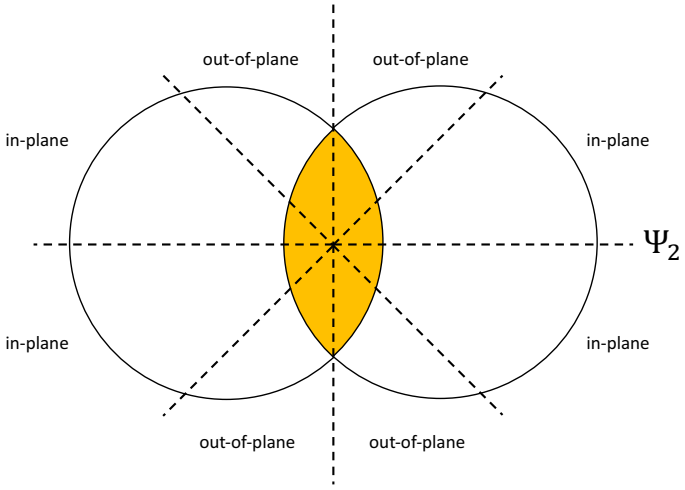

Figure 6.13.: Schematic view of the partitioning of the azimuthal angle distribution of produced particles relative to the event-plane Ψ_2 into the two different classes *in-plane* and *out-of-plane*.

and out-of-plane is small for central collisions and increases towards more peripheral collisions. The inclusive measurement can be compared to a theoretical expectation of the path-length dependence of R_{AA} as presented in [7]. In this model R_{AA} is determined as

$$R_{\mathrm{AA}} \propto \exp\left[-\frac{2\alpha_s C_F}{\sqrt{\pi}} L \sqrt{\hat{q}\frac{\mathcal{L}}{p_{\mathrm{T}}}}\right] \tag{6.10}$$

The parameters are defined as follows:

- L is the path-length in the medium
- C_F is the *Casimir Factor*, which depends on the origin of the fragmented hadron
- $\mathcal{L}$ is the so-called *spectral index*, i.e. the power of the underlying pp-p_{T}-spectrum.
- α_s is the strong coupling constant and a free parameter in the model.
- $\hat{q}$ is the average momentum transfer per unit length in the medium and is a free parameter in the model.

In the following application of the model to the data, the parameters are determined as follows:

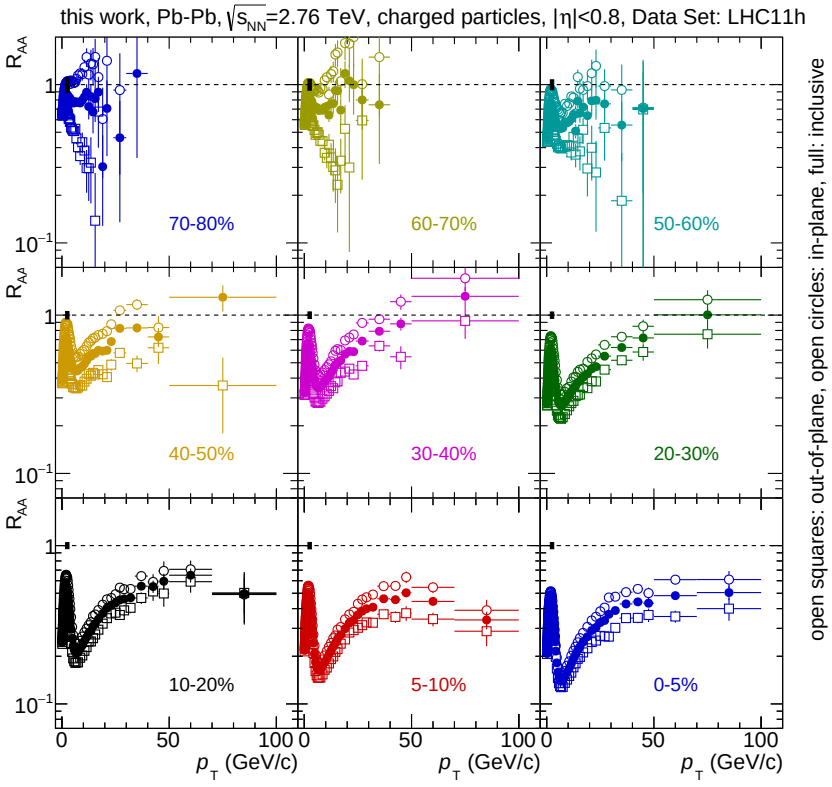

Figure 6.14.: Nuclear Modification Factor as function of p_{T} for inclusive charged particles in Pb–Pb collisions at $\sqrt{s_{NN}} = 2.76$ TeV with in- and out-of-plane measurements.

- The average path-length L in the medium is obtained from a Glauber MC calculation for the different centrality selections (compare Fig. 6.12).
- The *Casimir Factor* is determined as

$$C_F = x_{quark} \cdot \frac{4}{3} + x_{gluon} \cdot 3$$

  where x_{quark} (x_{gluon}) is the relative abundance of quarks (gluons). In this analysis, the relative abundances are taken from [55].
- The spectral index $\mathcal{L}$ is obtained from a power-law fit to the measured data at $\sqrt{s} = 2.76$ TeV (compare Fig. 5.1).

To constrain the free parameters α_s and $\hat{q}$, the inclusive measured R_{AA} in different centrality classes is parametrized with eq. 6.10. These parametrizations are shown in Fig. 6.15 in comparison to the data. Markers represent the measured data of R_{AA}, while lines show the model parametrizations as discussed above. The gray band shows the systematic uncertainty of the parametrization arising from the variation of

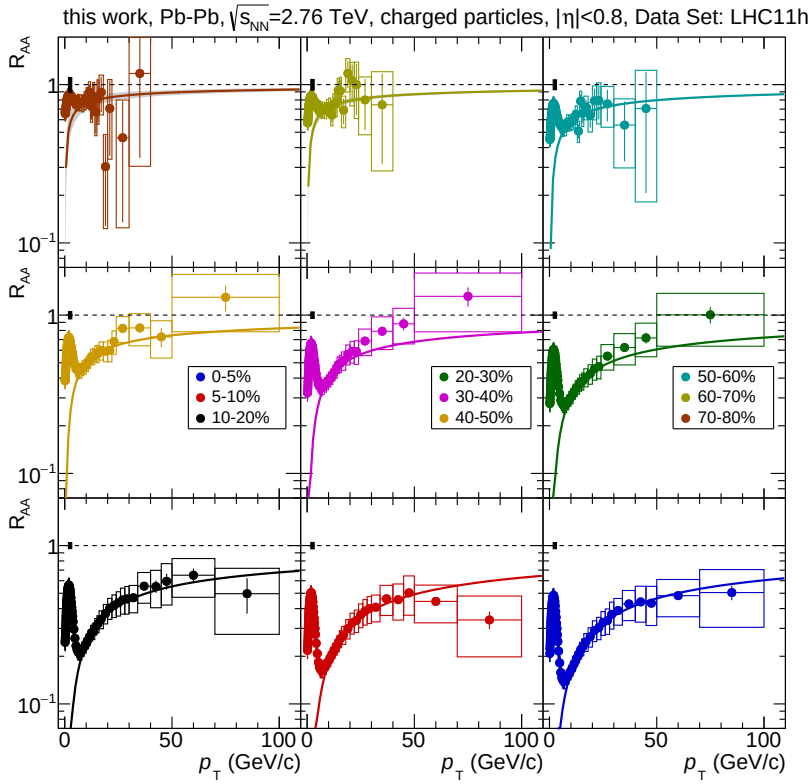

Figure 6.15.: Inclusive Nuclear Modification Factor as function of p_{T} for nine different centrality intervals for inclusive charged particles in Pb–Pb collisions at $\sqrt{s_{NN}} = 2.76$ TeV. The lines show a fit with param. 6.10 for 10 GeV/c < p_{T} < 50 GeV/c, the gray band shows the systematic uncertainty of the parametrization.

the path-length, which is used as input for the model. The parametrizations are in agreement with the measured data within systematic uncertainties in the parametrized p_{T}-range of 10 GeV/c < p_{T} < 50 GeV/c. At p_{T} > 50 GeV/c, the agreement between the parametrizations and the measured data is weaker.

The azimuthal angular dependence relative to the event-plane angle presented in Fig. 6.14 can now be studied in more details in a finer differentiation of the azimuthal angle ϕ of the produced particle relative to the angle of the event-plane Ψ_2:

$$\Delta\phi = |\phi - \Psi_2| \tag{6.11}$$

This relative angle can be correlated to an average, angle-dependent path-length $\langle L_{\Delta\phi} \rangle$, which here is based on the determination of the distance between the center and the edge in an hypothetical ellipse with the semi-minor and semi-major axis $L_{inplane}$ and $L_{outplane}$. It should be pointed out, that the ellipse here is only an approximation of the almond-shape assumed in the overlap region of the collisions. The average path-length

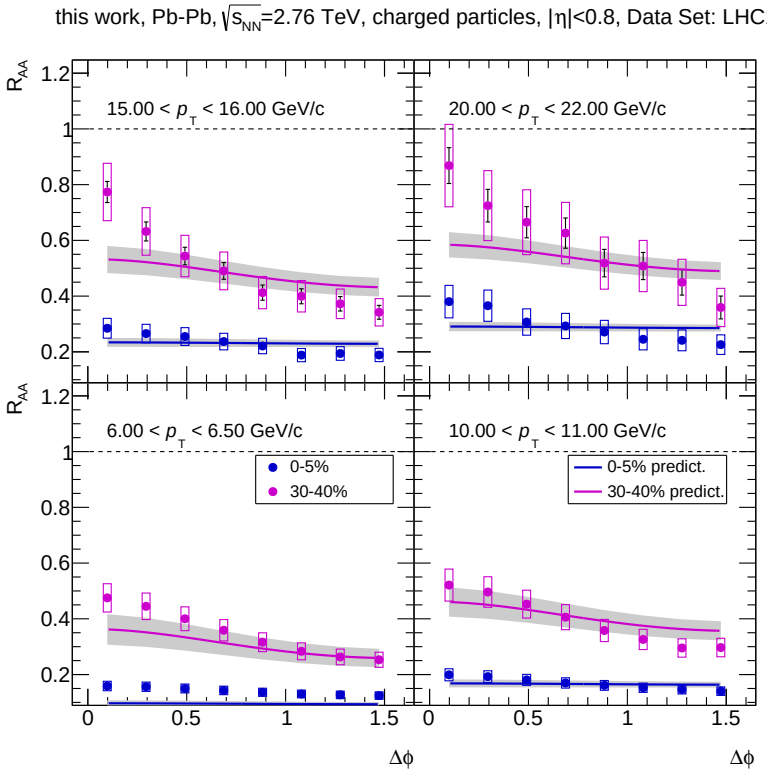

Figure 6.16.: Inclusive Nuclear Modification Factor as function of $\Delta\phi$ for two different centrality intervals for inclusive charged particles in Pb–Pb collisions at $\sqrt{s_{NN}} = 2.76$ TeV. The four different panels show different selections in p_{T} as denoted in each panel. The lines represent a prediction for the $\Delta\phi$ dependence of R_{AA} based on fits of the inclusive R_{AA} with eq. 6.10. The gray band shows the systematic uncertainty of the parametrization (see text for details).

$\langle L_{\Delta\phi} \rangle$ is calculated as:

$$\langle L_{\Delta\phi} \rangle = \sqrt{L_{inplane} \cdot \cos^2(\Delta\phi) + L_{outplane} \cdot \sin^2(\Delta\phi)} \tag{6.12}$$

$L_{inplane}$ and $L_{outplane}$ are obtained from the same Glauber MC as the angular independent path-length used in Fig. 6.15. This average path-length as well as α_s and $\hat{q}$ determined from the parametrizations of the inclusive R_{AA} shown in Fig. 6.15 serve as input for a prediction of R_{AA} as function of $\Delta\phi$ for a fixed p_{T} and centrality according to eq. 6.10. The comparison between the prediction and the measured data is shown in Fig. 6.16 for two different centrality intervals (different colors) and four different p_{T}-selections (different panels). The lines represent the model prediction. The gray band in Fig. 6.16 shows the combined systematic uncertainty of the prediction. This is a combination of the systematic uncertainty of the inclusive parametrization and a variation of $L_{inplane}$

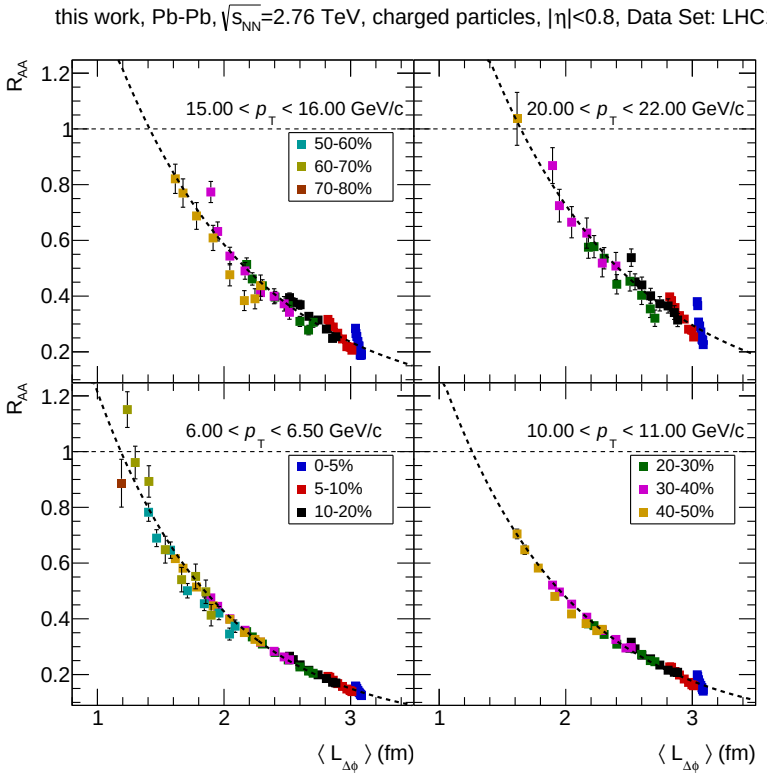

Figure 6.17.: Inclusive Nuclear Modification Factor as function of the path-length through the medium for different centrality intervals for inclusive charged particles. The four different panels show different selections in p_{T} as denoted in each panel. Points with statistical uncertainties larger 10% have been removed from the plot for clarity, also no systematic uncertainties are shown. The dashed line shows a common fit with eq. 6.13 to all data-points.

and $L_{outplane}$ within their uncertainties.

For low p_{T} (lower left panel) the model does not describe the data for central events, which can be explained as the model input from the inclusive R_{AA} has been parametrized for $p_{\mathrm{T}} > 10$ GeV/c only. For semi-central events, the model agrees with the data within systematic uncertainties. For higher p_{T} (other three panels) the model shows a similar angular dependence, which is weaker than measured in the data. A possible explanation might be the fact, that the model describes only the energy loss of partons in the medium. A potential contribution from elliptic flow (compare [54] too) would be largest for in-plane angles ($\Delta\phi = 0$). This flow contribution could give an additional boost to the in-plane particles, which are less suppressed than out-of-plane particles, where the path-length through the medium is larger than in-plane. For the out-of-plane measurement, the energy and momentum conservation might result in a lower R_{AA} compared to the model, as an elliptic flow could give a negative boost here.

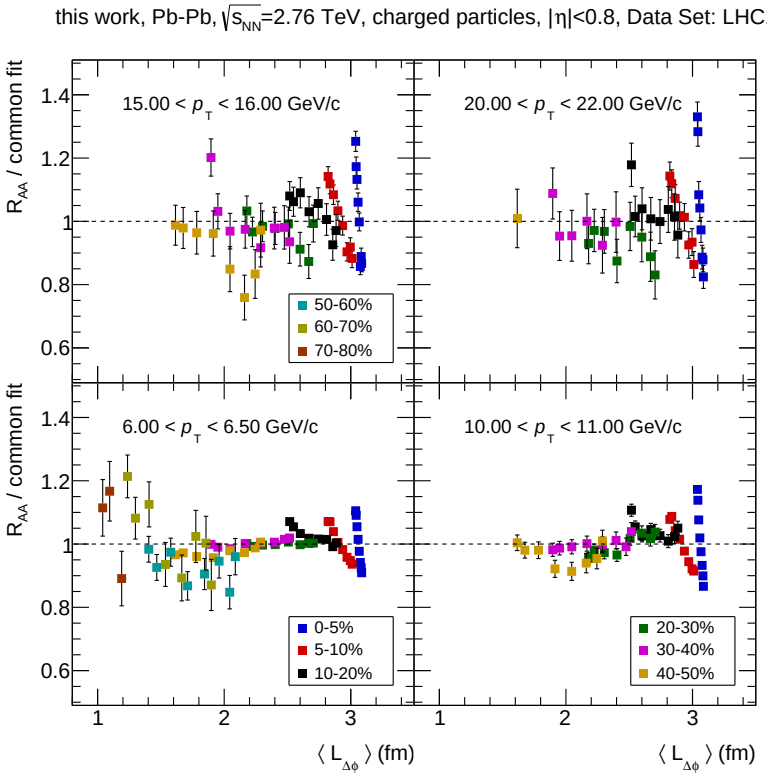

Figure 6.18.: Ratio between the inclusive nuclear modification factor and a common fit to all data-points as function of the length through the medium for different centrality intervals for inclusive charged particles. The four different panels show different selections in p_{T} as denoted in each panel. Points with statistical uncertainties larger 10% have been removed from the plot for better visibility, also no systematic uncertainties are shown.

Fig. 6.17 shows R_{AA} as function of the average path-length $\langle L_{\Delta\phi}\rangle$ for four different p_{T}-intervals (different panels) and nine different centrality intervals (different markers). In this plot, data-points with statistical uncertainties larger 10% have been removed for clarity. Overall, R_{AA} is independent of the collision centrality for the p_{T}-selections shown. This can be explained, as the suppression of particle production should depend to first order on the path-length the particles have traversed in the medium. To study the centrality dependence in more detail, the measured data points are compared to a common parametrization based on the model discussed above (compare eq. 6.10):

$$R_{\mathrm{AA}}\left(\langle L_{\Delta\phi}\rangle\right) = a \cdot \exp(b \cdot \langle L_{\Delta\phi}\rangle) \tag{6.13}$$

The parametrizations are shown in Fig. 6.17 for the four different p_{T}-selections as dashed lines. The ratios between the data-points and the corresponding parametrizations are

shown in Fig. 6.18 as function of the average path-length. Although a general agreement with the parametrization is found, in each centrality a clear deviation of the data points from the parametrization is observed. Clear structures are visible, especially for the most central events. This can be explained by the different shapes of the overlap regions for each centrality. For central collisions, the circle-shaped overlap region results in a weak angular dependence of the path-length, while for semi-central and peripheral collisions the almond-shaped overlap region results in a stronger angular dependence of the path-length (compare Fig. 4.3). Therefore, the data points for central events cluster at similar path-lengths, while the spread in R_{AA} is significantly larger for semi-central events. Going to more peripheral collisions, the angular dependence of the path-length increases together with a larger spread in R_{AA} (compare Fig. 6.17). Nevertheless in peripheral collisions, the large spread in R_{AA} and path-length results in a better agreement with the common fit (compare Fig. 6.18).
The path-length dependence of the π^0 R_{AA} in Au–Au collisions at $\sqrt{s_{NN}} = 200$ GeV as presented in [54] shows that the suppression vanishes, i.e. $R_{\mathrm{AA}} = 1$, for a path-length $L \approx 2$ fm. The data presented in Fig. 6.17, however, shows a vanishing of the charged particle suppression for slightly lower path-lengths of $L \approx 1.4$ fm instead of $L \approx 2$ fm; this difference in L might be related to different collision systems or collision energies. The slight p_{T}-dependence of the path-lengths, where $R_{\mathrm{AA}} = 1$ is small and allows for no clear conclusion. As suggested in [54], a possible independence of the path-length from p_{T} can be related to surface emission: this takes into account, that the suppression of the particle production depends on the production vertex in the medium; particles produced closed to the surface are suppressed less, as they only traverse a short path-length in the medium. The shortest path-lengths are reached for peripheral collisions for particles produced in-plane (compare Fig. 6.12). This difference is often referred to as a so-called *surface bias* (compare [56, 57, 58]). The statistics of the data set from the data taking period LHC11h allows for no conclusion on this effect at the moment, but lays the basis for upcoming analyses with higher statistics and at higher center-of-mass energies.

The analyses of charged particle production measured in Pb–Pb collisions at $\sqrt{s_{NN}} = 2.76$ TeV presented in this chapter, i.e. the extension of R_{AA} to $p_{\mathrm{T}} = 100$ GeV, the p_{T}- and centrality-dependence of S_{loss} as well as the path-length dependence of R_{AA}, can help to constrain current energy loss models. Together with the analyses of the p_{T}-spectra of charged particles measured in the data sets at higher collision energies, detailed studies of these models are possible and can help to better understand the particle production and suppression mechanisms in the QGP.

Chapter 7.

Summary and Outlook

This work focuses on a study of the basic properties of matter; in particular, on properties of the Quark Gluon Plasma (QGP) created in Pb–Pb collisions at $\sqrt{s_{NN}} = 2.76$ TeV and investigated by ALICE at the LHC. The analysis concentrates on the production of primary charged particles and their transverse momentum (p_{T}) dependence, where the particle production in Pb–Pb collisions is compared to the particle production in pp collisions. Furthermore, the particle production in Pb–Pb collisions with respect to the event-plane of the collision is investigated.

The protons and Pb-ions are brought to collision in the center of the ALICE experiment at the CERN-LHC. ALICE assembles a variety of detectors with different detection techniques. In this work, charged particles are measured with the Time Projection Chamber and the Inner Tracking System in the central barrel of ALICE. Together, they provide tracking of charged particles produced in the collision up to $p_{\mathrm{T}} = 100$ GeV/c.

For Pb–Pb collisions, here, data from the data taking periods LHC10h and LHC11h is analyzed. The data is reconstructed from the detector hits to build tracks. These tracks are prefiltered into so-called AODs to reduce the data size and to improve the analysis speed. Characteristic event properties such as the centrality or the event-plane of the event are determined commonly elsewhere to be identical in all analyses in the ALICE collaboration. Tracks are selected for the analysis with various track cuts. In this work, a new track cut, i.e. a cut on the active length in the TPC, has been applied. This purely geometrical cut shows good agreement between data and MC, which is needed to extract three different tracking corrections. At first, the efficiency and acceptance to measure charged particles in the detector are corrected. This corrects for inefficiencies in the detector setup as well as the limited acceptance of the detectors. At second, a correction removes the contamination of secondary particles in the track sample. At third, the p_{T} of each track is corrected for the p_{T} resolution. Here, a data-driven approach is used to

extract this correction, which is particularly needed at high p_{T}.
Particle production in pp collisions at high collision energies can be categorized into two different types based on the p_{T} of the produced particles. At low p_{T}, so-called *soft processes* play the most important role and dominate the total cross-section of particle production, while at high p_{T}, the so-called *hard processes* rule the particle production. At low p_{T}, mainly phenomenological models can describe the particle production, as the momentum transfer between the colliding partons is small. At high p_{T}, particle production is described by models based on perturbative QCD. In these models, the total cross-section at high p_{T} is usually split into three different parts which are all independent, usually referred to as factorization: the parton distribution function (PDF), the cross-section of an elementary reaction and the fragmentation function.
In this work, the p_{T} spectra of charged particles measured in pp collisions at three different collision energies of $\sqrt{s} = 0.9$, 2.76 and 7 TeV show a clear collision energy dependence, namely a flattening of the p_{T} spectra for higher collision energies. Furthermore, the spectra are compared to a prediction by an NLO-pQCD calculation [1, 2]. An overprediction of the model by roughly a factor of two is observed. The collision energy dependence of the charged particle production at different energies is further compared in terms of the so-called x_{T}-scaling, where it is assumed, that the particle production depends on the ratio of p_{T} and the collision energy. The comparison shows good agreement between all three energies for $x_{\mathrm{T}} \geq 0.006$.
Particle production in Pb–Pb collisions is more than a simple superposition of the particle production in pp collisions scaled with the number of binary collisions. Due to the creation of the QGP, collective effects as well as energy loss mechanisms modify the particle yield. Furthermore, the PDF itself is modified in comparison to pp collisions. Various signatures have been suggested to study the properties of the QGP. Of special interest in this work is the suppression of the particle yield caused by the energy loss of partons in the medium. Usually, this is studied in terms of the nuclear modification factor R_{AA}, i.e. the ratio of the particle yield in Pb–Pb collisions and the particle yield in pp collisions scaled by the number of binary collisions. For $R_{\mathrm{AA}} = 1$, no suppression of the particle production in Pb–Pb collisions is observed. The p_{T} dependence of R_{AA} can then give insight into the energy loss dependence on the p_{T} of the particle.
In this work, a study of charged particle production in Pb–Pb collisions at $\sqrt{s_{NN}} = 2.76$ TeV based on a re-analysis of the data set from the data taking period LHC10h is presented. The p_{T} spectra show a clear centrality dependence, especially in comparison to a scaled pp reference spectrum. In central collisions the particle production in Pb–Pb collisions is suppressed compared to the reference spectrum, while the p_{T} spectra in

pp and Pb–Pb agree better for more peripheral collisions. The re-analysis in this work confirms already published results [3] based on the same data set. In contrast to [3], the re-analysis is carried out with a new analysis code facilitating the use of AODs for the first time for the analysis of the p_{T} spectra of charged particles. This confirmation legitimates the use of the newly developed analysis task in this work for the analysis of charged particles based on the data set from the data taking period LHC11h, which is original to this work. The inclusion of the centrality triggers for central and semi-central events in this data set increases the p_{T} reach by a factor of two from $p_{\mathrm{T}} = 50$ GeV/c to $p_{\mathrm{T}} = 100$ GeV/c. Furthermore, the statistical uncertainty for $p_{\mathrm{T}} < 50$ GeV/c is reduced by a factor of two. This high p_{T} regime, which is now accessible by this work, and smaller statistical uncertainties can help to better constrain the energy loss in model calculations.

To complement the measurements at high p_{T}, the charged particle production at low p_{T} is characterized by the average transverse momentum $\langle p_{\mathrm{T}} \rangle$. The multiplicity dependence of $\langle p_{\mathrm{T}} \rangle$ is compared for pp collisions at three different collision energies of $\sqrt{s} = 0.9$, 2.76 and 7 TeV. Only a small collision energy dependence is observed. The dependence of $\langle p_{\mathrm{T}} \rangle$ on the collision system is studied for pp, p–Pb and Pb–Pb collisions. A strong difference between the three collision systems is observed: in pp collisions $\langle p_{\mathrm{T}} \rangle$ rises strongly with multiplicity. In Pb–Pb collisions, $\langle p_{\mathrm{T}} \rangle$ increases for low multiplicities and flattens at higher multiplicities. p–Pb collisions show features of both, pp and Pb–Pb collisions: a strong rise for low multiplicities and a plateau at a higher multiplicities. The onset of the plateau in p–Pb collisions is observed at higher $\langle p_{\mathrm{T}} \rangle$ than in Pb–Pb collisions.

The p_{T} spectra of charged particles measured in Pb–Pb collisions are compared to a scaled pp reference spectrum in terms of R_{AA}. For the construction of the pp reference spectrum, various methods are developed and presented in this work. In case no pp collisions have been measured at the same collision energy as of the Pb–Pb collisions, either NLO-pQCD calculations are facilitated to scale the measured data at higher resp. lower collision energies or an interpolation procedure between measurements at two available collision energies is used. The final reference spectrum for R_{AA} based on the data set from the data taking period LHC11h is constructed from the measured pp p_{T} spectrum at $\sqrt{s} = 2.76$ TeV. To increase the p_{T} range of the reference spectrum up to $p_{\mathrm{T}} = 100$ GeV/c, i.e. the p_{T} reach measured in central Pb–Pb collisions in the data set of the data taking period LHC11h, the measured pp p_{T} spectrum is parametrized with a so-called modified Hagedorn function; the parametrization is then extrapolated up to $p_{\mathrm{T}} = 100$ GeV/c. The resulting R_{AA} is below unity for all centrality selections. For 0 - 5 % central collisions, R_{AA} shows a minimum of $R_{\mathrm{AA}} \approx 0.2$ at $p_{\mathrm{T}} = 6 - 7$ GeV/c

and rises with higher p_{T}. For $p_{\mathrm{T}} > 40$ GeV/c R_{AA} seems to reach a plateau in central collisions covering the newly accessible p_{T} range. The so-called punch-through of particles cannot be excluded within the systematic uncertainties, however. In 70 - 80 % peripheral collisions, R_{AA} only weakly depends on p_{T} with $R_{\mathrm{AA}} \approx 0.8$.
In addition to the study of the suppression of the particle production caused by energy loss of partons in the QGP, the study of the relative energy loss of partons in the medium can help to constrain the energy loss mechanisms even further. Here, the relative transverse momentum loss S_{loss} is used as an approximation of the relative energy loss of the partons following [5]. For central collisions, S_{loss} decreases with p_{T}, matching the observation that R_{AA} increases with p_{T}. For peripheral collisions, nearly no p_{T} dependence of S_{loss} is observed. Furthermore, the centrality dependence of S_{loss} is studied for fixed selections in p_{T}. For all p_{T} selections, S_{loss} increases towards more central collisions. Within each centrality class, S_{loss} decreases with higher p_{T}. S_{loss} as function of centrality for fixed p_{T} is proportional to $N_{part}^{2/3}$ as suggested by [6].
As an alternative approach to constrain the energy loss and especially its path-length dependence in the medium the dependence of R_{AA} on the azimuthal angle relative to the event-plane $\Delta\phi$ of the collision is studied. A clear dependence of R_{AA} on $\Delta\phi$ is observed: for particles produced out-of-plane R_{AA} is smaller than for particles produced in-plane. This can be attributed to a different path-length of the particle in the medium. Due to an almond-shaped overlap region of the colliding ions, most prominent in semi-central collisions, the path-length in-plane is smaller than the path-length out-of-plane. The observation is compared to a theoretical model [7] which determines R_{AA} based on the energy loss of quarks and gluons in the medium. To compare the model with the data, the functional model prediction is fit to the inclusive, i.e. event-plane independent, R_{AA} as function of p_{T}. The free parameters of the model α_s and $\hat{q}$ together with the path-length obtained from a Glauber MC are then used to predict the $\Delta\phi$-dependent R_{AA} according to the model. For average values of $\Delta\phi$ this prediction agrees with the measured R_{AA}. The $\Delta\phi$-dependence, however, is less pronounced in the prediction than in data. For very high and very low $\Delta\phi$, the difference between data and prediction might be explained by elliptic flow effects, which affect the data, but are not included in the theoretical model. Furthermore, the $\Delta\phi$-dependence of R_{AA} can be translated to a path-length dependence. Overall, this path-length dependence shows no dependence of R_{AA} on the centrality. This can be understood, as the suppression should to first order depend on the path-length of the particles in the medium.

To conclude: the measurement of R_{AA} in Pb–Pb collisions at $\sqrt{s_{NN}} = 2.76$ TeV at high p_{T} together with a detailed study of the angular dependence of R_{AA} relative to the event-plane and the derived path-length dependence of the particles in the medium can help to constrain the theoretical understanding of particle production and suppression mechanisms in the hot and dense medium. Furthermore, energy loss alone seems not to be able to describe the observed path-length dependence of R_{AA} and additional collective effects, e.g. elliptic flow, may need to be included.

An extension of the measured pp spectrum to higher transverse momenta in the future will help to constrain R_{AA} even more and will help to reduce the systematic uncertainties of R_{AA} at high p_{T}, which are currently dominated by the uncertainties of the constructed pp reference spectrum at high p_{T}. In addition to an upgrade of the TPC with an increased read-out speed, trigger based measurements can help to extend the p_{T}-range. A data set including EMCal-triggered events has been recorded already. Currently, the influence of a potential trigger bias on the charged particle spectrum by triggering on electromagnetic probes is under study. A data set including TRD-triggers is planned for the upcoming data taking periods. This trigger has the advantage that potentially no trigger bias is introduced by the detector.
The measurement of Pb–Pb spectra is currently extended to higher collision energies at the LHC. Besides Pb–Pb collisions at $\sqrt{s_{NN}} = 5.02$ TeV, pp and p–Pb collisions at the same center-of-mass energy have been measured. With all three measurements together and a detailed comparison to theory predictions a more complete picture of the creation of matter is on the horizon.

Appendix A.

Complete Analysis Results

A.1. p_{T} Spectra in LHC10h (re-analysis)

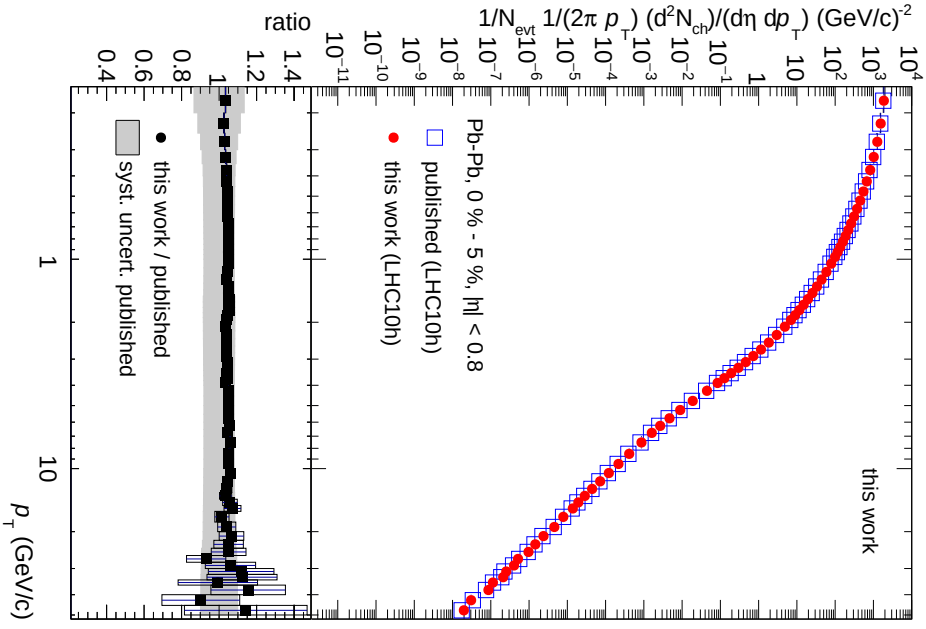

Figure A.1.: LHC10h, 0 - 5 %

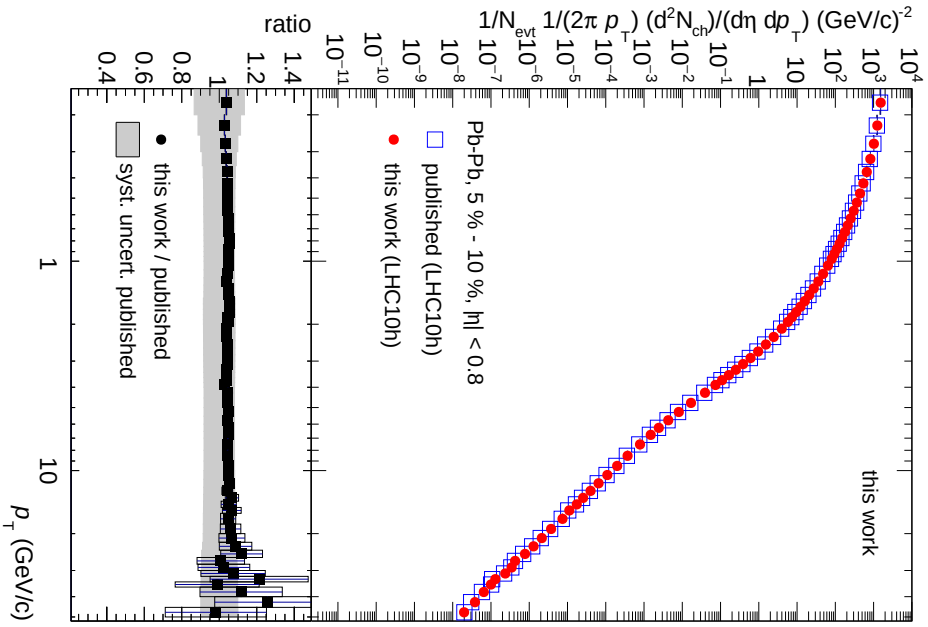

Figure A.2.: LHC10h, 5 - 10 %

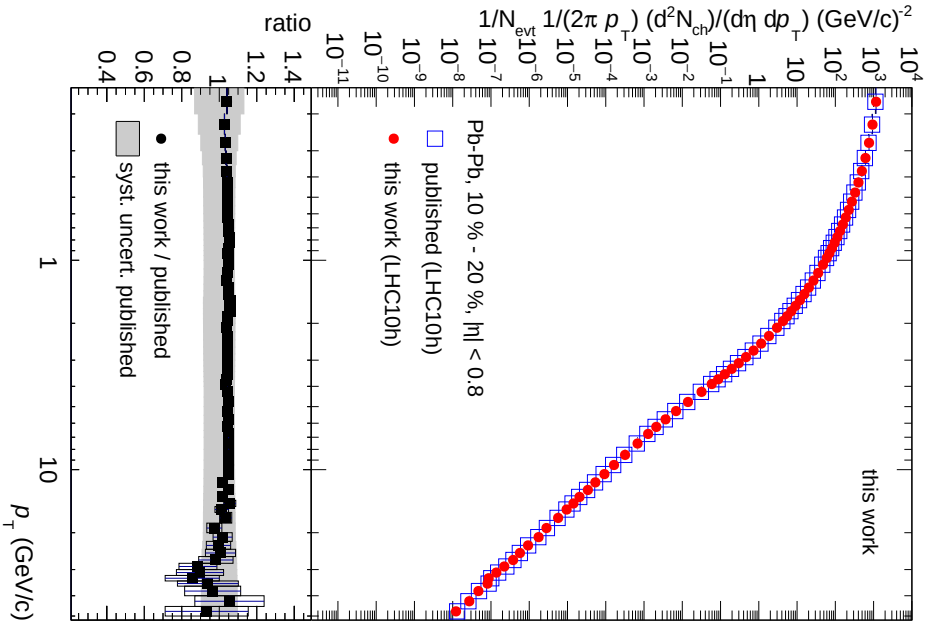

Figure A.3.: LHC10h, 10 - 20 %

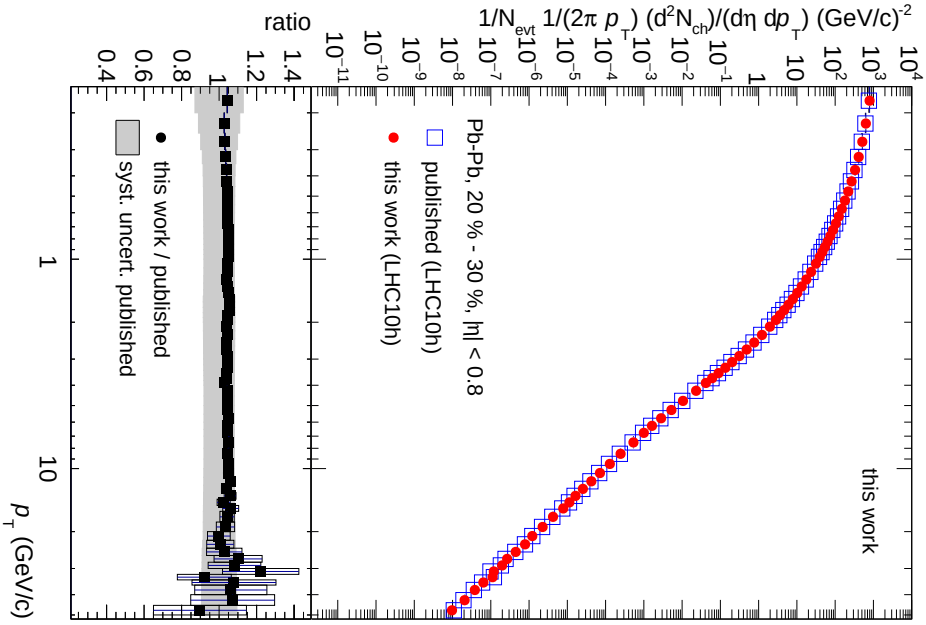

Figure A.4.: LHC10h, 20 - 30 %

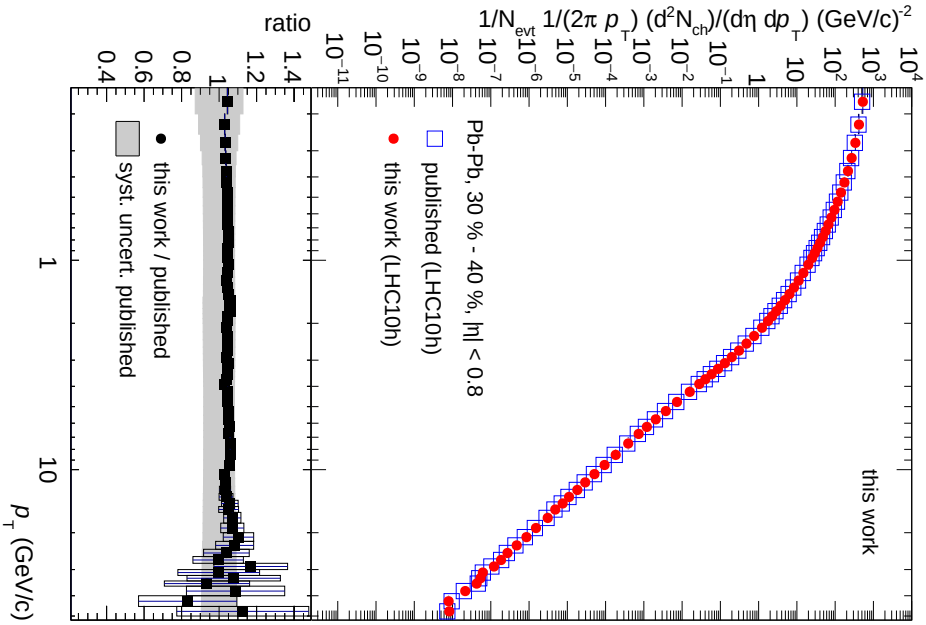

Figure A.5.: LHC10h, 30 - 40 %

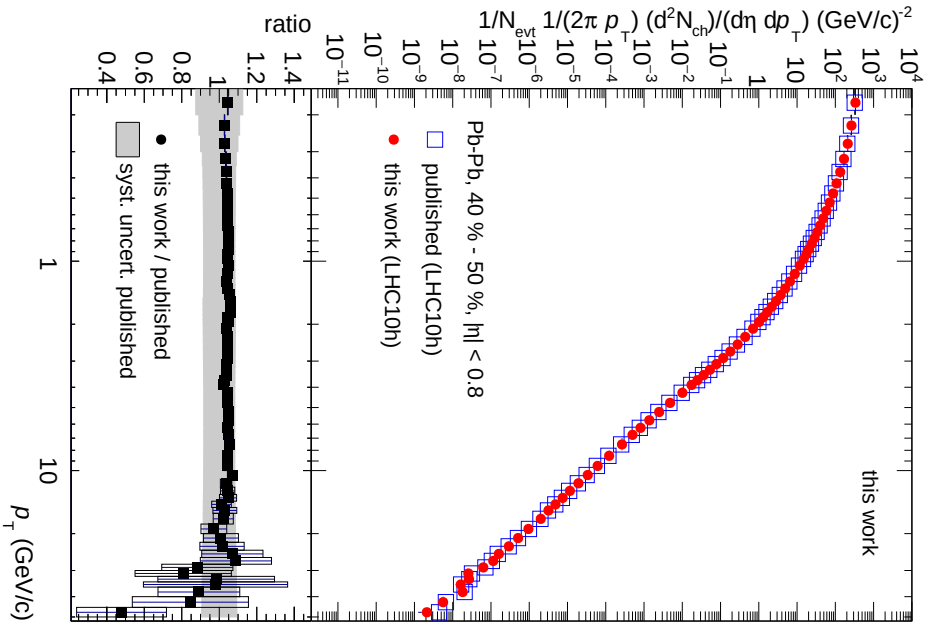

Figure A.6.: LHC10h, 40 - 50 %

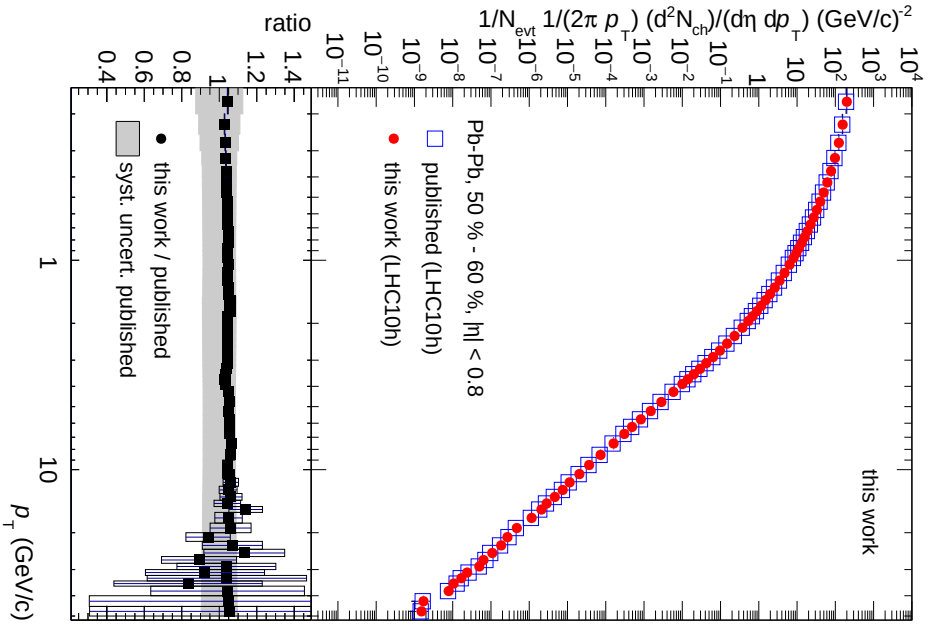

Figure A.7.: LHC10h, 50 - 60 %

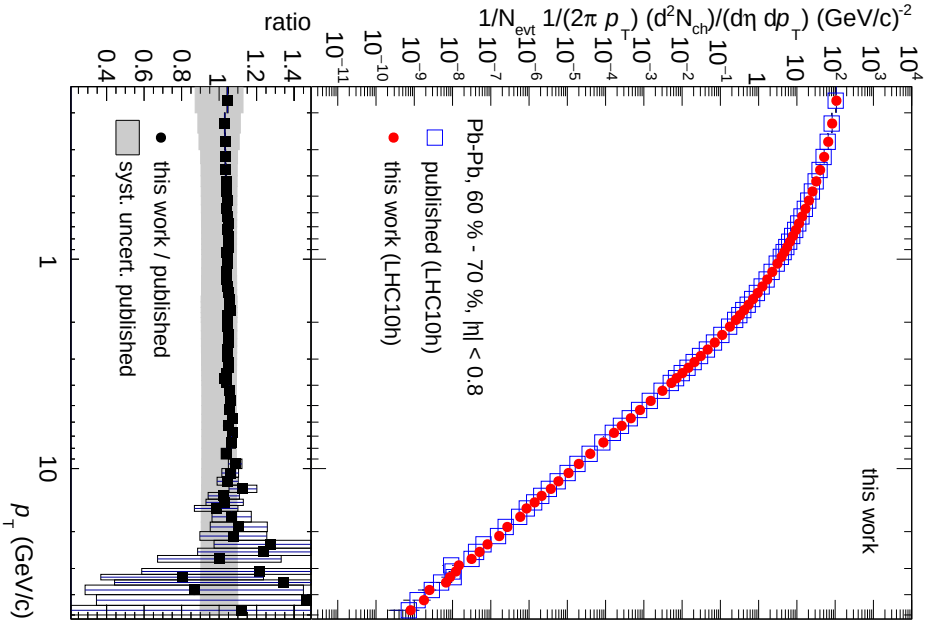

Figure A.8.: LHC10h, 60 - 70 %

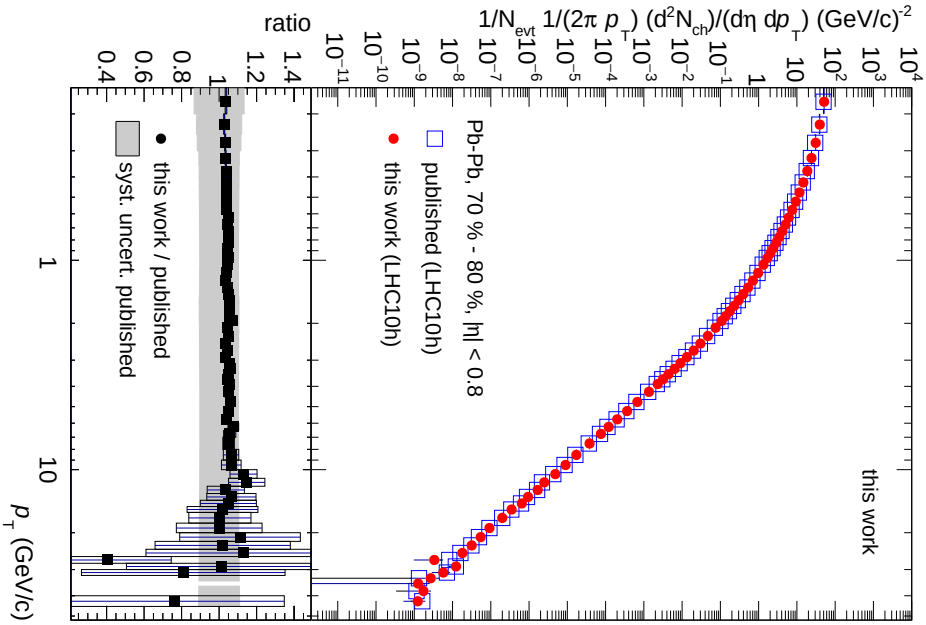

Figure A.9.: LHC10h, 70 - 80 %

A.2. R_{AA} in LHC10h (re-analysis)

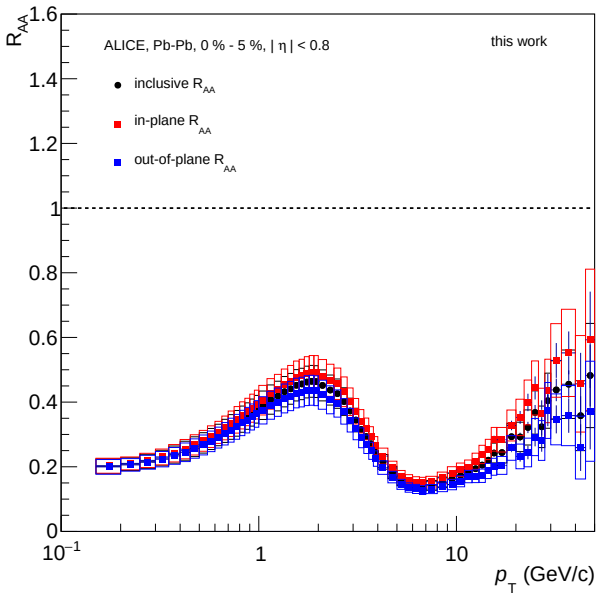

Figure A.10.: LHC10h, 0 - 5 %

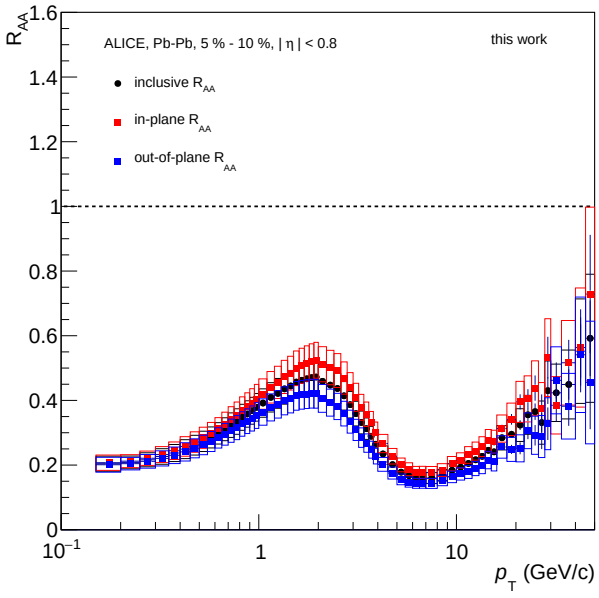

Figure A.11.: LHC10h, 5 - 10 %

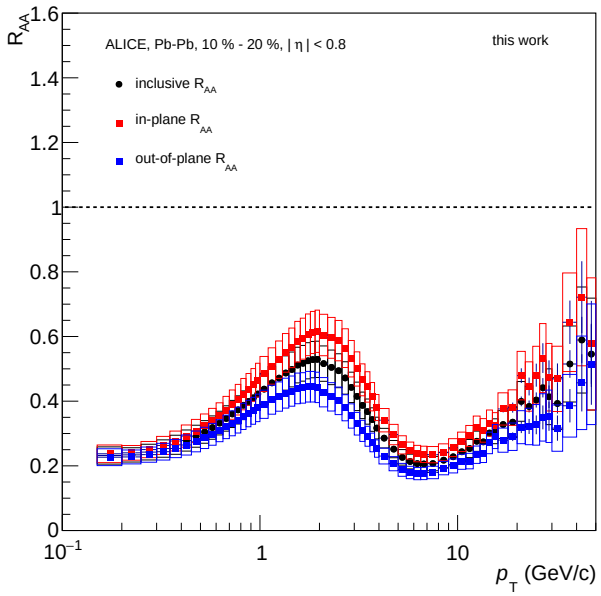

Figure A.12.: LHC10h, 10 - 20 %

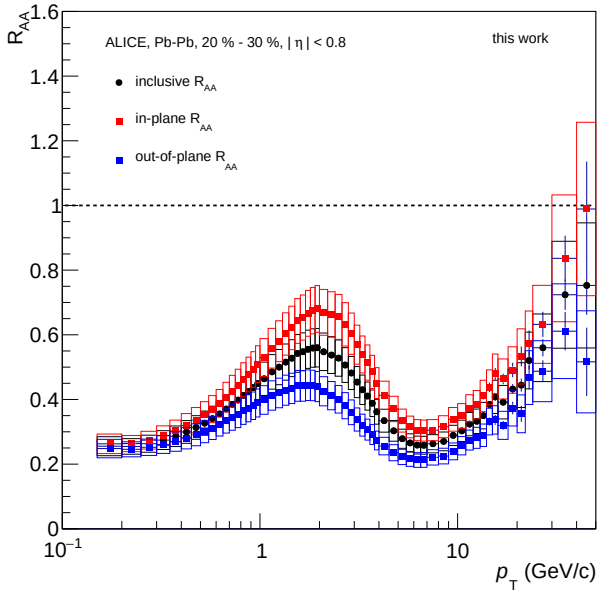

Figure A.13.: LHC10h, 20 - 30 %

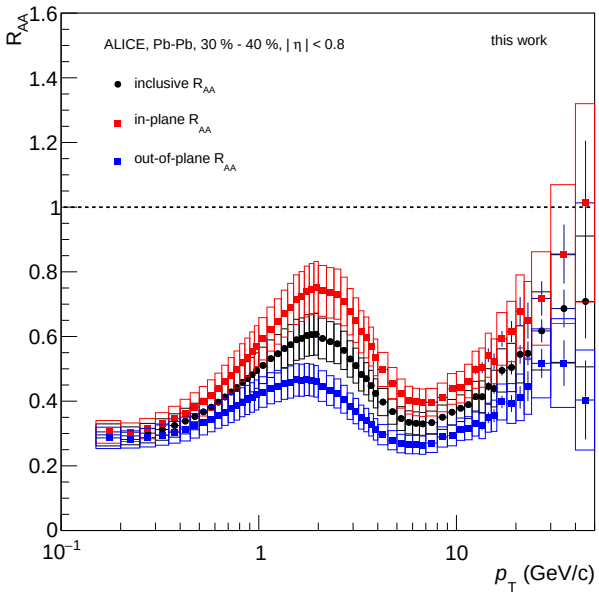

Figure A.14.: LHC10h, 30 - 40 %

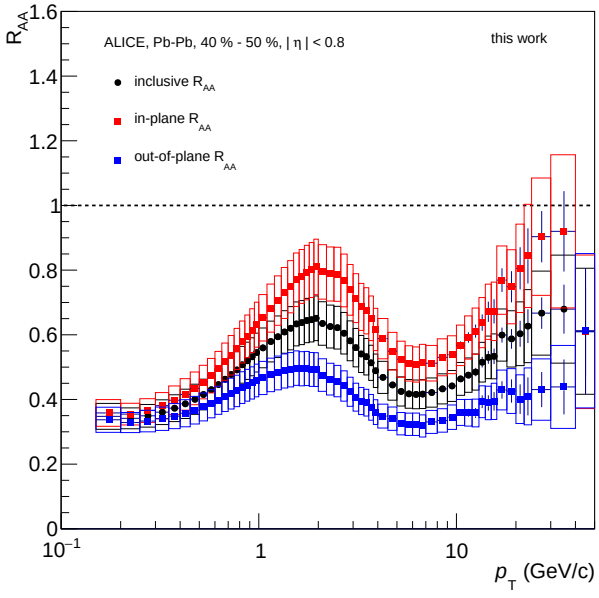

Figure A.15.: LHC10h, 40 - 50 %

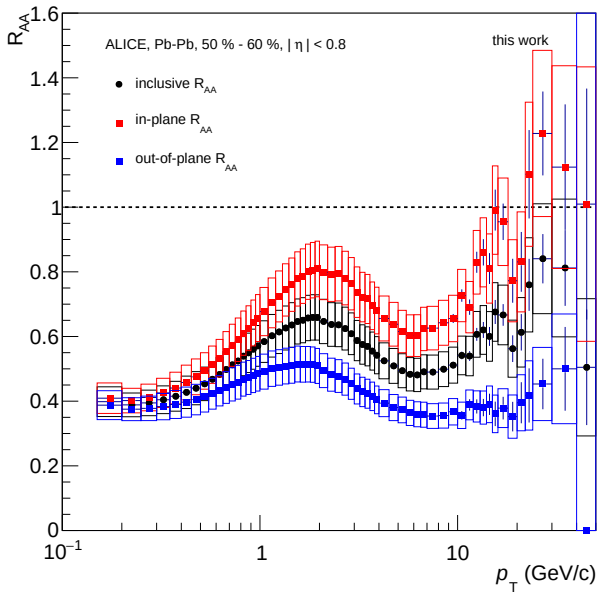

Figure A.16.: LHC10h, 50 - 60 %

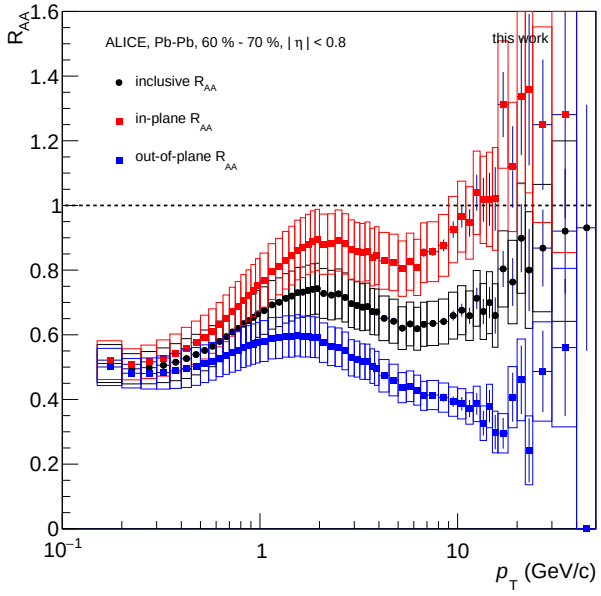

Figure A.17.: LHC10h, 60 - 70 %

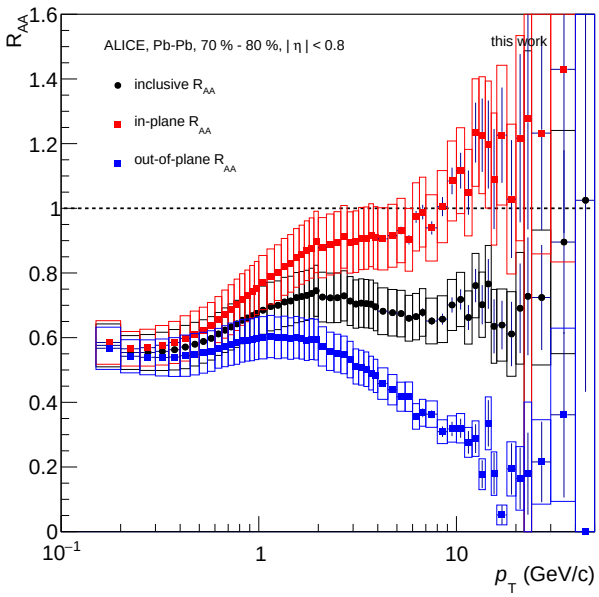

Figure A.18.: LHC10h, 70 - 80 %

A.3. p_{T} Spectra in LHC11h

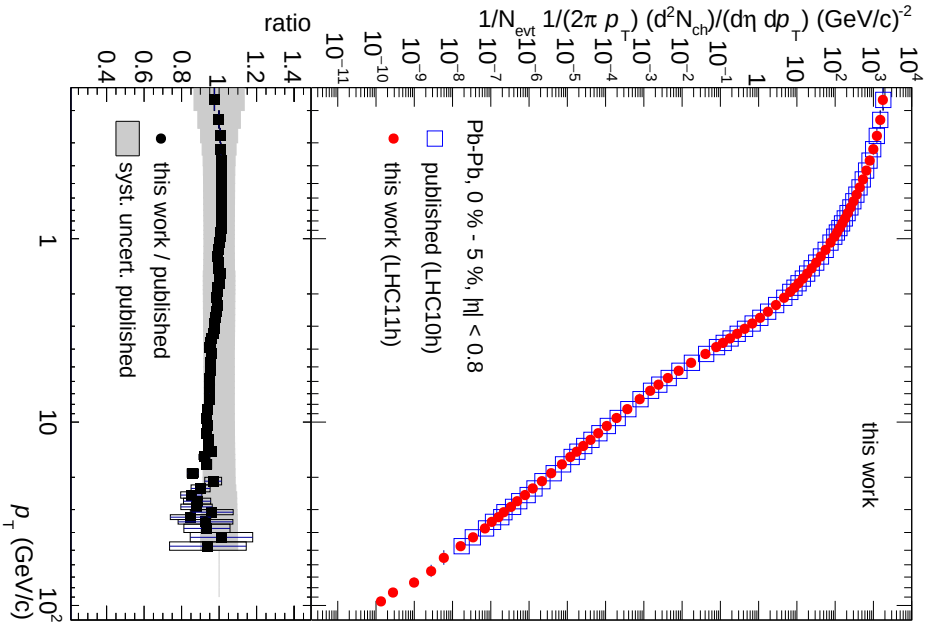

Figure A.19.: LHC11h, 0 - 5 %

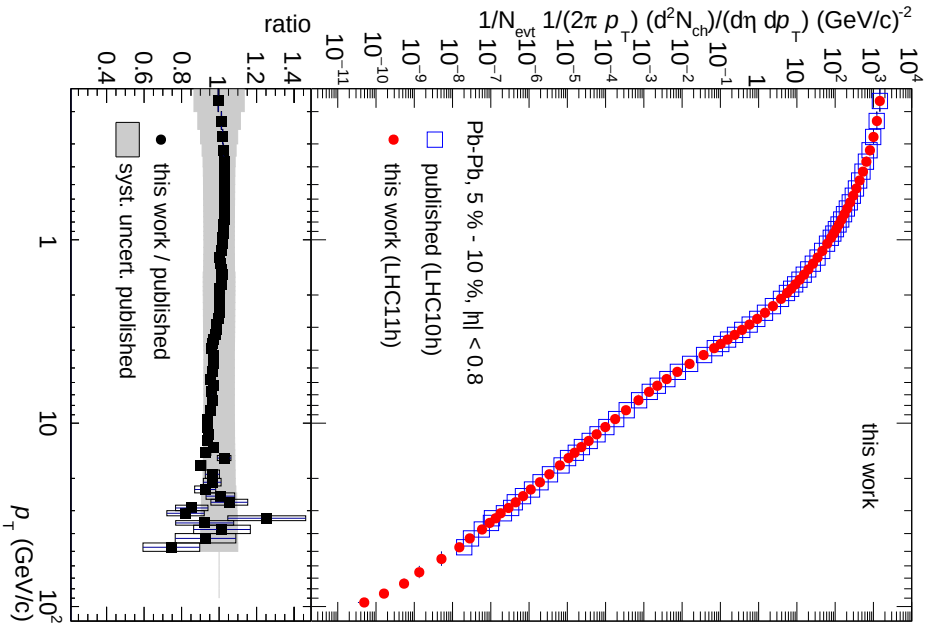

Figure A.20.: LHC11h, 5 - 10 %

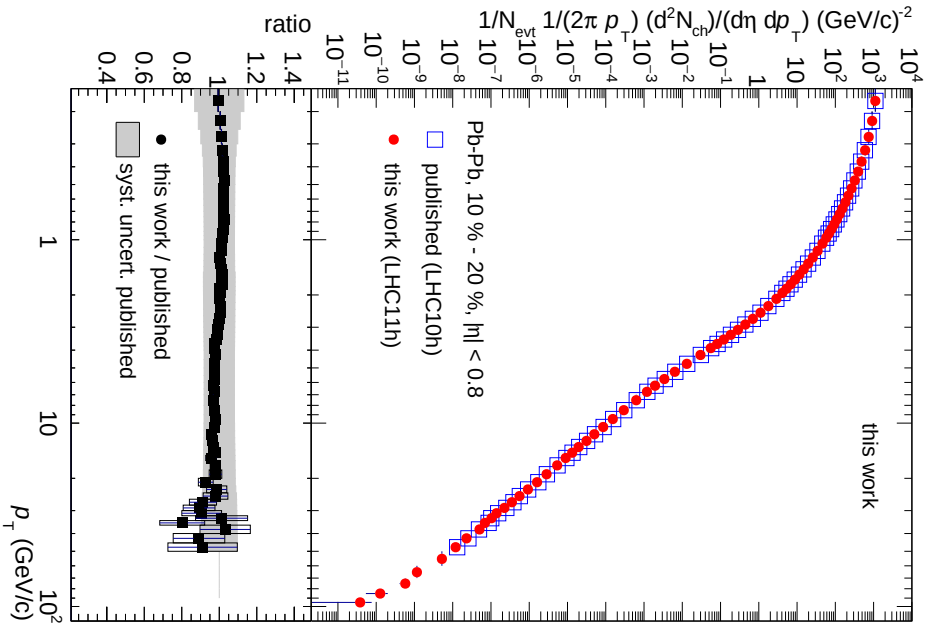

Figure A.21.: LHC11h, 10 - 20 %

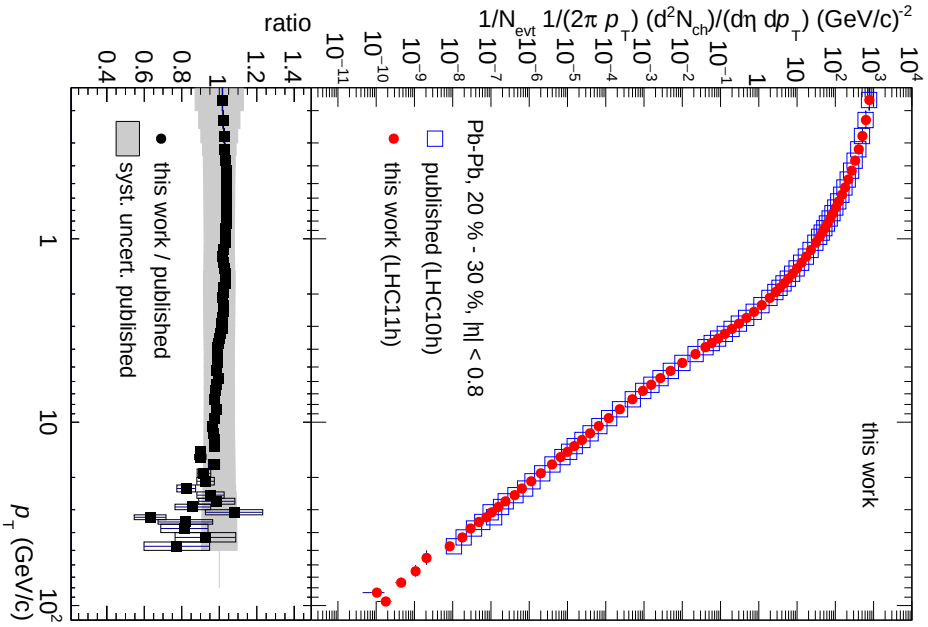

Figure A.22.: LHC11h, 20 - 30 %

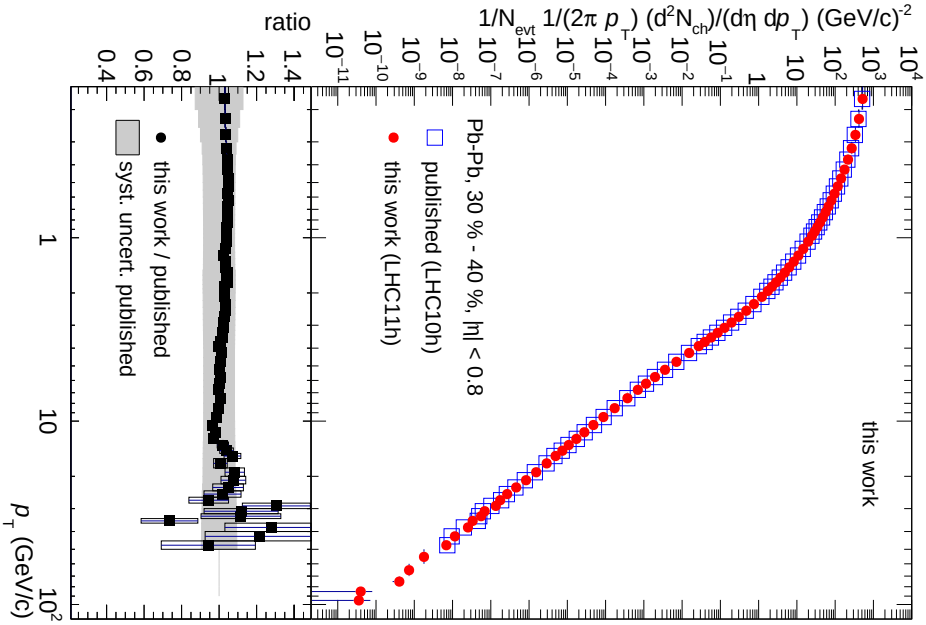

Figure A.23.: LHC11h, 30 - 40 %

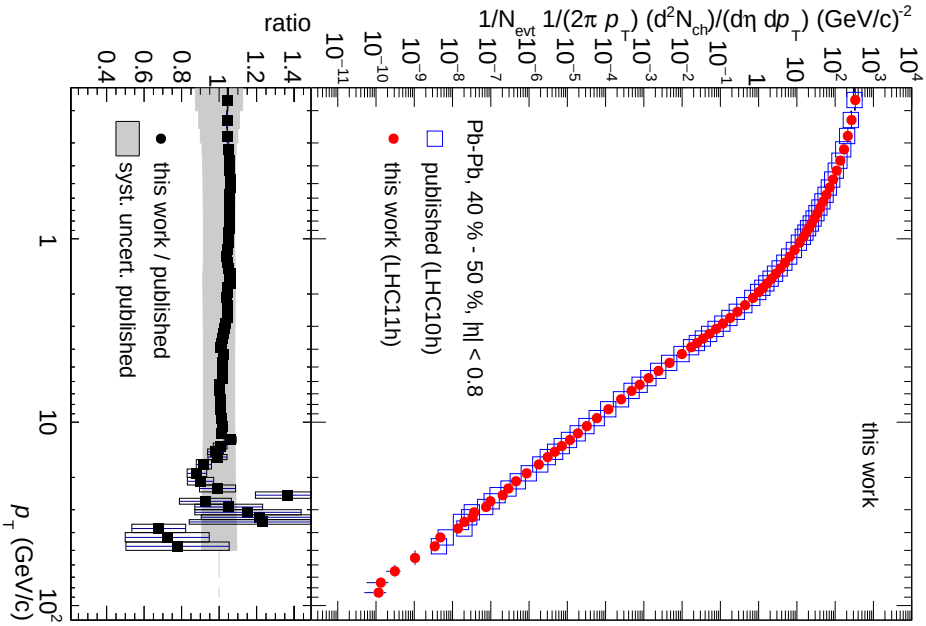

Figure A.24.: LHC11h, 40 - 50 %

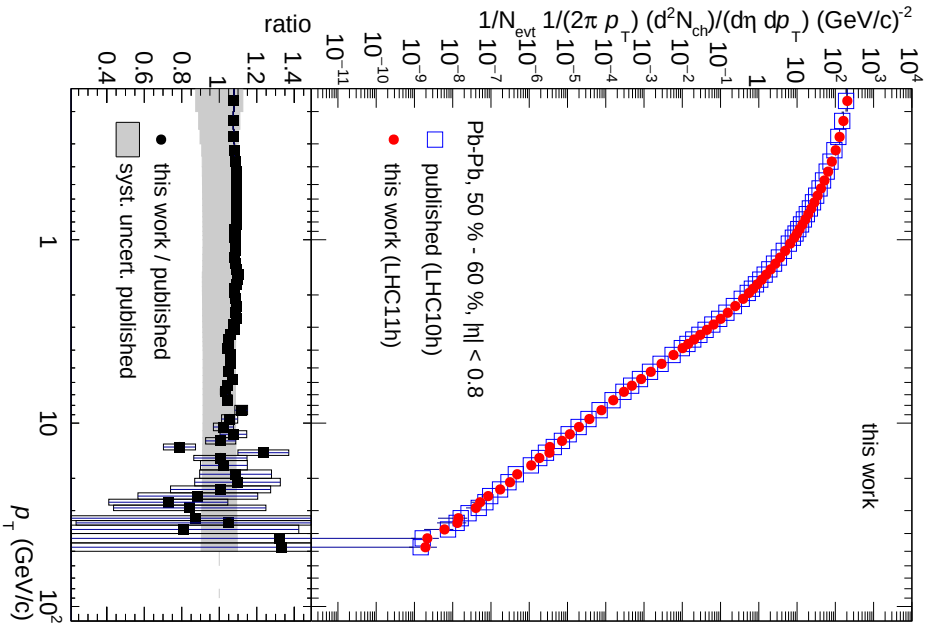

Figure A.25.: LHC11h, 50 - 60 %

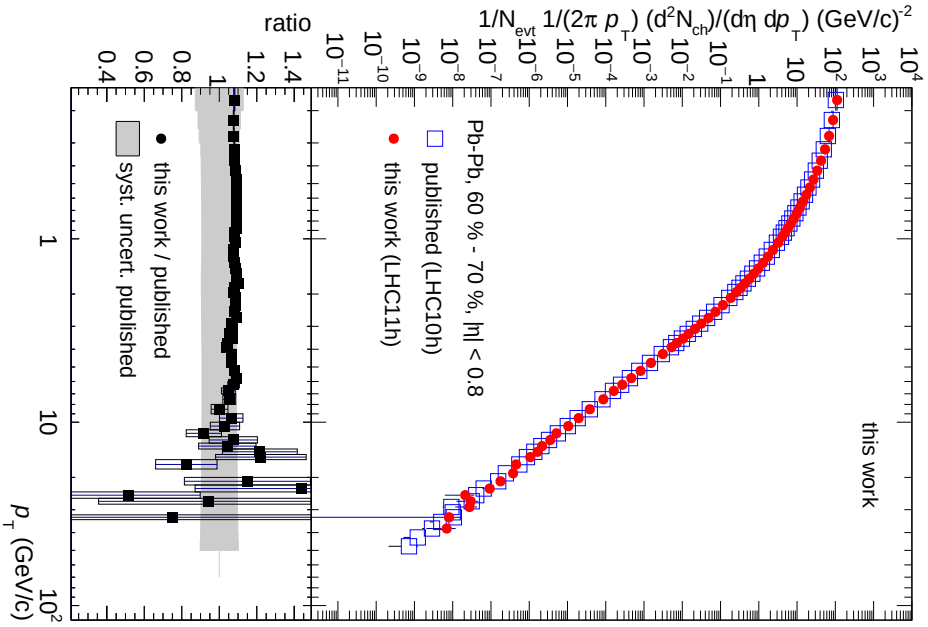

Figure A.26.: LHC11h, 60 - 70 %

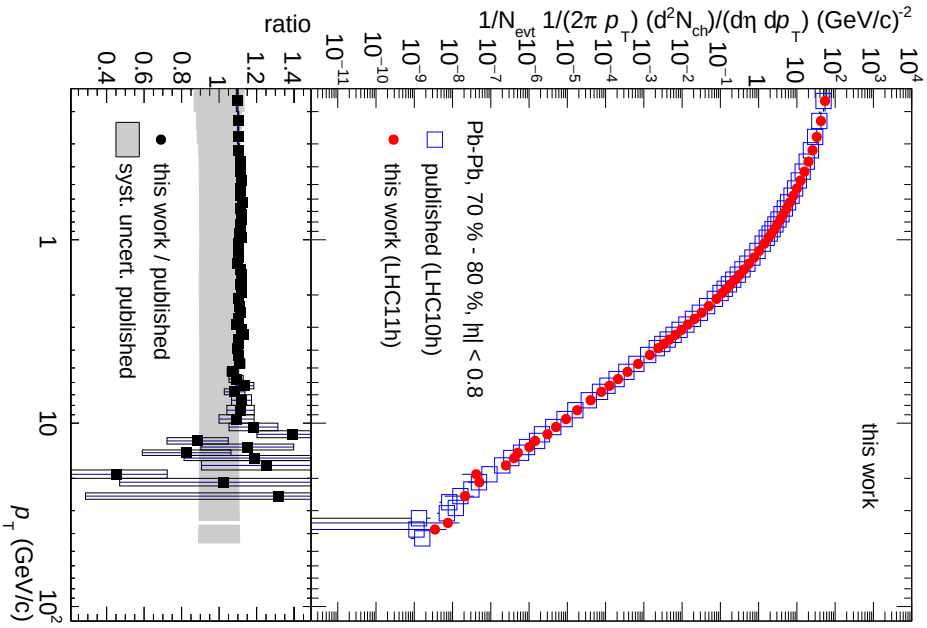

Figure A.27.: LHC11h, 70 - 80 %

A.4. R_{AA} in LHC11h

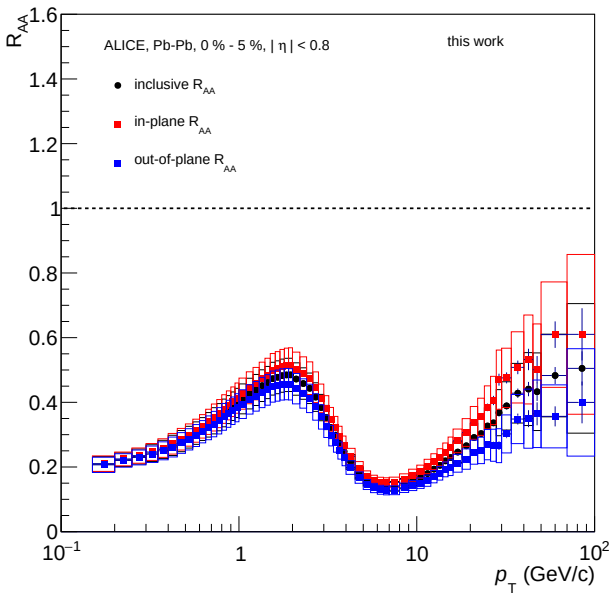

Figure A.28.: LHC11h, 0 - 5 %

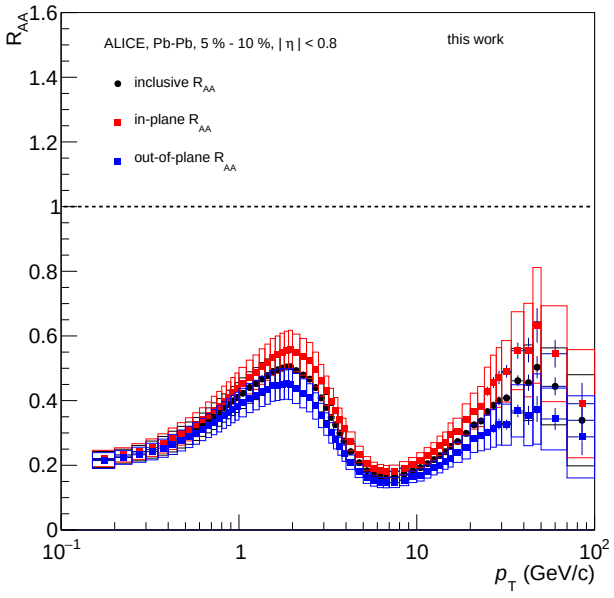

Figure A.29.: LHC11h, 5 - 10 %

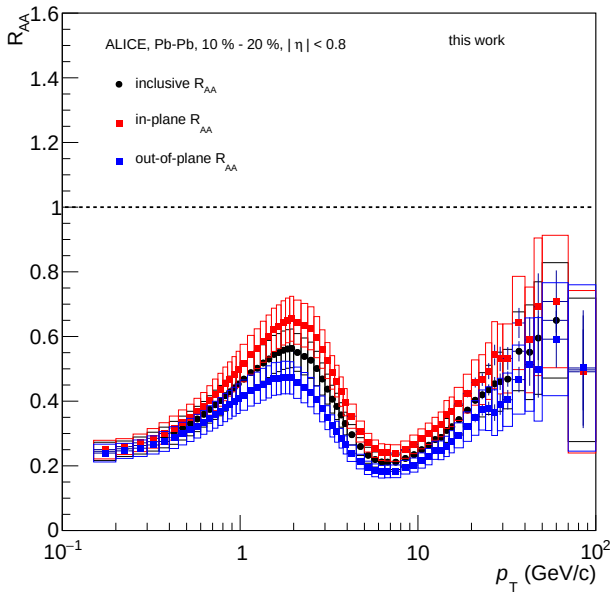

Figure A.30.: LHC11h, 10 - 20 %

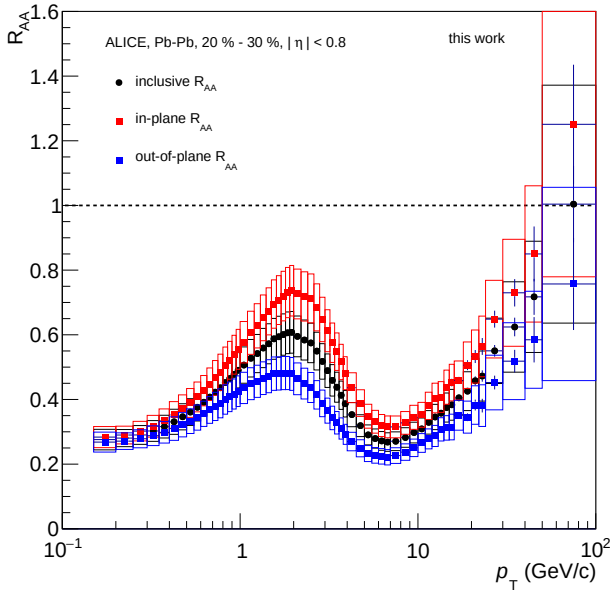

Figure A.31.: LHC11h, 20 - 30 %

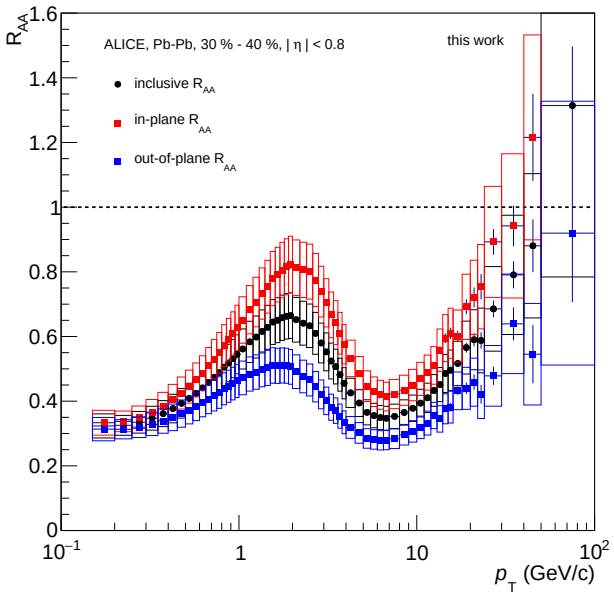

Figure A.32.: LHC11h, 30 - 40 %

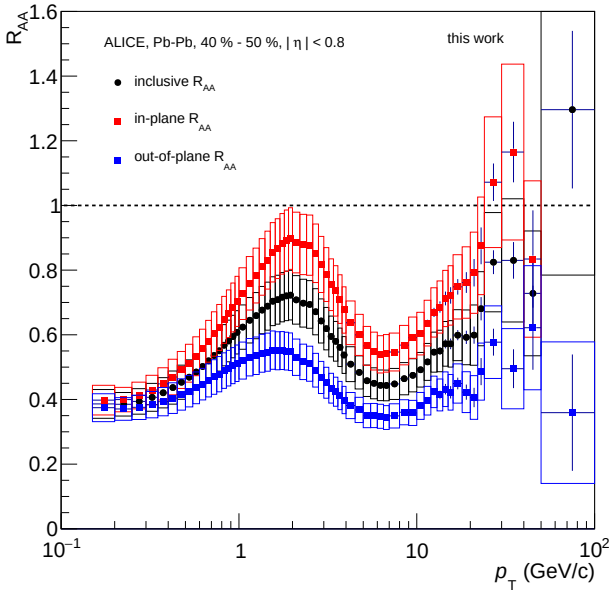

Figure A.33.: LHC11h, 40 - 50 %

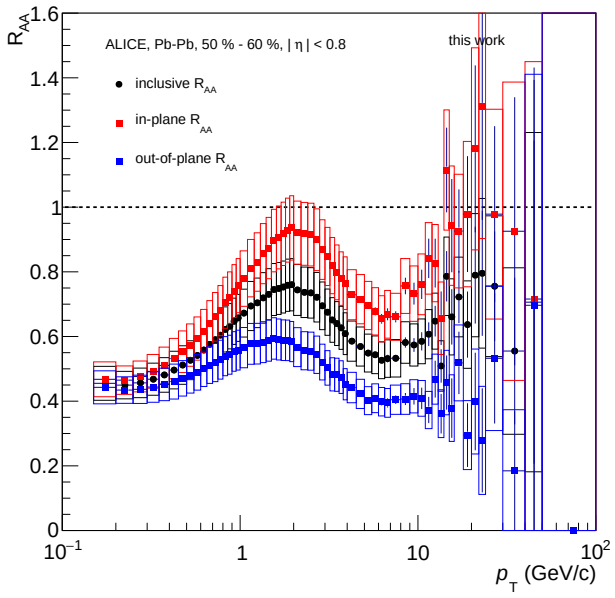

Figure A.34.: LHC11h, 50 - 60 %

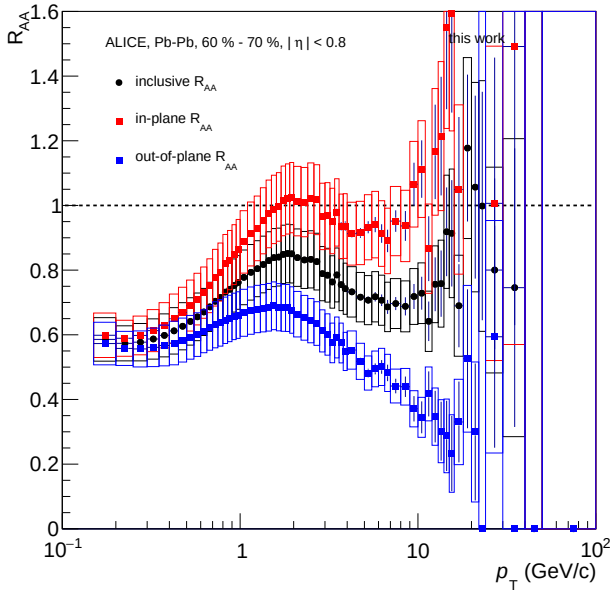

Figure A.35.: LHC11h, 60 - 70 %

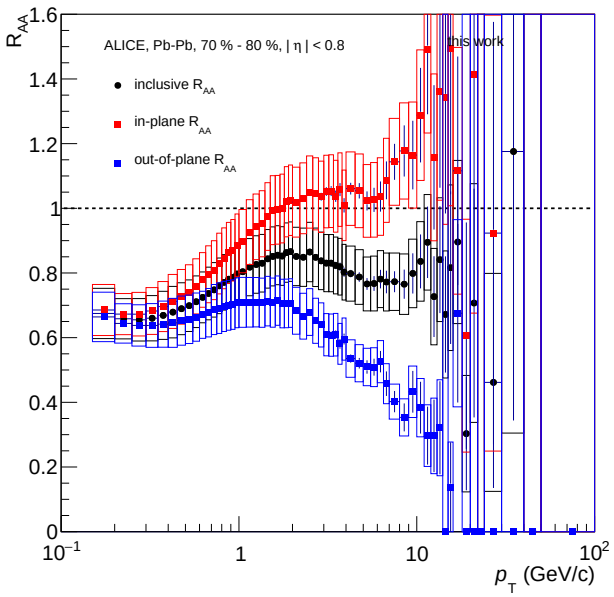

Figure A.36.: LHC11h, 70 - 80 %

Appendix B.

Selected Runs

LHC10h

139510, 139507, 139505, 139503, 139465, 139438, 139437, 139360, 139329, 139328, 139314, 139310, 139309, 139173, 139107, 139105, 139038, 139037, 139036, 139029, 139028, 138872, 138871, 138870, 138837, 138732, 138730, 138662, 138653, 138652, 138638, 138624, 138621, 138583, 138582, 138578, 138534, 138469, 138442, 138439, 138438, 138396, 138364, 138275, 138225, 138201, 138197, 138192, 138190, 137848, 137844, 137752, 137751, 137724, 137722, 137718, 137704, 137693, 137692, 137691, 137686, 137685, 137639, 137638, 137608, 137595, 137549, 137544, 137541, 137539, 137531, 137530, 137443, 137441, 137440, 137439, 137434, 137432, 137431, 137366, 137243, 137236, 137235, 137232, 137231, 137162, 137161

LHC11h

167918, 167920, 167988, 168027, 168072, 168090, 168106, 168108, 168112, 168143, 168310, 168314, 168333, 168342, 168349, 168362, 168410, 168459, 168466, 168489, 168512, 168513, 168579, 168802, 168905, 168990, 169014, 169038, 169042, 169044, 169068, 169092, 169096, 169118, 169140, 169144, 169146, 169152, 169158, 169164, 169202, 169308, 169413, 169416, 169418, 169418, 169420, 169448, 169486, 169501, 169505, 169509, 169514, 169532, 169552, 169554, 169554, 169556, 169570, 169585, 169586, 169588, 169589, 169590, 169610, 169836, 169838, 169842, 169850, 169856, 169858, 169886, 169924, 169967, 170032, 170060, 170082, 170084, 170084, 170086, 170088, 170090, 170122, 170157, 170160, 170178, 170194, 170204, 170204, 170208, 170229, 170247, 170268, 170270, 170288, 170307, 170308, 170310, 170312, 170312, 170314, 170344, 170388, 170388, 170582, 170594

Filter Bits and Cut Setting

Track Cut	kTrkGlobal	kTrkGlobalSDD
$N_{crossedRowsTPC}$	> 70	> 70
$N_{crossedRowsTPC}/N_{findableclusters}$	> 0.8	> 0.8
$\chi^2/cluster_{TPC}$	< 4	< 4
accept kink daughters	no	no
Require TPC Refit	yes	yes
Require ITS Refit	yes	yes
Cluster Requirement ITS	two, one in SPD	none in SPD, first in SDD
MaxDCAToVertexXYPtDep	$0.0105 + 0.0350/p_{\mathrm{T}}^{1.1}$	$0.0105 + 0.0350/p_{\mathrm{T}}^{1.1}$
$\chi^2_{TPC,constrainedglobal}$	< 36	< 36
$DCA_{vertex,z}$	< 2	< 2
$DCA_{vertex,2D}$	no	no
$DCA_{vertex,xy}$	no cut	no cut
Require σ to vertex	no	no
$\chi^2/cluster_{TPC}$	< 36	< 36
fraction shared clusters TPC	no cut	no cut

Table B.1.: Track cuts applied in the prefiltering process and marked with specific bits to enable a fast selection.

Appendix C.

Additional Information

Interaction of Charged Particles within a Gas

If a charged particle traverses a gas-filled volume, e.g. the TPC, it interacts via the coulomb force with the electrons of the gas mixture. If the energy, which is tranfered by this interaction, is large enough, the gas in the detector is ionized and the primary charged particle looses energy. The average energy loss per unit path length in the medium can be approximated with the modified Bethe-Bloch equation (see also [59], chapter 27.2.):

$$-\frac{\mathrm{dE}}{\mathrm{dx}} = Kz^2\frac{Z}{A}\frac{1}{\beta^2}\left[\frac{1}{2}\ln\frac{2m_e c^2\beta^2\gamma^2 T_{max}}{I^2} - \beta^2 - \frac{\delta(\beta\gamma)}{2}\right] \tag{C.1}$$

Here, T_{max} is the maximum energy, which can be transferred in one collision, K is a constant which includes Avogadro's number, the radius of an electron and the mass of an electron. z is the charge of the primary, incoming particle, Z the number of protons of one gas atom, A is the mass of one gas atom, m_e the mass of an electron. An additional term ($\delta(\beta\gamma)$) corrects the density for the behaviour of particles at very high velocities. The transverse component of the electric field of the particle increases, but is limited by the possible polarization of the surrounding atoms and ends in the so-called *Fermi-Plateau*. An additional term can be added, which corrects the Bethe-Bloch equation for the screening of the electrons in the inner shells by the outer electron shells.
The minimum to the specific energy loss is for particles with $\beta \approx 0.97$. Particles with velocities in this region are often called *minimum ionizing particles* (MIP).
The specific energy loss in a medium is not constant, but can be described by an

asymmetric distribution, e.g. the landau distribution, which is given as

$$f = \frac{1}{\sqrt{2\pi}} \exp\left(-\frac{1}{2}(\lambda + exp(-\lambda))\right) \tag{C.2}$$

where λ is the average energy loss normalized to the most probable energy loss.

Movement of Electrons in a Gas

If a gas is ionized, electrons and ions are separated. During their flight through the gas, the electrons loose more and more energy via elastic collisions. If the kinetic energy equals the thermal energy of the gas, the electrons do not loose more energy. The energy distribution of particles in a gas can be described with the Maxwell distribution:

$$F(\epsilon) = C\sqrt{\epsilon} \cdot \exp\left(-\frac{\epsilon}{kT}\right), \text{ with } C = \sqrt{\frac{4}{\pi k^3 T^3}} \tag{C.3}$$

Here, ϵ is the energy of the electrons, k is the Boltzmann constant and T the temperature of the gas.

Drift Velocity

Starting from a gas and a point-like charge distribution, which expands gaussian with time, and neglecting ion enrichment, the density distribution can be described as follows:

$$\frac{\mathrm{d}N}{N} = \frac{1}{\sqrt{4\pi Dt}} \exp\left(-\frac{(x - x_0)^2}{4Dt}\right) \mathrm{d}x \tag{C.4}$$

D is the diffusion constant of the gas. The width of this distribution is given as:

$$\sigma_{diff}^2 = 4Dt \tag{C.5}$$

$$\Rightarrow \sigma_{diff} = 2\sqrt{Dt} \tag{C.6}$$

The drift time t can be replaced by the drift length L and the drift velocity v_D, which results in:

$$\sigma_{diff} = 2\sqrt{D\frac{L}{v_D}} \tag{C.7}$$

Including the scattering cross section, the acceleration in the electric field and the particle density, v_D can be determined as:

$$v_D = \frac{e}{\sqrt{2m_e}} \frac{1}{\sigma(\epsilon)\sqrt{\epsilon}} \frac{E}{N} \tag{C.8}$$

With the equation of state

$$P \cdot V = N \cdot k_B \cdot T \tag{C.9}$$

$$\Rightarrow \frac{1}{N} = \frac{k_B \cdot T}{P \cdot V} \tag{C.10}$$

the drift velocity can be rewritten as

$$v_D = \frac{e}{\sqrt{2m_e}} \frac{1}{\sigma(\epsilon)\sqrt{\epsilon}} \frac{E}{P} \frac{k_B \cdot T}{V} \tag{C.11}$$

Coordinate System in ALICE

The coordinate system in ALICE [60] is a Cartessian coordinate system with its origin in the ideal interaction vertex. The main coordinates are defined as follows:

- The **x coordinate** is horizontal perpendicular to the beam direction. Positive values point to the center of the LHC, negative in the opposite direction.
- The **y coordinate** is vertical perpendicular to the beam direction. Positive values point upwards, negative ones downwards.
- The **z coordinate** moves with the beam direction. The muon arm in ALICE is at negative z values, which is often reffered to as *C-Side*, while the opposite direction is the so-called *A-Side*.
- The **azimuthal angle** ϕ in the x-y plane increases clockwise looking from the opposite direction to the muon arm.
- The **polar angle** θ increases from positive z ($\theta = 0$) to negative z ($\theta = \pi$).

Kinematic Variables

Each particle has a four-momentum, which consists of the energy E of the particle and its three-momentum vector $\vec{p}$

$$P = (E, \vec{p}) = (E, p_x, p_y, p_z) \tag{C.12}$$

where p_x, p_y, p_z are the components of the three-momentum vector in Cartesian coordinates.

Transverse Momentum, Rapidity, Pseudorapidity

The momentum $\vec{p}$ of a particle can be split into a longitudinal component p_L and a transverse component p_T. Longitudinal means *in beam direction*, while transverse is *perpendicular to the beam direction*. In the ALICE coordinate system, p_T and p_L can be written as

$$p = |\vec{p}| \quad = \sqrt{p_x^2 + p_y^2 + p_z^2} \quad = \sqrt{p_\mathrm{L}^2 + p_\mathrm{T}^2} \tag{C.13}$$

$$p_\mathrm{L} \quad \overset{(ALICE)}{=} p\cos\theta \quad = p_z \tag{C.14}$$

$$p_\mathrm{T} \quad \overset{(ALICE)}{=} p\sin\theta \quad = \sqrt{p_x^2 + p_y^2} \tag{C.15}$$

The transverse momentum p_T is invariant under Lorentz transformation, while the longitudinal momentum p_L is not invariant. A Lorentz invariant measure along the beam direction is the *rapidity*, which is defined as:

$$y = \frac{1}{2}\ln\left(\frac{E + p_\mathrm{L}}{E - p_\mathrm{L}}\right) \tag{C.16}$$

The measurement of the energy of a particle without its identification is difficult. Assuming, that the energy of the particle is much larger than the rest mass of the particle, the energy of the particle is approximately its momentum. The rapidity can then be rewritten as

$$y \approx \frac{1}{2}\ln\left(\frac{p + p_\mathrm{L}}{p - p_\mathrm{L}}\right) \overset{(ALICE)}{=} -\ln\left[\tan\left(\frac{\theta}{2}\right)\right] \equiv \eta \tag{C.17}$$

η is the *pseudorapidity*.

The Mandelstam Variables

To describe collisions of $2 \to 2$ particles, the so-called *Mandelstam* variables are used. They are defined as:

$$s = (P_1 + P_2)^2 = (P_3 + P_4)^2 \tag{C.18}$$

$$t = (P_1 - P_3)^2 = (P_1 - P_4)^2 \tag{C.19}$$

$$u = (P_1 - P_4)^2 = (P_2 - P_3)^2 \tag{C.20}$$

P_1 and P_2 are the four-momentum vectors of the incoming particles, P_3 and P_4 the ones of the outgoing particles.
Mainly used is $\sqrt{s}$, which is a measure of the provided energy in a collision in the center-of-mass. $\sqrt{t}$ is momentum transfer in the reaction of two particles.

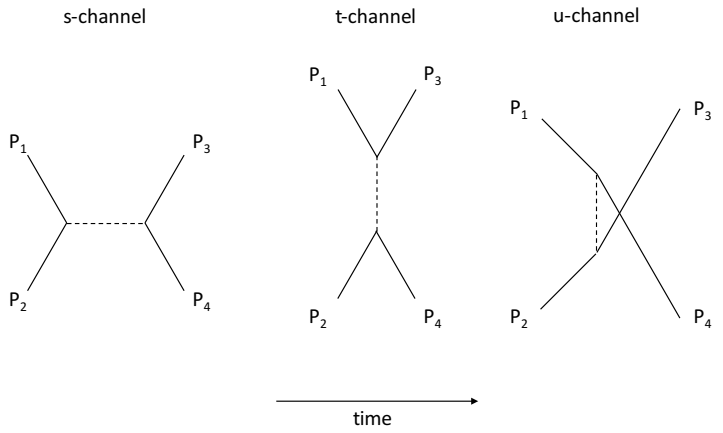

Bibliography

[1] R. Sassot, P. Zurita, M. Stratmann: Inclusive Hadron Production in the CERN-LHC Era, Phys. Rev. **D82 (2010)** 074011, doi:10.1103/PhysRevD.82.074011, 1008.0540.

[2] M. Stratmann: (private communication) .

[3] B. Abelev, et al.: Centrality Dependence of Charged Particle Production at Large Transverse Momentum in Pb–Pb Collisions at $\sqrt{s_{\rm NN}} = 2.76$ TeV, Phys. Lett. **B720 (2013)** 52–62, doi:10.1016/j.physletb.2013.01.051, 1208.2711.

[4] K. Aamodt, et al.: Suppression of Charged Particle Production at Large Transverse Momentum in Central Pb-Pb Collisions at $\sqrt{s_{NN}} = 2.76$ TeV, Phys. Lett. **B696 (2011)** 30–39, doi:10.1016/j.physletb.2010.12.020, 1012.1004.

[5] A. Adare, et al.: Neutral pion production with respect to centrality and reaction plane in Au+Au collisions at $\sqrt{s_{NN}}$=200 GeV, Phys. Rev. **C87 (2013)(3)** 034911, doi:10.1103/PhysRevC.87.034911, 1208.2254.

[6] I. Vitev: Testing the mechanism of QGP-induced energy loss, Phys. Lett. **B639 (2006)** 38–45, doi:10.1016/j.physletb.2006.05.083, hep-ph/0603010.

[7] Y. L. Dokshitzer, D. E. Kharzeev: Heavy quark colorimetry of QCD matter, Phys. Lett. **B519 (2001)** 199–206, doi:10.1016/S0370-2693(01)01130-3, hep-ph/0106202.

[8] F. Englert, R. Brout: Broken Symmetry and the Mass of Gauge Vector Mesons, Phys. Rev. Lett. **13 (1964)** 321–323, doi:10.1103/PhysRevLett.13.321.

[9] P. W. Higgs: Broken Symmetries and the Masses of Gauge Bosons, Phys. Rev. Lett. **13 (1964)** 508–509, doi:10.1103/PhysRevLett.13.508.

[10] K. Nakamura, et al.: Review of particle physics, J. Phys. **G37 (2010)** 075021, doi:10.1088/0954-3899/37/7A/075021.

[11] S. Navin: Diffraction in Pythia **(2010)**, 1005.3894.

[12] D. University: On-line Plotting and Calculation of Particle Distribution Functions **(2016)**, URL http://hepdata.cedar.ac.uk/pdf/pdf3.html.

[13] P. M. Nadolsky, H.-L. Lai, Q.-H. Cao, J. Huston, J. Pumplin, D. Stump, W.-K. Tung, C. P. Yuan: Implications of CTEQ global analysis for collider observables, Phys. Rev. **D78 (2008)** 013004, doi:10.1103/PhysRevD.78.013004, 0802.0007.

[14] K. J. Eskola, H. Paukkunen, C. A. Salgado: EPS09: A New Generation of NLO and LO Nuclear Parton Distribution Functions, JHEP **04 (2009)** 065, doi:10.1088/1126-6708/2009/04/065, 0902.4154.

[15] K. J. Eskola, H. Paukkunen, C. A. Salgado: Nuclear PDFs at NLO - status report and review of the EPS09 results, Nucl. Phys. **A855 (2011)** 150–157, doi:10.1016/j.nuclphysa.2011.02.032, 1011.6534.

[16] J. Book: J/ψ Production in Pb–Pb collisions with ALICE at the LHC, Ph.D. thesis (2014).

[17] L. Lederman, e. J. Wesener: Report of the workshop on GeV/nucleon collisions of heavy ions: how and why, November 29–December 1, 1974, Bear Mountain, New York. Brookhaven National Laboratory Associated Universities, Inc. **(1974)**, URL http://www.osti.gov/scitech/servlets/purl/4061527.

[18] T. Matsui, H. Satz: J/ψ Suppression by Quark-Gluon Plasma Formation, Phys. Lett. **B178 (1986)** 416–422, doi:10.1016/0370-2693(86)91404-8.

[19] R. H. Brown, R. Q. Twiss: Correlation between Photons in two Coherent Beams of Light, Nature **177 (1956)** 27–29, doi:10.1038/177027a0.

[20] A. M. Poskanzer, S. A. Voloshin: Methods for analyzing anisotropic flow in relativistic nuclear collisions, Phys. Rev. **C58 (1998)** 1671–1678, doi:10.1103/PhysRevC.58.1671, nucl-ex/9805001.

[21] S. Voloshin, Y. Zhang: Flow study in relativistic nuclear collisions by Fourier expansion of Azimuthal particle distributions, Z. Phys. **C70 (1996)** 665–672, doi:10.1007/s002880050141, hep-ph/9407282.

[22] K. Aamodt, et al.: Higher harmonic anisotropic flow measurements of charged particles in Pb-Pb collisions at $\sqrt{s_{NN}}$=2.76 TeV, Phys. Rev. Lett. **107 (2011)** 032301, doi:10.1103/PhysRevLett.107.032301, 1105.3865.

[23] C. A. Loizides: Jet physics in ALICE, Ph.D. thesis, Frankfurt U. (2005), `nucl-ex/0501017`.

[24] X.-N. Wang, M. Gyulassy, M. Plumer: The LPM effect in QCD and radiative energy loss in a quark gluon plasma, Phys. Rev. **D51 (1995)** 3436–3446, doi:10.1103/PhysRevD.51.3436, `hep-ph/9408344`.

[25] D. d'Enterria, B. Betz: High-p(T) hadron suppression and jet quenching, Lect. Notes Phys. **785 (2010)** 285–339, doi:10.1007/978-3-642-02286-9_9.

[26] O. Fochler: Nuclear modification factor from simplistic energy loss models, private communication **(2012)**.

[27] J. Adams, et al.: Transverse momentum and collision energy dependence of high p(T) hadron suppression in Au+Au collisions at ultrarelativistic energies, Phys. Rev. Lett. **91 (2003)** 172302, doi:10.1103/PhysRevLett.91.172302, `nucl-ex/0305015`.

[28] S. S. Adler, et al.: High p_T charged hadron suppression in Au + Au collisions at $\sqrt{s}_{NN} = 200$ GeV, Phys. Rev. **C69 (2004)** 034910, doi:10.1103/PhysRevC.69.034910, `nucl-ex/0308006`.

[29] S. P. Horvat: Measurement of beam energy dependent nuclear modification factors at STAR, J. Phys. Conf. Ser. **446 (2013)** 012017, doi:10.1088/1742-6596/446/1/012017, `1303.7260`.

[30] X.-N. Wang: pQCD based approach to parton production and equilibration in high-energy nuclear collisions, Phys. Rept. **280 (1997)** 287–371, doi:10.1016/S0370-1573(96)00022-1, `hep-ph/9605214`.

[31] A. Horvath: LHC, Wikimedia Commons **(2006)**, URL `https://commons.wikimedia.org/wiki/File:LHC.svg`.

[32] K. Aamodt, et al.: The ALICE experiment at the CERN LHC, JINST **3 (2008)** S08002, doi:10.1088/1748-0221/3/08/S08002.

[33] G. Dellacasa, et al.: ALICE technical design report of the inner tracking system (ITS) **(1999)**.

[34] C. Lippmann: Upgrade of the ALICE Time Projection Chamber **(2014)**.

[35] B. B. Abelev, et al.: Energy Dependence of the Transverse Momentum Distributions of Charged Particles in pp Collisions Measured by ALICE, Eur. Phys. J. **C73**

(2013)(12) 2662, doi:10.1140/epjc/s10052-013-2662-9, 1307.1093.

[36] B. Abelev, et al.: Centrality determination of Pb-Pb collisions at $\sqrt{s_{NN}} = 2.76$ TeV with ALICE, Phys. Rev. **C88 (2013)(4)** 044909, doi:10.1103/PhysRevC.88.044909, 1301.4361.

[37] ALICE-TPC: TPC QA (internal communication) **(2016)**.

[38] CERN: GEANT - Detector Description and Simulation Tool **(2010)**, URL http://wwwasd.web.cern.ch/wwwasd/geant/.

[39] J. Otwinowski, A. Andronic, M. Knichel, P. Luettig: (private communication) .

[40] B. B. Abelev, et al.: Multiplicity dependence of the average transverse momentum in pp, p-Pb, and Pb-Pb collisions at the LHC, Phys. Lett. **B727 (2013)** 371–380, doi:10.1016/j.physletb.2013.10.054, 1307.1094.

[41] S. Chatrchyan, et al.: Charged particle transverse momentum spectra in *pp* collisions at $\sqrt{s} = 0.9$ and 7 TeV, JHEP **08 (2011)** 086, doi:10.1007/JHEP08(2011)086, 1104.3547.

[42] B. Abelev, et al.: Neutral pion and η meson production in proton-proton collisions at $\sqrt{s} = 0.9$ TeV and $\sqrt{s} = 7$ TeV, Phys. Lett. **B717 (2012)** 162–172, doi:10.1016/j.physletb.2012.09.015, 1205.5724.

[43] M. J. Tannenbaum: Review of hard scattering and jet analysis, PoS **CFRNC2006 (2006)** 001, nucl-ex/0611008.

[44] P. Luettig: Mittlerer Transversalimpuls in pp Kollisionen bei $\sqrt{s} = 900$ GeV (Master Thesis) **(2010)**.

[45] J. Jung: (private communication) **(2016)**.

[46] T. Sjostrand, S. Mrenna, P. Z. Skands: A Brief Introduction to PYTHIA 8.1, Comput. Phys. Commun. **178 (2008)** 852–867, doi:10.1016/j.cpc.2008.01.036, URL http://home.thep.lu.se/~torbjorn/pythia81html/Welcome.html, 0710.3820.

[47] J. Jung: A geometric approach of simulating the mean transverse momentum in Pb–Pb collisions as a superposition of p–Pb events (Bachelor Thesis) **(2015)**.

[48] R. Hagedorn: Multiplicities, p_T Distributions and the Expected Hadron $\rightarrow$ Quark - Gluon Phase Transition, Riv. Nuovo Cim. **6N10 (1983)** 1–50, doi:10.1007/BF02740917.

[49] P. Huhn: Studie zur Triggereffizienz geladener Teilchen in ALICE (Bachelor Thesis) **(2015)**.

[50] B. B. Abelev, et al.: Transverse momentum dependence of inclusive primary charged-particle production in p-Pb collisions at $\sqrt{s_{\rm NN}} = 5.02$ TeV, Eur. Phys. J. **C74 (2014)(9)** 3054, doi:10.1140/epjc/s10052-014-3054-5, 1405.2737.

[51] J. Adam, et al.: Pseudorapidity and transverse-momentum distributions of charged particles in proton–proton collisions at $\sqrt{s} = 13$ TeV, Phys. Lett. **B753 (2016)** 319–329, doi:10.1016/j.physletb.2015.12.030, 1509.08734.

[52] T. Aaltonen, et al.: Measurement of Particle Production and Inclusive Differential Cross Sections in $p\bar{p}$ Collisions at $\sqrt{s} = 1.96$-TeV, Phys. Rev. **D79 (2009)** 112005, doi:10.1103/PhysRevD.82.119903,10.1103/PhysRevD.79.112005, [Erratum: Phys. Rev.D82,119903(2010)], 0904.1098.

[53] A. Adare, et al.: Suppression pattern of neutral pions at high transverse momentum in Au + Au collisions at s(NN)**(1/2) = 200-GeV and constraints on medium transport coefficients, Phys. Rev. Lett. **101 (2008)** 232301, doi:10.1103/PhysRevLett.101.232301, 0801.4020.

[54] S. S. Adler, et al.: A Detailed Study of High-p(T) Neutral Pion Suppression and Azimuthal Anisotropy in Au+Au Collisions at s(NN)**(1/2) = 200-GeV, Phys. Rev. **C76 (2007)** 034904, doi:10.1103/PhysRevC.76.034904, nucl-ex/0611007.

[55] W. A. Horowitz, M. Gyulassy: The Surprising Transparency of the sQGP at LHC, Nucl. Phys. **A872 (2011)** 265–285, doi:10.1016/j.nuclphysa.2011.09.018, 1104.4958.

[56] A. Drees, H. Feng, J. Jia: Medium induced jet absorption at RHIC, Phys. Rev. **C71 (2005)** 034909, doi:10.1103/PhysRevC.71.034909, nucl-th/0310044.

[57] T. Renk, K. Eskola: Prospects of medium tomography using back-to-back hadron correlations, Phys. Rev. **C75 (2007)** 054910, doi:10.1103/PhysRevC.75.054910, hep-ph/0610059.

[58] M. Verweij: Modelling and measurement of jet quenching in relativistic heavy-ion collisions at the LHC, Ph.D. thesis, Utrecht U. (2013), URL http://inspirehep.net/record/1296927/files/thesis_M_Verweij.pdf.

[59] P. D. Group: Review of Particle Physics **(2008)**.

[60] A. Collaboration: Definition of the ALICE Coordinate System and Basic Rules for Sub-detector Components Numbering, ALICE-INT-2003-038 **(2003)**.

Danksagung

An dieser Stelle möchte ich zuerst meinem Doktorvater Henner Büsching danken, der mir diese Arbeit ermöglicht hat. Durch seine Unterstützung war es mir möglich, Teil des ALICE-Experiments zu sein. Ebenso danke ich ihm für für das stets offene Ohr bei Fragen und viele spannende Diskussionen, die zum Gelingen dieser Arbeit beigetragen haben. Für die Möglichkeiten, durch die Teilnahme bei Konferenzen die Facetten der Schwerionenphysik kennenzulernen, danke ich ihm ebenfalls. Harald Appelshäuser danke ich für die Begutachtung dieser Arbeit, für viele spannende und fruchtbare Diskussionen sowie die Unterstützung bei Veröffentlichungen.
Anton Andronic, Julius Gronefeld, Michael Knichel, Edgar Perez Lezama, Kai Schweda und Jacek Otwinowski danke ich für die Zusammenarbeit in den letzten Jahren bei der Analyse der Spektren und den daraus resultierenden Veröffentlichungen.
Für die finanzielle Unterstützung danke ich HGS-HIRe und H-QM. Dem Team der HGS-HIRe Gerhard Burau, Johanna Dilley, Helena Santos, Sylke Schneider und Sascha Vogel danke ich für die Organisation von Lecture Weeks, Power Weeks und Seminaren, aber auch für die Hilfe und Unterstützung bei vielen organisatorischen Fragen.
Mein Dank gilt Andreas Arend, Theo Bröker, Jerome Jung und Sylke Schneider, die als Bürokollegen das Enstehen dieser Arbeit über die Jahre miterlebt haben und mir hilfreich zur Seite gestanden haben. Claudia Freudenberger, Marianne Frey und Ulrich Köpf danke ich für die Unterstützung bei allen organisatorischen Fragen; meinen Adminkollegen Werner Amend, Christoph Baumann, Ernst Hellbär, Patrick Huhn, Carsten Klein, Theodor Rascanu, Sebastian Scheidt und Jens Wiechula für die spannende Zusammenarbeit rund um die IT; Patrick Huhn, Marco Marquard und Fabian Pliquett für die Zusammenarbeit bei vielen Analysen, aber auch bei der Organisation vieler Projekte; ebenso danke ich Julian Book, Pascal Dillenseger, Benjamin Dönigus, Stefan Heckel, Baldo Sahlmüller und Simone Schuchmann, die mir bei vielen Fragen, speziell rund um die Analyse, weitergeholfen haben. Besonders bedanken möchte ich mich bei Werner Amend, ohne dessen Unterstützung vieles nicht möglich gewesen wäre. Ebenso gilt Patrick Reichelt Dank für seine stete Unterstützung über die Jahre. Dank gilt auch allen weiteren Mitgliedern der HEP-Gruppe und des IKF.
Zuletzt gilt mein Dank meiner Familie: meinen Eltern, Großeltern, Brüdern und besonders meiner kleinen Familie für die immerwährende Unterstützung über viele Jahre, ohne die diese Arbeit nicht möglich gewesen wäre.

Curriculum Vitae

Philipp Lüttig

Date and Place of Birth: 03.05.1986, Frankfurt am Main

Education

since Oct 2010	PhD student at Goethe University Frankfurt
	Advisor: Prof. Dr. Henner Büsching
since Oct 2010	Member of HGS-HIRe and H-QM
Sep 2008 - Sep 2010	Physics Studies at Goethe University Frankfurt (Master Degree)
	Advisor: Prof. Dr. Harald Appelshäuser
	Topic: Average Transverse Momentum in
	proton-proton collisions at $\sqrt{s} = 900$ GeV
Apr 2006 - Aug 2008	Physics Studies at Goethe University Frankfurt (Bachelor Degree)
	Advisor: Prof. Dr. Harald Appelshäuser
	Topic: Development of a Testing Environment
	for TRD Readout Chambers
1996 - 2005	A Level at Heinrich-von-Gagern-Gymnasium (Abitur)

Selected Publications

ALICE Collaboration: *Pseudorapidity and transverse-momentum distributions of charged particles in proton–proton collisions at $\sqrt{s} = 13$ TeV*, Phys. Lett. B **753** (2016) 319

ALICE Collaboration: *Transverse momentum dependence of inclusive primary charged-particle production in p-Pb collisions at $\sqrt{s_{\mathrm{NN}}} = 5.02$ TeV*, Eur. Phys. J. C **74** (2014) no.9, 3054

ALICE Collaboration: *Multiplicity dependence of the average transverse momentum in pp, p-Pb, and Pb-Pb collisions at the LHC*, Phys. Lett. B **727** (2013) 371

ALICE Collaboration: *Energy Dependence of the Transverse Momentum Distributions of Charged Particles in pp Collisions Measured by ALICE* Eur. Phys. J. C **73** (2013) no.12, 2662

ALICE Collaboration: *Transverse momentum distribution and nuclear modification factor of charged particles in p-Pb collisions at* $\sqrt{s_{NN}} = 5.02$ *TeV*, Phys. Rev. Lett. **110** (2013) no.8, 082302

ALICE Collaboration: *Centrality Dependence of Charged Particle Production at Large Transverse Momentum in Pb–Pb Collisions at* $\sqrt{s_{\rm NN}} = 2.76$ *TeV*, Phys. Lett. B **720** (2013) 52

ALICE Collaboration: *Suppression of Charged Particle Production at Large Transverse Momentum in Central Pb-Pb Collisions at* $\sqrt{s_{NN}} = 2.76$ *TeV*, Phys. Lett. B **696** (2011) 30

ALICE Collaboration: *Transverse momentum spectra of charged particles in proton-proton collisions at* $\sqrt{s} = 900$ *GeV with ALICE at the LHC*, Phys. Lett. B **693** (2010) 53

Presentations

Transverse Momentum Spectra of Inclusive Charged Particles in pp, p–Pb and Pb–Pb Collisions, DPG Spring Meeting 2015, Heidelberg

ALICE results on light flavour hadron production in p–Pb collisions at the LHC, Rencontres de Moriond 2014

Transverse Momentum Spectra of Unidentified Charged Particles in pp, p–Pb and Pb–Pb Collisions, DPG Spring Meeting 2014, Frankfurt

Transverse Momentum Spectra of Unidentified Charged Particles in pp Collisions at the ALICE experiment, Hard Probes Conference 2012, Sardegna (poster)

Suppression of Charged Particle Production at High $p_{\rm T}$ *in ALICE*, 7th International Workshop High-$p_{\rm T}$ physics at LHC 2012

Transverse Momentum Spectra of Unidentified Charged Particles in pp Collisions at the ALICE experiment, DPG Spring Meeting 2012, Mainz

Correlation Between $\langle p_{\rm T} \rangle$ *and Charged Particle Multiplicity in pp Collisions at* $\sqrt{s} = 0.9$, 2.76 *and* 7 *TeV with ALICE*, Quark Matter Conference 2011, Annecy (poster)

Suppression of Particle Production at High $p_{\rm T}$ *in ALICE*, 6th International Workshop High-$p_{\rm T}$ physics at LHC 2011